

FABRICATION OF NANO AND POROUS MATERIALS & THEIR UTILIZATION
IN THE PURIFICATION OF WATER CONTAMINATED WITH ARSENIC,
COPPER, AND LEAD

by

ZÜLEYHA ÖZLEM KOCABAŞ ATAKLI

Submitted to the Graduate School of Engineering and Natural Sciences

in partial fulfillment of the requirements for the degree of

Doctor of Philosophy

Sabancı University


July 2013

FABRICATION OF NANO AND POROUS MATERIALS & THEIR
UTILIZATION IN THE PURIFICATION OF WATER CONTAMINATED WITH
ARSENIC, COPPER, AND LEAD

APPROVED BY

Prof. Dr. Yuda Yürüm

(Thesis Supervisor)



Prof. Dr. M. Ferhat Yardım



Assoc. Prof. Selmiye Alkan Gürsel



Asst. Prof. Alpay Taralp



Asst. Prof. Fevzi Çakmak Cebeci



DATE OF APPROVAL: 19.07.2013

© ZÜLEYHA ÖZLEM KOCABAŞ ATAKLI 2013

All Rights Reserved

FABRICATION OF NANO AND POROUS MATERIALS & THEIR UTILIZATION
IN THE PURIFICATION OF WATER CONTAMINATED WITH ARSENIC,
COPPER, AND LEAD

ZÜLEYHA ÖZLEM KOCABAŞ ATAKLI

Materials Science and Engineering, PhD Dissertation, 2013

Supervisor: Prof. Dr. Yuda Yürüm

Keywords: Nanomaterials, Titanium dioxide, Iron oxide, Adsorption, Kinetics, Copper, Lead, Arsenic

ABSTRACT

Water pollution mainly caused by arsenic and heavy metal ions is a growing threat to environment and public health. Adsorption is one of the most efficient methods for the removal of the contaminants due to its high efficiency, easy operation and low cost. This thesis aims to develop nano and porous materials, and then implement these into adsorptions of arsenic, lead, and copper in order to investigate an effective water purification system for communities. In this study, specific functional nanomaterials comprising ferric ion loaded red mud, iron oxide/activated carbon, titanium dioxide nanoparticles, and titanium dioxide/activated carbon nanocomposites have been successfully fabricated. The obtained nanomaterials are characterized by using X-ray diffraction, Raman spectroscopy, scanning electron microscopy, Fourier transform infrared spectroscopy, and X-ray photoelectron spectrometer.

The arsenic removal efficiency of ferric ion loaded red mud considering effect of pH, initial arsenic concentration, and contact time is evaluated and the higher adsorption capacities found 11.640 mg/g for As(V) at pH 7.0 and 5.254 mg/g for As(III) at pH 2.0. The presence of ferric ion in the system increased the uptakes of arsenic species from water; therefore, the following study is focused on utilization of iron oxide nanoparticles deposited uniformly on activated carbon support with high loadings by microwave hydrothermal treatment. Maximum adsorption capacity is 27.78 mg/g for As(V) and for a loading of 0.75 g/L, 99.90% uptake is reached within 5 minutes. On the other hand, the beneficial adsorptive eliminations of Pb(II), Cu(II), and As(III) from water are also demonstrated using anatase nanoadsorbent produced by sol-gel method. The maximum experimental adsorption uptakes were 31.25 mg/g for Pb(II), 23.74 mg/g for Cu(II), and 16.98 mg/g for As(III), respectively. XPS analyses revealed that the surface oxygen-containing functional groups including hydroxyl groups were involved in the adsorption process. In order to prevent release of the nanoparticles to the environment, activated carbon was used as a support material for TiO₂ nanoparticles. It was observed that As(III) uptake capacity of the nanocomposite was improved approximately 2.7 times as compare to the bare TiO₂ nanoparticles. Finally, the effectiveness of titanium dioxide nanoparticles in removing arsenic species from water was enhanced by the photocatalytic oxidation experiments converting As(III) to As(V). The maximum adsorption capacities were found 12.13 mg/g for As(III) in the absence of UV-A illumination, 41.38 mg/g for As(V), and 36.55 mg/g for As(III) in the presence of UV-A illumination.

Overall, anatase nanoadsorbent are able to reduce Pb(II) and Cu(II) concentrations below the MCL requirements for drinking water. The enhanced As(III) removal are observed under UV-A illumination by using TiO₂ nanoparticles and they are able to reduce As(III) concentrations below the MCL requirements for drinking water up to moderate initial concentrations. Additionally, 10-AC/TiO₂ nanocomposite, having a considerable As(III) uptake capacity, can be also potentially used in arsenic removal.

NANO VE GÖZENEKLİ MALZEMELERİN ÜRETİMİ VE BUNLARIN ARSENİK,
BAKIR VE KURŞUN İLE KİRLENMİŞ SULARIN TEMİZLENMESİNDE
KULLANIMI

ZÜLEYHA ÖZLEM KOCABAŞ ATAKLI

Malzeme Bilimi ve Mühendisliği, Doktora Tezi, 2013

Tez Danışmanı: Prof. Dr. Yuda Yürüm

Anahtar Kelimeler: Nano malzemeler, Titanyum dioksit, Demir oksit, Adsorpsiyon,
Kinetik, Bakır, Kurşun Arsenik

ÖZET

Suların arsenik ve ağır metaller ile kirletilmesi çevre ve insan sağlığı için giderek büyüyen bir tehlike haline gelmiştir. Adsorpsiyon yöntemi diğer su temizliği teknikleri arasında en etkili, uygulanabilir ve düşük maliyete sahip olmaktadır. Bu tez çalışmasında nano ve gözenekli malzemeler sulardan arsenik, kurşun ve bakır'ın alınması için geliştirilerek; etkin, ucuz ve yüksek kalitede su temizliği sağlayacak sistemin ortaya koyulması amaçlanmıştır. Bu çalışmada ferrik iyonları ile yüklenmiş kırmızı çamur, demir oksit/aktif karbon, titanyum dioksit nano parçacıklar ve titanyum dioksit/aktif karbon nano kompozitlerden oluşan spesifik fonksiyonel nano malzemeler başarılı bir şekilde üretilmiştir. Elde edilen bu malzemeler X-ışını kırınımı, taramalı elektron mikroskopisi, Raman spektrometrisi, FTIR spektrometrisi ve X-ışını foto elektron spektroskopisi kullanılarak ayrıntılı olarak karakterize edilmiştir.

Ferrik iyonları ile yüklenmiş kırmızı çamurun sulardan arsenik alma etkinliği pH, temas süresi ve ilk arsenik konsantrasyon miktarı göz önüne alınarak, As(V) iyonu için pH 7.0'de 11.640 mg/L ve As(III) iyonları için pH 2.0'de 5.254 mg/L olarak bulunmuştur. Ferrik iyonların arsenik alımını iyileştirdiği gözlenmesinin sonucunda yüksek miktarda demir oksit nano parçacıkları ile kaplı aktif karbon mikrodalga yöntemi ile üretilmiştir. Bu malzemelerin maksimum adsorpsiyon kapasiteleri 27.78 mg/g olup 0.75 mg/L adsorban kullanarak 5 dakikalık temas süresi sonunda sudan %99.90 oranında As(V) alınmıştır. Sol-gel yöntemi ile sentezlenen anataz nano parçacıkları ile kurşun, bakır ve arsenik sulardan adsorpsiyon yöntemi ile başarılı bir şekilde alınmıştır. Bulunan korelasyon katsayısı ve ortalama hata oranı değerlerine göre, Pb(II) adsorpsiyonu en iyi Langmuir izotermi ile Cu(II) ve As(III) adsorpsiyonları ise Freundlich izotermi ile açıklanmıştır. Deneysel olarak bulunan maksimum adsorpsiyon değerleri kurşun için 31.25 mg/L, bakır için 23.74 mg/L ve arsenik için 16.98 mg/L olarak bulunmuştur. XPS analizleri sonucunda adsorpsiyon prosesinde yüzeydeki oksijen içeren gruplar rol aldığı bulunmuştur. Nano parçacıkların çevreye dağılmasını engellemek için, üretilen titanyum dioksit nano parçacıklarının içerisine aktif karbon eklenmiş olup, bu nano kompozitin arsenik tutma kapasitesi, saf titanyum dioksit nano parçacıkların 2.7 katında arttırdığı görülmüştür. Son olarak titanyum dioksit nano parçacıkların sulardan arsenik tutma kapasiteleri foto katalitik oksidasyon yöntemi kullanarak iyileştirilmiştir. Titanyum dioksit nano parçacıklarını içeren 4 mg/L As(III) solüsyon 120 dakika içerisinde denge durumuna gelmiştir. Maksimum UV-A ışığı yokluğunda As(III) adsorpsiyonu 12.13 mg/g ve As(V) adsorpsiyonu 41.38 mg/g olup, UV-A ışığında 36.55 mg/g As(III) adsorplanmıştır.

Genel olarak, anataz nano adsorbanlar kullanılarak içme sularındaki maksimum Pb(II) ve Cu(II) konsantrasyonların altına düşürülebilir. UV-A ışığı ile aydınlatılan titanyum dioksit nano parçacıklar sulardaki maksimum As(III) konsantrasyonunu belirlenen değerlerin altına düşmesinde etkili olmuşlardır. Ayrıca üretilen 10-AC/TiO₂ nano kompozit malzemesi yüksek As(III) alımı ile sulardan arsenik alınmasında kullanılan potansiyel bir malzeme olabilir.

«»To my family«»

Ahmet & Sunay & İrem KOCABAŞ

Your support and encouragement has brought me this far.

ACKNOWLEDGMENTS

Firstly, I would like to give my special thanks to my advisor Prof. Dr. Yuda Yürüm for his patient guidance, encouragement and excellent advises throughout the research.

Special thanks go to “Veli Bayır and Dr. Mustafa Atilla Yazıcı” for their essential assistance, guidance and help during my graduate years at Sabancı University.

I would like to express many thanks to “Dr. Özgür Birer” for his assistance, guidance and help in my research.

Many thanks go in particular to my colleagues “Dr. Burcu Saner Okan, Dr. Alp Yürüm, and Mustafa Baysal” for their friendly help in my research. I would like to express my warmest thanks to my dear friends “Firuze Okyay, Ezgi Dünder Tekkaya, Elif Özden Yenigün, Lale Işikel Şanlı, Melike Mercan Yıldızhan, Zuhale Taşdemir, Kaan Bilge, Güliz İnan, Ece Alpaslan, Tuğçe Akkaş, Oğuzhan Oğuz” for their friendship and support at Sabancı University.

I owe my loving thanks to my husband Mustafa Nevzat Ataklı and my parents Ahmet Kocabaş, Sunay Kocabaş and İrem Kocabaş who always help and support me in any conditions of my life.

Finally, I would like to express my gratitude to all those who gave me the possibility to complete the thesis.

TABLE OF CONTENTS

ABSTRACT.....	v
ÖZET	vi
ACKNOWLEDGEMENTS.....	ix
TABLE OF CONTENTS.....	x
LIST OF FIGURES	xiv
LIST OF TABLES.....	xviii
LIST OF SYMBOLS AND ABBREVIATIONS	xix
CHAPTER 1. Introduction	1
CHAPTER 2. Literature Survey.....	5
2.1. Contaminations in Natural Water	5
2.1.1. Arsenic	5
2.1.2. Lead	9
2.1.3. Copper.....	10
2.2. Removal Technologies in Wastewater Treatment.....	12
2.2.1.Precipitation and Coagulation Processes	12
2.2.2.Ion exchange Processes	13
2.2.3.Membrane Technology	14
2.2.4.Oxidation Processes.....	15
2.2.5.Adsorption Processes.....	16
2.3.Types of Adsorbents Used in Water Treatment	17
2.3.1. Low-Cost Adsorbents	18
2.3.2. Iron Impregnated Adsorbents	20
2.3.3. Nanoadsorbents.....	21
2.3.4. Nanocatalysts and Redox Active Nanocomposites	23
CHAPTER 3. Kinetic Modeling of Arsenic Removal from Water by Ferric Ion Loaded Red Mud	25
3.1. Background.....	25
3.2. Experimental.....	27
3.2.1. Materials and Reagents.....	27
3.2.2. Preparation of Ferric Ion Loaded Red Mud (FRM).....	27
3.2.3. Adsorption Experiments	28

3.2.4. Characterization	28
3.3. Result and Discussion	29
3.3.1. Characterization of Adsorbent Materials	29
3.3.2. Effect of pH	32
3.3.3. Effect of Initial Arsenic Concentration	34
3.3.4. Effect of Contact Time and Sorption Kinetics	35
3.3.5. Adsorption Capacity	43
3.4. Concluding Remarks	50
CHAPTER 4. As(V) Removal from Water by Iron Oxide/Activated Carbon System Manufactured by Microwave Heating	51
4.1. Background	51
4.2. Experimental	53
4.2.1. Materials	53
4.2.2. Deposition of iron oxide nanoparticles on AC	53
4.2.3. Sample characterization	54
4.2.4. Batch Adsorption Experiments	55
4.3. Result and Discussion	55
4.3.1. XRD characterization of the Samples	55
4.3.2. SEM Characterization of the Particles	56
4.3.3. Porous Texture of the Adsorbents	58
4.3.4. Effect of Heating Duration on Iron Loading	60
4.3.5. Adsorption Isotherms	61
4.3.6. Adsorption Kinetics	64
4.3.7. Effect of solution pH	69
4.4. Concluding Remarks	71
CHAPTER 5. Synthesis and Characterization of Anatase Nanoadsorbent and Application in Removal of Lead, Copper and Arsenic from Water	72
5.1. Background	72
5.2. Materials and Methods	74
5.2.1. Synthesis of Anatase Nanoadsorbent	74
5.2.2. Characterization	74
3.2.3. Adsorption Experiments	75

5.3. Result and Discussion.....	76
3.3.1. Characterization of Nanoadsorbent Materials	76
3.3.2. Kinetic Studies and Mathematical Modeling	80
3.3.3. Adsorption Isotherms	84
3.3.4. Adsorption Thermodynamics	89
3.3.5. Effect of Solution pH	91
3.3.6. Proposed Binding Mechanism.....	94
5.4. Concluding Remarks	99
CHAPTER 6. A Facile Synthesis of Activated Carbon/Titanium Dioxide Nanocomposites for Enhanced As(III) Removal From Water	100
6.1. Background.....	100
6.2. Materials and Methods.....	101
6.2.1. Synthesis of AC/TiO ₂ Nanocomposites.....	101
6.2.2. Characterization.....	102
6.2.3. Adsorption Experiments.....	102
6.3. Result and Discussion.....	104
6.3.1. Characterization of AC/TiO ₂	104
6.3.2. Sorption Kinetics of the AC/TiO ₂ Nanocomposites.....	108
6.3.3. Adsorption Capacity.....	112
6.3.4. Effect of pH on Adsorption	116
6.3.5. Regeneration of AC/TiO ₂	118
6.4. Concluding Remarks.....	120
CHAPTER 7. Arsenic Removal From Water By TiO ₂ Nanoparticles Through Simultaneous Photocatalytic Oxidation And Adsorption.....	121
7.1. Background.....	121
7.2. Materials and Methods.....	123
7.2.1. Synthesis of TiO ₂ Nanoparticles.....	123
7.2.2. Adsorption and photocatalytic oxidation experiments	123
7.2.3. Characterization	124
7.3. Result and Discussion.....	125
7.3.1. Crystal structure and morphology of TiO ₂ Nanoparticles	125
7.3.2. Effect of pH	127

7.3.3. Effect of contact time on arsenic removal and kinetic modeling	128
7.3.4. Role of UV-A Illumination	130
7.3.5. Adsorption isotherm	132
7.3.6. Adsorption Energy	137
7.4. Concluding Remarks	139
CHAPTER 8. Conclusion and Future Works	140
8.1. Conclusion	141
8.2. Future Works	143
BIBLIOGRAPHY	144
Vita	160

LIST OF FIGURES

Figure 2.1. Arsenic species found in water.....	8
Figure 2.2. (a) Arsenate and (b) Arsenite speciation as a function of pH [1].....	8
Figure 2.3. Distribution of Pb(II) species at 25 °C [2]	10
Figure 2.4. The speciation diagram of copper in water [3].....	11
Figure 2.5. The illustration of ion exchange process [4]	13
Figure 2.6. Pressure Driven Membrane Process Classification [5]	14
Figure 2.7. Illustration of specific and nonspecific adsorption.....	17
Figure 2.8. Activated carbon particles with the illustration of micro and mesopores ...	18
Figure 2.9 Ferric hydroxide speciation [6].	20
Figure 2.10. Selected nanomaterials currently being evaluated as functional materials for water purification [7].....	21
Figure 2.11. Schematic of TiO ₂ photocatalytic mechanism [8].....	23
Figure 3.1. (a) SEM micrograph of the particles of the RM and (b) SEM micrograph of the particles of the FRM	29
Figure 3.2. (a) X-ray diffractogram of RM and FRM and (b) Infrared spectra of RM and FRM	31
Figure 3.3. The pH _{final} and arsenic uptake, q _e as a function of pH _{initial} for adsorptions of As(III) and As(V) onto FRM. (initial arsenic concentration: 1mg/L adsorbent amount: 1 mg/L, temperature: 25°C and contact time: 12 h).....	32
Figure 3.4 Effect of initial arsenic concentration on arsenic removal by FRM and RM. (initial arsenic concentration: 0.04-20 mg/L, adsorbent amount: 1 mg/L, pH: 2.0, temperature: 25°C and contact time: 5 h)	35
Figure 3.5. Arsenic uptake on FRM versus adsorption time at different initial arsenic concentrations (a) pure As(III) (b) pure As(V). (initial arsenic concentration: 1, 2, and 4 mg/L, adsorbent amount: 1 mg/L, pH: 2.0, temperature: 25°C.	36
Figure 3.6 Linearized pseudo-second-order reaction kinetics of As(III) and As(V) on FRM. (initial arsenic concentration: 1, 2, and 4 mg/L, adsorbent amount: 1 mg/L, pH: 2.0, temperature: 25°C).....	38
Figure 3.7. Analysis of adsorption process using external diffusion model (a) pure As(III) (b) pure As(V). (initial arsenic concentration: 1, 2, and 4 mg/L, adsorbent amount: 1 mg/L, pH: 2.0, temperature: 25°C)	40

Figure 3.8. Analysis of adsorption process of arsenic onto FRM using intraparticle diffusion model (a) pure As(III) (b) pure As(V). (initial arsenic concentration: 1, 2, and 4 mg/L, adsorbent amount: 1 mg/L, pH: 2.0, temperature: 25°C).....	42
Figure 3.9. Adsorption isotherm of As(III) and As(V) on the FRM (initial arsenic concentration: 0.04-20 mg/L, adsorbent amount: 1 mg/L, pH: 2.0 and 7.0, temperature: 25°C and contact time: 5 h).....	44
Figure 4.1. XRD patterns of iron deposited AC	56
Figure 4.2. Iron deposited AC and ACO with various heating times	58
Figure 4.3. Close up of iron deposited ACO heated for 9 minutes.....	58
Figure 4.4. Nitrogen adsorption and desorption isotherms of ACO samples prepared at different heating durations	59
Figure 4.5. Adsorption isotherm of As(V) adsorbed by (a) AC-3min, (b) ACO-3min, (c) AC-9min and (d) ACO-9min (initial concentration = 0.5–20 mg/L, pH = 7.0, S:L = 750 mg/L, contact time = 24 h).....	63
Figure 4.6. Kinetic profile and pseudo second order model fit of As(V) onto (a) AC-9min, and (b) ACO-9min (initial concentration = 5.0 mg/L, pH = 7.0, S:L = 750 mg/L).	66
Figure 4.7. Intraparticle diffusion model fit of As(V) onto AC-9min, and ACO-9min (initial concentration = 5.0 mg/L, pH = 7.0, S:L = 750 mg/L)	68
Figure 4.8. Adsorption of As(V) as a function of pH and by pH_{final} versus $pH_{initial}$ for (a) AC0, (b) ACO-9min, and (c) AC-9min (initial concentration = 5.0 mg/L, S:L = 750 mg/L, contact time = 24 h).....	70
Figure 5.1. XRD pattern of the synthesized anatase nanoadsorbent.....	76
Figure 5.2. Raman spectra of the synthesized anatase nanoadsorbent.	77
Figure 5.3. SEM image of (in lens detector) the synthesized anatase nanoadsorbent... ..	78
Figure 5.4. XPS spectra of (a) survey scan, (b) Ti2p, (c) O1s of anatase nanoadsorbent surface at pH 6.0	79
Figure 5.5. Kinetic modeling of sorption of (a) As(III), (b) Pb(II), and (c) Cu(II) onto synthesized anatase nanoparticles [Temperature = 25°C, pH = 6.0, S:L = 500 mg/L]	82
Figure 5.6. Adsorption isotherm of (a) As(III), (b) Pb(II), and (c) Cu(II) adsorbed by synthesized anatase nanoparticles [Initial concentration = 0.3–20 mg/L, Temperature = 25°C, pH = 6.0, S:L = 500 mg/L]	87

Figure 5.7. (a) Adsorption of 10 mg/L Pb(II), Cu(II), and As(III) as a function of pH by 500 mg/L synthesized anatase nanoparticles 25 °C (b) pH _{final} versus pH _{initial} during the adsorption.....	93
Figure 5.8. XPS spectra of O1s after (a) Pb(II), (b) Cu(II), (c) As(III) adsorption at pH 6.0	96
Figure 5.9. XPS (a) Pb 4f, (b) Cu 2p, (c) As 3d XPS core-level spectra on the anatase nanoadsorbent surface after adsorption at pH 6.0.....	98
Figure 6.1. SEM images of TiO ₂ (a) , 40-AC/TiO ₂ (b) 20-AC/TiO ₂ (c) , 10-AC/TiO ₂ (d) and AC (e)	104
Figure 6.2. XRD patterns of the TiO ₂ , AC, and AC/TiO ₂ nanocomposites	105
Figure 6.3. Raman spectra of AC, 10-AC/TiO ₂ , 20-AC/TiO ₂	106
Figure 6.4. TGA curves of the TiO ₂ , AC, and AC/TiO ₂ nanocomposites.....	107
Figure 6.5. Nitrogen adsorption/desorption isotherms of AC and AC/TiO ₂ nanocomposites.....	108
Figure 6.6. Effect of contact time for As(III) adsorption onto TiO ₂ , AC, and AC/TiO ₂ nanocomposites [Temperature = 25°C, pH = 7.0, S:L = 500 mg/L].	109
Figure 6.7. Intraparticle diffusion model for the As(III) adsorption onto the TiO ₂ and AC/TiO ₂ nanocomposites	111
Figure 6.8: Adsorption isotherm of As(III) onto TiO ₂ (a), 10-AC/TiO ₂ (b) 20-AC/TiO ₂ (c), 40-AC/TiO ₂ (d) [Initial concentration = 0.5–17 mg/L, Temperature = 25°C, pH = 7.0, S:L = 500 mg/L].	115
Figure 6.9. Adsorption of 5 mg/L As(III) as a function of pH by 500 mg/L adsorbent materials 25 °C (a) and pH _{final} versus pH _{initial} during the adsorption (b)	118
Figure 6.10. Desorption capacity of 10-AC/TiO ₂ nanocomposite for As(III) with the different eluting solutions	119
Figure 6.11. Regeneration of 10-AC/TiO ₂ nanocomposite for As(III) with the increase of cycle number	120
Figure 7.1. XRD spectra of the TiO ₂ nanoparticles and commercial anatase powder (a) , SEM images of the TiO ₂ nanoparticles at 20 kX (b) and 120 kx (c)	126
Figure 7.2. Effect of pH on the adsorptions of As(III) and As(V) [Adsorbent amount: 0.5 g/L, initial arsenic concentration: 4.5 mg/L reaction temperature: 25°C]	127
Figure 7.3. Time dependence of As(III) (a) and As(V) (b) adsorbent amount, 0.5 g/L; initial arsenic concentration: 4 mg/L, pH, ~ 6 for As(III) and ~ 4 for As(V). The inset of	

figure represents pseudo second order curve for adsorption of As(III) and As(V) on TiO ₂ nanoparticles	129
Figure 7.4. Effect of UV-A light interaction time on As(III) adsorption from water by TiO ₂ nanoparticles.	131
Figure 7.5. Residual arsenic concentrations versus pH considering with and without UV-A illumination by using TiO ₂ nanoparticles	132
Figure 7.6. Adsorption isotherm of As(III) (a) , As(V) (b) and UV-light illuminated As(III) (c) onto TiO ₂ nanoparticles.....	134
Figure 7.7. Langmuir and Freundlich plots of the adsorption data of As(III) (a) , As(V) (b) and UV-light illuminated As(III) (c) in the concentration range from 1 to 25 mg/L.	135
Figure 7.8. The linearized graph of DKR isotherm for As(III), As(V), and UV-illuminated As(III)	138

LIST OF TABLES

Table 2.1. Global Arsenic Contamination In Ground Water [9].....	6
Table 2.2. Acidity constants for As(V) and As(III) [10].....	9
Table 2.3. Chemical compositions of the RM.....	19
Table 3.1. Parameters of pseudo first order and pseudo second order kinetic models for adsorption of As(III) and As(V) on FRM at pH 2.0	39
Table 3.2. Parameters of external diffusion and intraparticle diffusion models for adsorption of As(III) and As(V) on FRM at pH 2.0	43
Table 3.3. Calculated isotherm parameters for As(III) and As(V) adsorption onto FRM at pH 2.0 and 7.0.	46
Table 3.4. Comparison of adsorption performance of tested adsorbent with previous works.....	49
Table 4.1. Surface area and pore structure parameters for iron deposited AC & ACO .60	
Table 4.2. Iron loading on AC & ACO.....	61
Table 4.3. Langmuir, Freundlich, and Sips isotherm parameters for fresh and iron deposited AC and ACO.....	64
Table 4.4. The kinetic sorption modelling parameters of As(V) on AC-9min and ACO-9min.	67
Table 5.1. The kinetic sorption modelling parameters of Pb, Cu, and As on the anatase nanoparticles at pH 6.0.	83
Table 5.2. Langmuir, Freundlich, Redlich_Peterson, and Sips, isotherm parameters for Pb(II), Cu(II), and As(III) removal on the anatase nanoparticles.....	88
Table 5.3. Thermodynamic parameters for Pb(II), Cu(II), and As(III) sorption on the anatase nanoparticles	89
Table 6.1. Structural characteristic parameters of AC and AC/TiO ₂	108
Table 6.2. The kinetic sorption modeling parameters for As(III) adsorption.	110
Table 6.3. Parameters of intraparticle diffusion model for As(III) adsorption	112
Table 6.4. Sorption isotherm parameters for As(III) removal onto TiO ₂ and AC/TiO ₂	116
Table 7.1. The kinetic sorption modeling parameters for As(III) and As(V) adsorption on to TiO ₂ nanoparticles.....	130
Table 7.2. Adsorption isotherm parameters for As(III) with/without UV illumination and As(V) by using TiO ₂ nanoparticles.....	137

LIST OF SYMBOLS AND ABBREVIATIONS

AC	: Activated Carbon
APE	: Average percent error
BET	: Brunauer Emmett Teller
BJH	: Barrett Joyner Halenda
DKR	: Dubinin-Kaganer-Radushkevich
FT-IR	: Fourier Transformed Infrared Spectroscopy
FRM	: Ferric Ion Loaded Red Mud
MCL	: Maximum Contamination Level
RM	: Red Mud
SEM	: Scanning Electron Microscopy
TEM	: Transmission Electron Microscopy
TTIP	: Titanium Tetra Isopropoxide
TGA	: Thermal Gravimetric Analyzer
PZC	: Point of Zero Charge
WHO	: World Health Organization
XRD	: X-ray Diffraction
XPS	: X-ray Photoelectron spectrometer
A	: Intraparticle diffusion constant
a_{RP}	: Redlich-Peterson isotherm constant (L/mg)
a_{LF}	: Sips isotherm constant
b	: Adsorption equilibrium constant (L/mg)
C_o	: Initial solution concentration (mg/L)
C_e	: Liquid phase sorbate concentration in equilibrium (mg/L)
D_{XRD}	: Average crystallite size
E	: Free energy of adsorption
k_1	: Pseudo first order rate constant for the arsenic adsorption process (min^{-1})
k_2	: Pseudo second order rate constant (g/mg min)
k_{ext}	: External diffusion rate constant (1/min)
k_{int}	: Internal diffusion rate constant ($\text{mg}/(\text{g min}^{0.5})$)
K_c	: Equilibrium constant (L/g)

K_F	: Adsorbent's relative adsorption capacity (mg/g)
K_{RP}	: Redlich-Peterson isotherm constant (L/g),
K_{LF} ,	: Sips isotherm constant (mg/L)
n	: Freundlich constant representing adsorption intensity
R_L	: Dimensionless constant separation factor
R	: Ideal gas constant
R^2	: Correlation Coefficient
q_t	: Amount of sorbate adsorbed (mg/g) at time t
q_e	: Solute amount adsorbed per unit weight of adsorbent (mg/g)
q_{mon}	: Monolayer adsorption capacity (mg/g)
q_{exp}	: Experimental uptake value
q_{cal}	: Calculated uptake value
X_m	: Adsorption capacity (mol/g)
ΔG	: Free energy change
ΔH	: Enthalpy change (kJ/ mol)
ΔS	: Entropy change (kJ/mol K)
ε^2	: Polanyi potential
λ	: Average wavelength of the X-ray radiation,
β	: Full width at half-maximum peak position
β_{RP}	: dimensionless constant of Redlich-Peterson isotherm
θ	: Diffracting angle

CHAPTER 1

INTRODUCTION

Water, as a universal solvent for many reactions including metabolic processes within the body, is one of the vital components for the continuity of life on earth. The threats of long-term water shortages driven by population growth and climate change are forcing researchers to find a way to treat water contaminated with heavy metal and arsenic. Specifically, rapid industrialization is the major cause for introducing heavy metal and arsenic contaminants to the water.

The existence of heavy metals and arsenic in water supplies may cause severe effects on health, environmental toxicity, and affect the quality of the water environment [11]. Arsenic and lead may accumulate in the body and can reach toxic levels. Arsenic is the most dangerous as it can cause lung, liver, kidney, skin, and bladder cancers. Long-term consumption of even low levels of arsenic could be dangerous [12]. Lead also can cause serious health problems, such as damage to the brain and kidneys, and may cause lowered intelligence in children. Furthermore, in the case of women, lead is stored in the bones, and it can be released later in life and during pregnancy [13]. Copper is essential elements for good health, but like all heavy metals, an excess of the metals can be harmful. For instance, copper excess can cause Wilson's disease [14]. Arsenic, lead, and copper are naturally occurring contaminants of groundwater and surface water. Arsenic is introduced into environment by geochemical reactions, natural weathering reaction, mining activities, industrial wastes and volcanic emissions [9]. Lead and

copper may enter drinking water after the treatment process due to the corrosion of pipes or faucets made of lead and copper. The primary sources of copper in drinking water are corrosion of household plumbing systems, erosion of natural deposits, and leaching from wood preservatives. The current allowable concentrations of lead, arsenic, and copper in drinking water as set by the United States Environmental Protection Agency (U.S. EPA) are 15 ppb, 10 ppb, and 1.3 parts per million (ppm), respectively [15].

The most common methods, which have been used for removal of heavy metal ions from an aqueous medium, contain solvent extraction, ultra-filtration, reverse osmosis, electro dialysis, chemical precipitation, ion exchange, and adsorption[16-19]. Among these water treatments, adsorption is the most preferred method for removal of heavy metal ions since it is a highly efficient method with low cost and a range of different adsorbents. The adsorbents, which are extensively used for heavy metal removal, include activated carbon, zeolites, sawdust, fly ash, chitosan, activated alumina, and iron oxide particles [20-23].

The new promises that nanotechnology have encouraged the industry to focus their research and investments on developing new applications for the nanomaterials. It is estimated that the United States federal government has invested approximately one billion dollars, while the total worldwide investments were greater than three billion dollars in 2005 alone [24]. Although used in many fields such as medicine, biotechnology and electronics, the beneficial applications of nanotechnology in drinking water treatment are only recently initiated [25-27]. As a consequence of their size, nanomaterials can exhibit an array of unique novel properties, which can be utilized in development of new heavy metal and arsenic treatment technologies. Some of their properties, such as high surface area, self-assembly, and high specificity make them an excellent candidate for removal of heavy metals and arsenic from water by adsorption. Particularly, metal oxide nanomaterials can interpret better heavy metal and arsenic removal properties of an adsorbent compared to conventional porous metal oxide particles.

Iron oxide, which is one of the widely used metal oxides as an adsorbent, exists in many forms in nature. Magnetite (Fe_3O_4), maghemite ($\gamma\text{-Fe}_2\text{O}_3$), and hematite ($\alpha\text{-Fe}_2\text{O}_3$) are

the most common forms [28]. In recent years, the synthesis and utilization of adsorbent materials with iron oxide, which includes novel properties and functions, have been widely studied [29]. Additionally, iron oxide with low toxicity, chemical inertness and biocompatibility may show a tremendous potential in combination with other materials [30].

Titanium dioxide (TiO_2) has many properties such as non-toxicity, inertness, high refractive index, hydrophilicity, and low cost [31]. In addition, TiO_2 is well known as a matter with a high photocatalytic activity due to its strong oxidizing power and favorable band gap energy. These desired properties make TiO_2 an excellent choice and it has been extensively tested in environmental applications, especially in adsorption technologies on removal of heavy metals and arsenic. Moreover, the high mobility and reactivity of TiO_2 nanoparticles due to their small size; make TiO_2 particles effective as an adsorbent material. TiO_2 nanoparticles have the ability to hold onto heavy metal ions and collect them from water. As the oxidation states of the heavy metals become more stable, they turn into more toxic structures since they can go into a reaction with bio-molecules of body and construct bio-toxic complexes that are very stable [32]. As^{3+} is of the most toxic arsenic forms that are mostly cause water pollution and TiO_2 has the capability of converting stable forms into less toxic and more adsorbable forms under UV radiation [33].

Although the properties, such as high surface area, self-assembly, and high specificity make nanomaterials excellent candidates for removal of heavy metals and arsenic from water by adsorption, these properties also bring some disadvantages for human health. For instance the nanoparticles can easily go into the body through inhalation; ingestion due to their small size and this problem can restrict the application of the nanoparticles for water remediation [34]. In order to solve this problem, nanoparticles can be immobilized by embedding them onto a bulk material. This provides the prevention of release of the nanoparticles to the environment and at the same time, the reactivity of them will be preserved.

While the primary goal of the thesis is to demonstrate nanomaterial synthesis to engineer adsorbents for environmental pollutants, the secondary goal is to determine extent of adsorption of arsenic, lead, and copper onto low-cost nanomaterials with a

series of adsorption and photocatalytic oxidation experiments in order to investigate an effective and inexpensive water purification system for communities that cost less and is easy to operate, and produced drinking water with a high quality. The specific objectives of the study involved two major technological practices for water treatment i.e. adsorption and photocatalysis, which encompass five separate research and development stages. These include:

(1) Evaluation, modification and characterization of ferric ion loaded red mud minerals as alternative low-cost adsorbents for As(III) and As(V) removal.

(2) Evaluation of the impact of synthesis conditions (e.g. iron concentration, and contact time) on the distribution of iron (hydr)oxide nanomaterials derived from Fe(III) inside activated carbon media, oxidized with KMnO₄, and the consequent impact on As(V) removal.

(3) Synthesis and characterization of TiO₂ nanoparticles with sol-gel method and evaluation of the arsenic, lead, and copper removal capabilities, kinetics and adsorption mechanisms of the nanoparticles.

(4) Preparation and characterization of activated carbon/TiO₂ nanocomposites and the evaluation of As(III) adsorption capabilities of activated carbon /TiO₂ nanocomposites, activated carbon, and TiO₂ in terms of contact time and pH

(5) Synthesis of anatase nanophotocatalyst and integration of the adsorption-photocatalysis process for the removal of As(III) and As(V) species from water

CHAPTER 2

LITERATURE SURVEY

The literature review mainly pointed out three topics. First, the significance of arsenic, lead, and copper removal from drinking waters were considered in terms of their effects on human health and their chemistry, mobility, and redox reactions. Second, the water treatment techniques and their efficiency to remove arsenic, lead, and copper from aqueous solution were explained. Finally, the types of adsorbents that were used in removal of arsenic, lead, and copper were concerned.

2.1. Contaminations in Natural Water

2.1.1. Arsenic

Excessively high arsenic concentration in water/wastewater is threatening environmental problem for many countries especially in Bangladesh, India, Germany, China and Turkey [35]. Additionally, many parts of European countries have also had arsenic concentration higher than 10 $\mu\text{g/l}$ in ground water [36]. As shown in Table 2.1, the largest population at risk among the 14 countries with known groundwater arsenic contamination is in Bangladesh, followed by West Bengal in India [9, 37, 38].

Table 2.1. Global Arsenic Contamination In Ground Water [9]

Country /region	Potential exposed population	Concentration($\mu\text{g/L}$)
Bangladesh	30,000,000	< 1 to 2,500
West Bengal, India	6,000,000	< 10 to 3,200
Argentina	2,000,000	< 1 to 9,900
Vietnam	>1,000,000	1 to 3,050
Inner Mongolia	100,000 to 600,000	< 1 to 2,400
Chile	400,000	100 to 1,000
Mexico	400,000	8 to 620
Romania	400,000	< 2 to 176
Taiwan	100,000 to 200,000	<1 to 2,500
Greece	150,000	-
Spain	>50,000	1 to >100
Germany	-	< 10 to 150
Xinjiag, Shanxi	500	40 to 750
Usa / Canada	-	< 1 to > 100,000

Water is one of the most significant media that makes enable arsenic to enter into human body [39]. Due to its toxic and carcinogenic effects on human beings, the maximum contamination level of arsenic (MCL) in water has taken serious consideration by environmental authorities and the World Health Organization (WHO), has adopted 10 $\mu\text{g/L}$ as a maximum contamination level of arsenic in drinking water [40].

Although arsenic is essential as a nutrient for humans in small quantities, it can cause to death in chronic consumptions [41]. Humans are exposed to arsenic from air, food, and water and the deadly dosage for adults is 1-4 mg As/kg body weight. The most significant source of arsenic exposure is ingestion of drinking water since the arsenic levels are generally highest in groundwater where geochemical conditions increase the dissolution of arsenic [42]. The arsenic poisoning of ground water was first reported in Taiwan in 1968 [43]. Arsenic exposure can cause short and long term health problems in both humans and animals. Acute poisoning with arsenic in humans may produce dryness of mouth and throat, dysphasia, vomiting, severe diarrhea, and hematuria. Sub-acute toxicity can result in loss of appetite, nausea possibly with vomiting, dry throat, sharp pains, diarrhea and erythema. Chronic exposure to sub-acute levels of arsenic can produce dry, loose hair, brittle nails, and eczema [38]. Chronic exposure to high levels

of arsenic in drinking water can also lead to long term damage to internal organs in the respiratory, digestive, circulatory, neural, and renal systems. Additionally, long-term exposure to arsenic can result in skin, lung, and bladder cancer [12].

Arsenic is mobilized by natural conditions and anthropogenic activities, however most environmental arsenic problems result from the natural conditions which contain geochemical reactions, weathering reactions, biological activity, wind erosion and volcanic emissions [35]. In addition to natural sources, arsenic can also be introduced by the man-made sources into water. The wastes from mining operations, the smelting of metal ores, the use of particular pesticides and wood preservatives including arsenic can contribute to the presence of arsenic in the water environment [38].

In the environment, arsenic occurs in different oxidation states that form various species. Arsenic is presented as arsenate with an oxidation state of +5 or arsenite with an oxidation state of +3 [44]. The toxicity of arsenic is associated with its chemical form that is governed by the valence state. When arsenic forms complexes with organic compounds it becomes mostly less toxic than inorganic forms of arsenic. The toxicity level of arsenic decreases in the following order: arsine > inorganic arsenic (III) > organic arsenic(III) > inorganic arsenic(V) > organic arsenic(V) > arsonium compounds and elemental arsenic [45].

The organic and inorganic forms of arsenic are illustrated in Figure 2.1. Two inorganic forms of arsenic are common in natural waters: arsenite (AsO_3^{3-}) and arsenate (AsO_4^{3-}), referred to as As(III) and As(V). As(III) is a hard acid and specifically makes complexes with oxides and nitrogen. However As(V) behaves like a soft acid, forming complexes with sulfides. Organic arsenic species which are mono methyl arsenate (MMA) and dimethyl arsenate (DMA) available in contaminated surface and ground water [46]. They are widespread in surface water more often than in groundwater and they are rarely present at concentrations higher than 1 $\mu\text{g/L}$. Therefore, organic species are mostly considered less significant in contrast to inorganic arsenic species in drinking water treatment [47]. Although organic arsenic is detoxified by methylation process, inorganic arsenic is needed a well-established treatment [48].

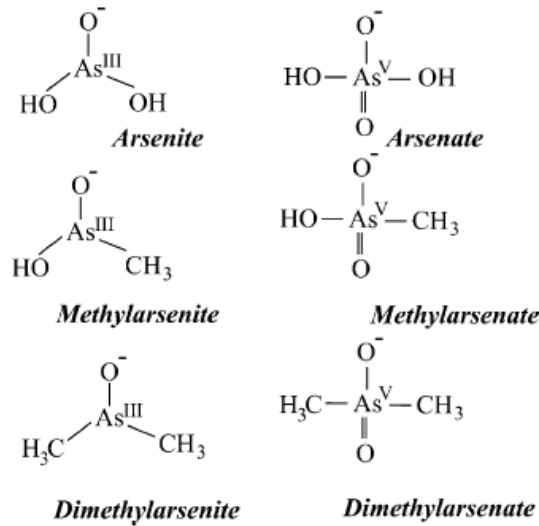


Figure 2.1. Arsenic species found in water.

Especially, As(III) has greater toxicity (25–60 times) and mobility than As(V) since preferential reactions with sulfhydryl groups in mammalian enzymes [49]. As(V) generally reveals a low mobility in aquifer and sediment systems due to its retention on mineral surfaces controlled largely by adsorption reactions with metal hydroxide [50]. Arsenic speciation graphs as a function pH is illustrated in Figure 2.2. H_2AsO_4^- dominates at low pH (less than about pH 6.9) in oxidizing conditions while at higher pH, HAsO_4^{2-} is the dominant form. Moreover, H_3AsO_4 and AsO_4^{3-} may be present in strong acid or base conditions, respectively. Under reducing conditions at $\text{pH} < \sim 9.2$, the uncharged H_3AsO_4 predominates [35].

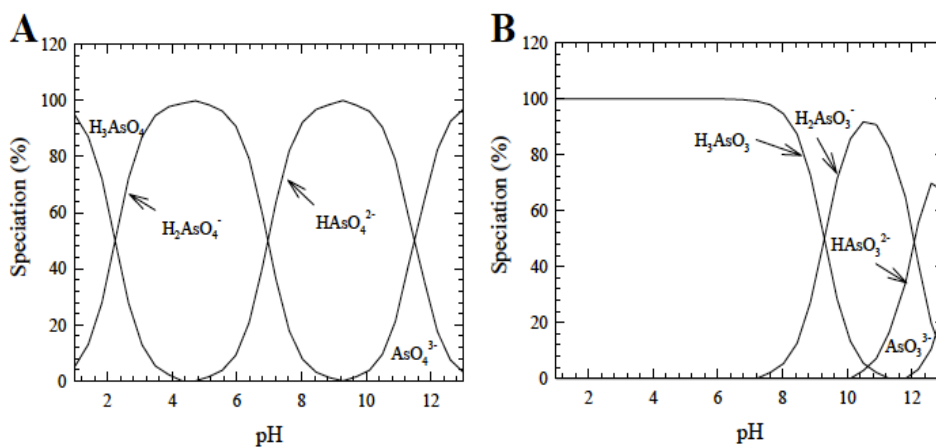


Figure 2.2: (a) Arsenate and (b) Arsenite speciation as a function of pH [1].

Deprotations of arsenious (H_3AsO_3) and arsenic (H_3AsO_4) acids under different conditions are summarized in Table 2.2 with the respective pK_a values [51]. The conversion of As(III) to As(V) in oxygenated water is thermodynamically favored, but the rate of the transformation may take days, weeks or months. However, strong acidic or alkaline solutions, the presence of copper salts, carbon, unknown catalysts and higher temperatures can increase the oxidation rate. In contrast, the reduction of As(V) to As(III) in anaerobic conditions may require bacterial mediation since the conversion is chemically slow [52].

Table 2.2: Acidity constants for As(V) and As(III) [10]

Reaction	pK_a
As(V) (arsenic acid)	
$\text{H}_2\text{AsO}_4^- + \text{H}^+ \rightarrow \text{H}_3\text{AsO}_4$	2.24
$\text{HAsO}_4^{2-} + \text{H}^+ \rightarrow \text{H}_2\text{AsO}_4^-$	6.96
$\text{AsO}_4^{3-} + \text{H}^+ \rightarrow \text{HAsO}_4^{2-}$	11.50
As(III) (arsenous acid)	
$\text{H}_2\text{AsO}_3^- + \text{H}^+ \rightarrow \text{H}_2\text{AsO}_3$	9.22
$\text{HAsO}_3^{2-} + \text{H}^+ \rightarrow \text{H}_2\text{AsO}_3^-$	12.11
$\text{AsO}_3^{3-} + \text{H}^+ \rightarrow \text{HAsO}_3^{2-}$	13.41

2.1.2. Lead

Lead, which is one of the most toxic heavy metals, is attracting comprehensive attention of environmentalists because of its acute and chronic toxic effects in human health. According to the list organized by the Agency for Toxic Substances and Disease Registry (ATSDR) in 2011, lead is ranked as second hazardous heavy metals among the substances after arsenic [53].

Lead, abundant in the environment, can enter the human body through uptake of food, water and air. The combustion of fossil fuels and the smelting of sulfide ore, and into lakes and streams by acid mine drainage are the main reasons for lead contamination in water. Additionally, process industries, such as battery manufacturing, metal plating and finishing are also major source of lead pollution [54]. In acute and long-term exposure, lead can cause numerous undesirable effects, such as gastrointestinal symptoms, sleeplessness,

headaches, abdominal cramps, kidney damages and loss of memory. Moreover, renal diseases and increased of blood hypertension also have been interconnected with lead poisoning [55]. In addition to that, infants, children up to 6 years of age, the fetus, and pregnant women are the most susceptible to adverse health effects of lead. Current EPA drinking water standard for lead are 0.05 mg/L, but the level 0.02 mg/L is under review [56].

A speciation diagram for a 3×10^{-4} M solution is plotted in Figure 2.3. In aqueous solution at $\text{pH} < 10$, divalent lead speciation is generally cationic; the major species are Pb^{2+} , PbOH^+ and $\text{Pb}_3(\text{OH})_4^{2+}$. Anionic $\text{Pb}(\text{OH})_3^-$ is only found under alkaline conditions. $\text{Pb}(\text{OH})_2(\text{aq.})$ is the prevalent molecule at pH 10, however because of the low solubility constant of $\text{Pb}(\text{OH})_2(\text{s})$ it precipitates at high lead concentration (when the total lead concentration is $> 10^{-4}$ M) [2].

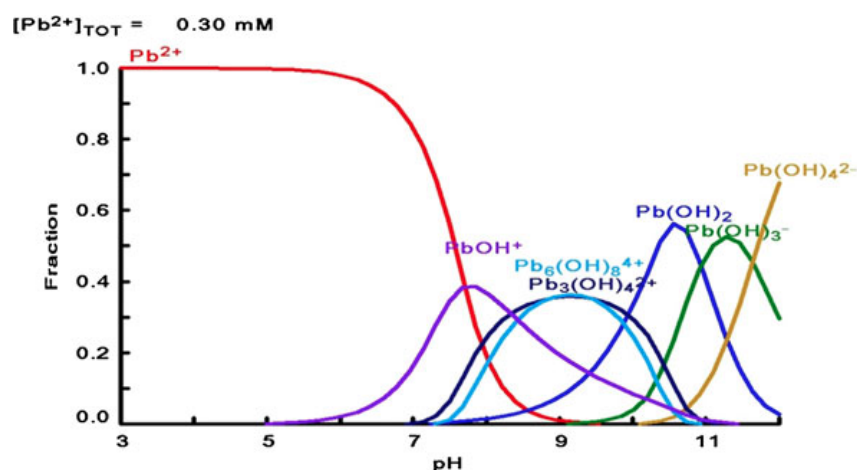


Figure 2.3. Distribution of Pb(II) species at 25 °C [2]

2.1.3. Copper

Copper, which is an important catalyst for synthesis various materials, is essential element of humans and living organism in small amount. Following zinc and iron, copper is the third most abundant trace element in the body [57]. Although copper is essential element in the human body, it can cause adverse health effect. The excessive exposure to copper above the limit value, the health problems varying from stomach

distress to excessively damage caused by vomiting, diarrhoea, stomach cramps and nausea can be observed [58]. Moreover, long-term exposure to copper is correlated with liver damage and kidney disease. Although the human body has a natural mechanism for keeping the proper level of copper, children under one year old are more vulnerable to the toxic effects of copper. People with Wilson's disease also have a problem with maintaining the proper balance and taking care to limit the exposure of copper [14]. According to World Health Organization the maximum acceptable concentration of Cu (II) in drinking water is 1.3 mg/L [59] .

The main concentration of copper in atmosphere is ranging from 5–200 ng/m³. It is releasing to atmosphere by natural source (windblown dust 65%, volcanoes, forest fire and sea spray) and anthropogenic source (nonferrous metal production 3.3%, copper smelters and copper sulphate production 2.7%, coal and oil combustion 4.6%, iron and steel production 7.4%, municipal incinerators 1.9% others 2.3%) [60]. There are also many other factors that affect the amount of copper in drinking water such as the temperature of water in pipe and copper availability in the distribution system. Figure 2.4 interpreted the speciation diagram of copper in water. Copper exists in both the free state and in hydroxyl forms. Among all the forms free Cu²⁺ ions and Cu⁺ are considered to be highly toxic as compared to the anionic complexes such as carbonate complexes [61].

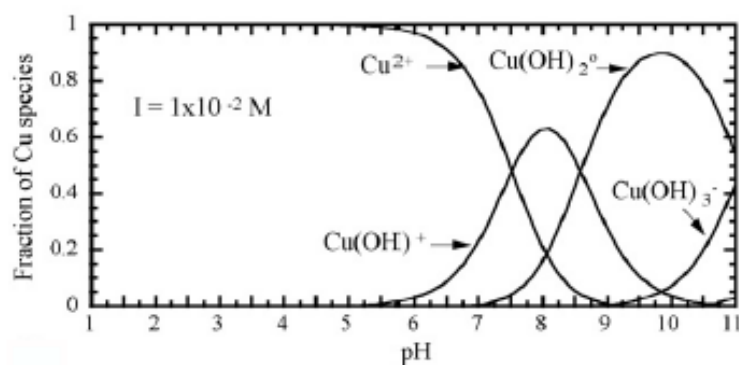


Figure 2.4. The speciation diagram of copper in water [3]

2.2. Removal Technologies in Wastewater Treatment

Many technologies have been developed for the removal of arsenic and heavy metals. The water treatment processes can be categorized based on the mechanisms involved; precipitation and coagulation, ion exchange, oxidation, membrane technology, and adsorption. All of these technologies which rely on various chemical processes for the removal of lead, copper, and arsenic were summarized in the below.

2.2.1. Precipitation and Coagulation Processes

Precipitation process results in low-solubility solid mineral from dissolved contaminants. The solid can then be removed through sedimentation and filtration. The contaminants can become insoluble by presenting coagulants in the solution and they form solid complexes known as co-precipitation.

Precipitation/ coagulation are the most commonly used technologies for the removal of arsenic from surface and groundwaters, gaining residual arsenic concentrations in the range of 5-10 $\mu\text{g/L}$ with having the initial arsenic concentrations in the range of 10-500 $\mu\text{g/L}$ [52]. However, direct precipitation has not been shown to play a significant role in the arsenic removal. Thus co-precipitation and filtration are needed to activate arsenic removal mechanisms.

The most frequently used metal salts are ferric salts such as ferric chloride or ferric sulfate and aluminum salts such as alum. Ferrous sulfate has seldom been used since it is less effective [39]. This treatment can provide advantages in terms of simple in operation and relatively low cost. However, the optimal conditions vary for removal of different constituents, and coagulation to remove contaminants may not be optimal for removal of other compounds, especially phosphate and fluoride in the case of arsenic removal [35]. For example, aluminum coagulation can produce toxic sludges with having low arsenic and heavy metal removal efficiencies. Although iron coagulation

provides medium arsenic removal efficiency, which is higher than aluminum coagulation, it requires readjustment of pH during the co-precipitation process.

2.2.2. Ion exchange processes

Ion exchange involves the reversible displacement of an ion adsorbed onto a solid surface by a dissolved ion. The resins have been developed specifically to optimize removal of contaminants from water. Different resins will have various selectivity sequences. For example, the acidic resins are negatively charged, and can be loaded with cations (e.g. Na^+), which are easily displaced by other cations during water treatment. This type of cation exchange is most commonly used for heavy metal removal. Conversely, strongly basic resins can be pretreated with anions, such as Cl^- , and used to remove a wide range of negatively charged species [62]. The anion exchange resin can be applied to arsenic species, which is also negatively charged. The typical anion exchange process is illustrated at Figure 2.5. In this system an ion exchange resin loaded with anions at the “exchange sites”, is placed in vessels. The water containing negatively charged contaminant is passed through the vessels and the contaminant “exchanges” for the anions. The water exiting the vessel is lower in the contaminant but higher in anion than the water entering the vessel. Finally, the resin becomes “exhausted”; that is, all or most of the “exchange sites” that were loaded with anions become loaded with contaminants [4].

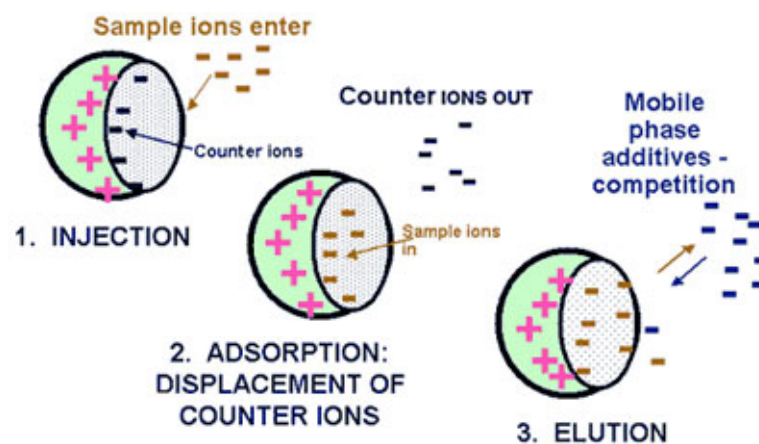


Figure 2.5. The illustration of ion exchange process [4].

The effect of the presence of other anions is an important factor to ion exchanger treatment of arsenic and heavy metals. Jackson and Miller [63] reported that sulfate was reported not to influence As(V) sorption by ferrihydrite but resulted in a considerable decrease in As(III) sorption below pH 7, with the largest decrease at the lowest pH. In low-sulfate waters, ion exchange resin can easily remove As(V), but removing As(III) species from water is quite difficult. Accordingly, the USEPA recommends that ion exchange resins not be used in waters with >120 mg/L sulfate and will be most effective in waters with even lower sulfate levels (<25 mg/L) [64]. Additionally, major disadvantage of ion exchange is that it is expensive in capital and operating cost.

2.5.3. Membrane Technology

Membrane filtration has the advantage of removing many contaminants from water, including bacteria, salts, and various heavy metals as can be seen in Figure 2.6. The structure of the membrane is such that some molecules can pass through, while others are excluded, or rejected. Two classes of membrane filtration can be considered; low-pressure membranes, such as microfiltration and ultrafiltration, and high-pressure membranes such as nanofiltration and reverse osmosis.

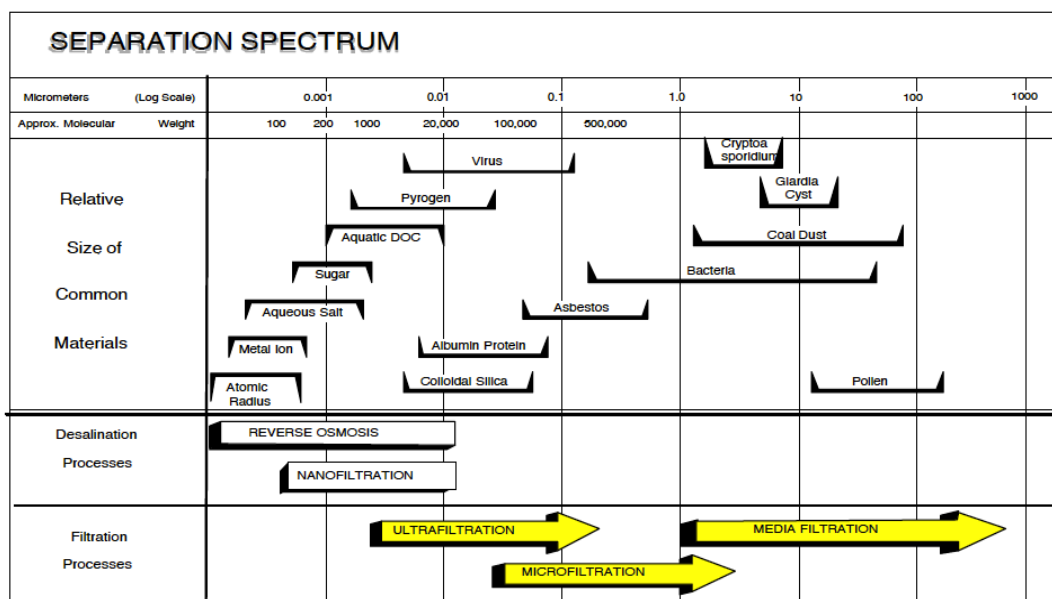


Figure 2.6. Pressure Driven Membrane Process Classification [5]

The main disadvantage of membranes is fouling by colloidal matter in the raw water, particularly with organic matter. Iron and manganese can also cause to membrane fouling [65]. To prevent fouling, reverse osmosis filters are almost always preconditioned by a filtration step. High technology operation cost and maintenance, and very high-capital and running cost is prohibiting to usage of membrane process in the removal of contaminants from water.

2.5.4. Oxidation Processes

In most arsenic removal technologies, the As(V) is most effectively removed from water than As(III) since As(III) is predominantly non-charged below pH 9.2 [66]. Therefore, various treatment systems contain an oxidation step to convert As(III) to As(V).

Ultraviolet radiation can catalyze the oxidization of As(III) in the presence of other oxidants, such as gaseous chlorine, hypochlorite, ozone, permanganate, hydrogen peroxide [67-70] Chlorine is a rapid and effective oxidant, but may result in reactions with organic matter, which produces toxic trihalomethanes as a by-product. In Europe and the USA, ozone is being used as an oxidant material, but in developing countries, ozone has not been so widely used. An ozone dose of 2 mg/L, contacted with the water for 1 minute prior to filtration, has been shown to be effective in oxidizing iron and manganese, at the same time removing arsenic and other metals to below detection limits [71]. At a similar ozone dose, As(III) was shown to have a half-life of approximately 4 minutes [68]. Hydrogen peroxide may be an effective oxidant if the raw water contains high levels of dissolved iron, which often occur in conjunction with arsenic contamination. Oxidation alone does not remove arsenic from solution; therefore it must be combined with a removal process such as coagulation, adsorption or ion exchange.

2.5.5. Adsorption Processes

Adsorption is the adhesion of a chemical species onto the surface of particles. In general, adsorption can be defined as accumulation or depletion of solute molecules at an interface. Adsorption is primarily described with intermolecular interactions between solute and solid phases [68]. The interactions can be surface complexation reactions, which are basically inner-sphere surface complexes of the metal or arsenic ions and the respective surface functional groups. Moreover the interactions can comprise in an account of the electrostatic interactions where the metal or arsenic ions form outer-sphere complexes at a certain distance from the surface [72]. In general, heavy metal and arsenic adsorption is explicated in terms of two essential mechanisms: specific adsorption, which is considered more selective and less reversible reactions comprising chemisorbed inner-sphere complexes, and nonspecific adsorption (ion exchange), which contains rather weak and less selective outer-sphere complexes. Specific adsorption result in strong and irreversible binding of heavy metal or arsenic ions onto adsorbent while nonspecific adsorption is an electrostatic phenomenon in which cations/anions from the pore water are replaced for cations/anions near the surface. Cation/anion exchange is a form of outer-sphere complexation with only weak covalent bonding between metals or arsenic ions and charged adsorbent surfaces. It is reversible in nature and occurs rather quickly as it is typical for reactions which are diffusion-controlled and of electrostatic nature [73]. Specific adsorption depends largely on pH due to formation of surface complexes by pH dependent species on the edges. Figure 2.7 interprets the possible specific and nonspecific adsorption of lead, copper, and arsenic onto adsorbent surface.

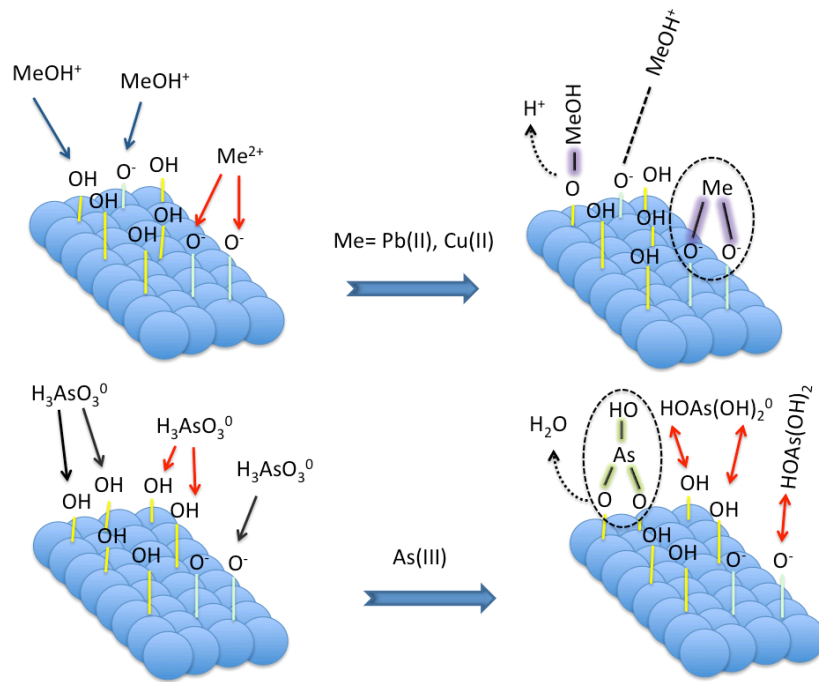


Figure 2.7. Illustration of specific and nonspecific adsorption.

The third fundamental mechanism of sorption is fixation (absorption), which includes the diffusion of heavy metal or arsenic species into the adsorbent surface. Heavy metals or arsenic that are specifically adsorbed onto clay minerals and metal oxides may diffuse into the lattice structures of these minerals. Then these species become fixed into the pore spaces of the adsorbent [72].

2.3. Types of Adsorbents Used in Water Treatment

Among the methods used for heavy metal and arsenic removal from water, adsorption is acquired importance due to its technical simplicity and applicability in rural areas, where people are more subjected to polluted drinking water [74]. For the adsorption of contaminants from water, several adsorbent materials have already been proposed. In terms of variety of different materials can be ranged from natural materials to specially designed technical particles. Especially, selective adsorption utilizing metal oxides, carbonaceous materials, and nanomaterials, has generated increasing excitement.

2.3.1. Low-Cost Adsorbents

Activated carbon (AC) has unquestionably been the most popular and widely used low-cost adsorbent in wastewater treatments all around the world. AC has been obtained from coconut shells, wood char, lignin, petroleum coke, bone-char, peat, sawdust, carbon black, rice hulls, sugar, peach pits, fish, fertilizer waste, waste rubber tire, etc [75]. They are produced by carbonization process, heating them in the absence of air below 600 °C to remove volatile compounds. Subsequently, chemical and physical activation steps are investigated using oxidizing agents (steam, carbon dioxide, or oxygen) at higher temperature or with chemical activants (ZnCl₂, H₂PO₄, H₂SO₄, KOH, K₂S, KCNS, etc.) Based on its shape and size, AC is categorized into four types: powder (PAC), granular (GAC), fibrous (ACF), and clothe (ACC). Because of the different sources of raw materials, each type of AC has its specific function as well as inherent disadvantages and advantages in water treatment. As can be seen in Figure 2.8, AC can comprise mesopores and micropores providing high surface areas up to 2000m²/g [76]. However, surface area may not be a leading factor for adsorption on activated carbon. Actually, high surface area does not mean high adsorption capacity. Although a significant number of low-cost adsorbents from various materials have been found, AC has still been used extensively today. Numerous researchers were studied to utilize AC for removing heavy metals such as mercury, arsenic, copper, lead, chromium, and zinc [77]. Recently the market price of AC for industrial grade is about US\$ 20–22.00/kg, depending on the quality of AC [78].



Figure 2.8. Activated carbon particles with the illustration of micro and mesopores

Red mud is a waste material that is formed during the production of alumina from bauxite. As can be seen in Table 2.3, it mineralogically consists mainly of different forms of iron and aluminum oxide minerals, calcium and sodium aluminum silicates and various titanium compounds [79]. In the study conducted by Altundogan et.al, red mud has been explored as an alternate adsorbent for arsenic and an alkaline aqueous medium (pH 9.5) favored As (III) removal, whereas the acidic pH range (1.0-3.2) was effective for As(V) removal [79]. In another study, Bauxsol combined by acid and heat treatment, and Bauxsol with added ferric sulfate or aluminum sulfate were investigated and it was found that the acid treatment alone, as well as in combination with heat treatment, increased arsenic removal efficiency. In contrast, the addition of ferric sulfate or aluminum sulfate suppressed arsenic removal [80].

Table 2.3. Chemical compositions of the RM.

<i>Constituent</i>	<i>% w/w</i>
Al ₂ O ₃	20.39
SiO ₂	15.74
Fe ₂ O ₃	36.94
CaO	2.23
Na ₂ O	10.10
V ₂ O ₅ – P ₂ O ₅	0.55
TiO ₂	4.98
CO ₂	2.04
S	0.08
Loss on ignition (900°C)	8.19

2.3.2. Iron Impregnated Adsorbents

Iron oxides exist in many forms in nature. Magnetite (Fe_3O_4), maghemite ($\gamma\text{-Fe}_2\text{O}_3$), and hematite ($\alpha\text{-Fe}_2\text{O}_3$) are the most common forms [28]. In recent years, the synthesis and utilization of adsorbent materials with iron oxide, which includes novel properties and functions, have been widely studied [29]. Additionally, iron oxide with low toxicity, chemical inertness and biocompatibility may show a tremendous potential in combination with other materials [30].

When FeCl_3 is added to water, it hydrolyzes to form ferric hydroxide [$\text{Fe}(\text{OH})_{3(s)}$], which has a net positive charge on the surface of the particles formed. The net positive charge of $\text{Fe}(\text{OH})_{3(s)}$ particles changes relying on the pH of solution, and as the pH of solution decreases, the number of positively charged sites on the $\text{Fe}(\text{OH})_{3(s)}$ particles increases. According to ferric hydroxide speciation diagram (Figure 2.9), a pH around 7.3 is required for $\text{Fe}(\text{OH})_{3(s)}$ particles to have a net positive charge [6].

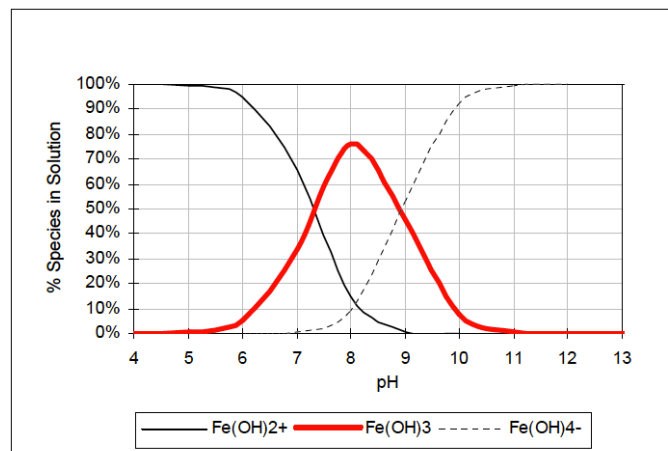


Figure 2.9 Ferric hydroxide speciation [6].

The combination of AC and iron loading would take advantage of the strength of these two materials. The AC serves as an ideal support media for iron loading. Recently, various researchers have studied arsenic removal from water using iron impregnated GAC. These studies analyzed the removal of arsenic, mercury, and lead using iron-impregnated GAC (Fe-GAC) [81, 82], As(V) removal by iron-impregnated GAC [83].

2.3.3. Nanoadsorbents

Utilization of specific nanoparticles either embedded in supporting structural media that can effectively, inexpensively and rapidly treat water contaminant with heavy metals and arsenic. The use of nanoparticles for treatment of wastewater may potentially provide greater advantages over the traditional adsorbents. Figure 2.10 highlights four classes of nanoscale materials that are being evaluated as functional materials for (1) metal containing nanoparticles, (2) carbonaceous nanomaterials, (3) zeolites and (4) dendrimers. These have a broad range of physicochemical properties that make them specifically attractive as reactive and separation media for water treatment.

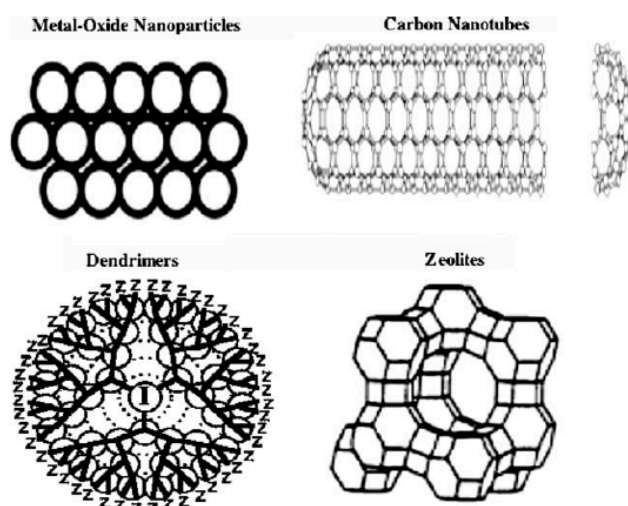


Figure 2.10. Selected nanomaterials currently being evaluated as functional materials for water purification [7].

Nanoparticles have two significant properties that make them precisely attractive as adsorbents. First, they have much larger surface areas than bulk particles; second, nanoparticles can be functionalized with various chemical groups to increase their affinity towards target compounds. Numerous research groups are utilizing the unique properties of nanoparticles to develop high capacity and selective adsorbents for heavy metal and arsenic species. Li et al. [84] have investigated the sorption of Pb(II), Cu(II) and Cd(II) onto multiwalled carbon nanotubes (MWCNTs). They reported maximum sorption capacities of 97.08 mg/g for Pb(II), 24.49 mg/g for Cu(II) and 10.86 mg/g for Cd(II) at room temperature, pH 5.0 and metal ion equilibrium concentration of 10 mg/l.

Qi and Xu [85] have evaluated the sorption of Pb(II) onto chitosan nanoparticles (40–100 nm) prepared by ionic gelation of chitosan and tripolyphosphate.

For adsorption of heavy metals and arsenic from aqueous systems, one of the most widely studied nanomaterial is titanium dioxide. Titanium dioxide (TiO₂) is a relatively common material that has been used in many products including paints, plastics, foods, cosmetics, paper, and toothpastes because of its stable, brilliant white color [86]. TiO₂ can have three crystal structures: anatase, rutile, and brookite. Rutile is thermodynamically stable at room temperature while anatase is kinetically stable and will not readily transform to the rutile phase at room temperature. In addition to that the anatase phase of TiO₂ has commonly been used as a photocatalyst to oxidize organic pollutants in water and air [87].

It has been reported that bulk and nanoparticle TiO₂ anatase exhibit different chemical behavior, catalytic reactivity, and surface acidity based on their different surface planes [88]. According to study conducted by the nanoparticles were able to simultaneously remove multiple metals (Zn, Cd, Pb, Ni, Cu) from a solution of pH 8.0. Adsorption kinetics for heavy metals followed a modified first order model, and the nanoparticles had a faster adsorption than the bulk ones. Langmuir isotherm was suitable to characterize metal adsorption onto TiO₂ anatase [89]. In another study conducted by Liang et al. [90], nano-TiO₂ (diameter = 10–50 nm, BET surface area = 208 m²/g) showed adsorptive capacity to Zn and Cd as 15.3 and 7.9 mg/g, respectively, at pH 9.0.

2.3.4. Nanocatalysts and Redox Active Nanocomposites

In photocatalysis, light of energy greater than the band gap of the semiconductor, excites an electron from the valence band to the conduction band (Figure 2.11). In the case of anatase TiO₂, the band gap is 3.2 eV, therefore UV light ($\lambda \leq 387$ nm) is required [87]. As illustrated in Figure 2.11 the absorption of a photon excites an electron to the conduction band (e_{CB}^-) generating a positive hole in the valence band (h_{VB}^+). Charge carriers can be trapped in the TiO₂ lattice or they can recombine, releasing energy. Otherwise, the charge carriers can migrate to the catalyst surface and

initiate redox reactions with adsorbates. Positive holes can oxidize OH^- or water at the surface to produce $\bullet\text{OH}$ radicals, which are extremely powerful oxidants [8].

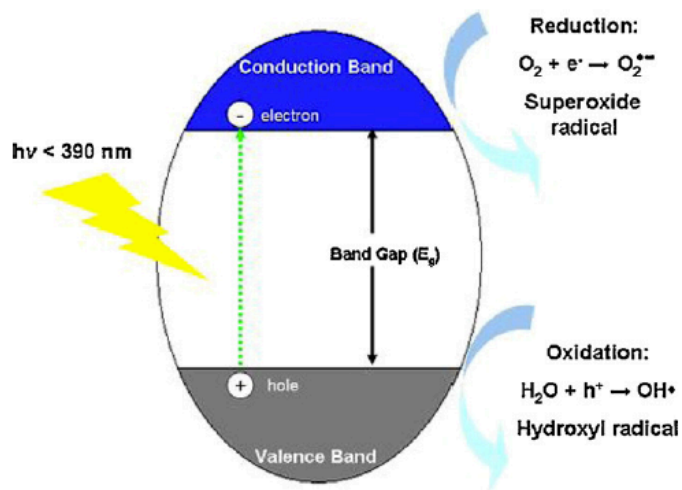
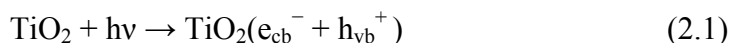


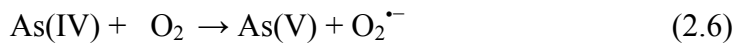
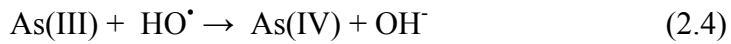
Figure 2.11. Schematic of TiO_2 photocatalytic mechanism [8]

The photooxidation of As(III) to As(V) in the presence of TiO_2 and light and subsequent adsorption into TiO_2 has also been investigated. Bissen et al. [91] have reported that photooxidation of As(III) to As(V) occurs within minutes and that exponential declines in As(III) concentration. No reverse reaction of As(V) to As(III) was observed, and while As(III) was oxidized by UV light in the absence of TiO_2 , the reaction was too slow to be practical in water treatment. Pena et al. [92] reported that rapid photooxidation of As(III) to As(V) occurred in the presence of sunlight, nanocrystalline TiO_2 , and oxygen. In natural groundwater, the oxidation of As(III) to As(V) and subsequent adsorption of As(V) onto TiO_2 would completely remove arsenic at slightly acidic pH values. The photooxidation pathways of the TiO_2 -catalyzed As(III) is given in the following [92].

Generation charge carriers and photooxidants:



Arsenic(III) oxidation:



TiO₂ powder, can by itself, photodegrade pollutant molecules when radiated with UV radiation. However, during the photodegradation process, interaction by certain pollutant molecules or their intermediates could cause the TiO₂ powder to coagulate, thereby reducing the amount of UV radiation from reaching the TiO₂ active centers (due to reduction of its surface area) catalytic effectiveness. In order to overcome this coagulation problem, some researchers have used different materials as a support for the titania photocatalyst. Carbonaceous materials were initially used as a support for TiO₂ in photodegradation studies [93]. It has a very large specific surface area that is typically more than TiO₂.

CHAPTER 3

KINETIC MODELING OF ARSENIC REMOVAL FROM WATER

BY FERRIC ION LOADED RED MUD

3.1. Background

Arsenic is one of the well-known toxic contaminants in the environment. Arsenic contamination in aqueous system is a global problem. The excessively high arsenic concentration, especially in drinking water, is a challenging environmental water pollution problem for many countries as the USA, China, Chile, Bangladesh, Taiwan, Mexico, Argentina, Poland, Canada, Hungary, Japan, India, and Turkey [94]. Arsenic is severely harmful to the human health. Long-term exposure to arsenic can lead to cancer of the lungs, skin, kidney, and liver [95]. Due to its toxic and carcinogenic effects on humans, the contamination level of arsenic in water has been taken under serious consideration by environmental authorities. According to the World Health Organization (WHO), 10 $\mu\text{g/L}$ has been adopted as the maximum contamination level (MCL) of arsenic in drinking water [96]. The technologies for removal of arsenic species from water can be classified as coagulation, electrolysis, ion exchange, membrane processes and adsorption [16, 18, 19, 97]. Nowadays, removal of arsenic by adsorption has acquired importance due to its technical simplicity and applicability in rural areas, where people are more subject to polluted drinking water with arsenic [74]. However, the issue of arsenic contaminated water is not only related to technical obstacles but also associated with economic ones. The costs of arsenic removal technologies are prohibitive. Considering the millions of people threatened by arsenic-

contaminated water, low-cost technologies are urgently needed to effectively remediate arsenic from water, especially in developing nations.

Several researchers have reported the removal of arsenic from aqueous solution by solid adsorbents. The most widely studied low cost solid adsorbents for adsorption processes include untreated rice husks [98], lignite [99], activated carbon [100], fly ash [101], sand [102], clay minerals [103] and natural zeolites [15]. Recent literature has also shown that red mud (RM), which is a cost-effective adsorbent material, significantly reduces arsenic concentration in water [104]. RM is composed generally of iron, aluminum, silica, calcium and titanium oxides particles and obtained as a waste material during the production of alumina [105]. At present, about 1-2 tons of RM residues are produced from a ton of alumina, and the disposal of RM is especially one of the main problems for many alumina industries [106, 107]. Such a residue causes a severe environmental problem because of RM's high alkalinity and depositing large amounts of RM in depony areas [80, 106, 107]. Therefore, proper modification of RM and utilization of it as an adsorbing material for environmentally hazardous pollutants may be beneficial for such an inexpensive material. Genc-Fuhrman et al. [80] investigated the neutralization of RM by acids and ferrous sulfate in order to facilitate the environmental use of the RM. They demonstrated that with acid treatment alone arsenic removal efficiency increased. Li et al. [108] prepared ferrous based red mud as adsorbent for As(V) removal and they discovered that an amount of 0.4 g/L ferrous based red mud was sufficient for remarkable arsenic removal of an initial 0.5 mg/L As(V) concentration.

Recent studies have illustrated the possible use of ferric based sorbents for water containing arsenic species [108, 109] since ferric iron has a high affinity towards inorganic arsenic species and is very selective in the adsorption process [110]. However, the removal of both As(III) and As(V) from water using ferric ion loaded red mud (FRM) has not been reported in the adsorption literature; moreover, the sorption kinetics and adsorption mechanisms of As(III) and As(V) on the adsorbent material has not been reported previously. Therefore, the objectives of this chapter were: (i) to prepare the adsorbent material by mixing a certain ratio of FeCl_3 with RM (ii) to investigate the influence of pH, initial arsenic concentration, and contact time on As(III) and As(V) adsorption (iii) to understand the adsorption mechanisms and rate-

determining steps of As(III) and As(V) onto FRM by analyzing the sorption kinetic models and (iv) to obtain adsorption isotherm parameters for As(III) and As(V).

3.2. Experimental

3.2.1. Materials and Reagents

RM supplied from Etibank Seydisehir Aluminium Plant, Konya, Turkey was washed with distilled water and boiled for 30 min, then dried at 100°C in oven for 32 h and stored in a desiccator for further analysis and experiments. Analytical grade hydrochloric acid, sodium hydroxide and ferric chloride hexahydrate were purchased from Merck. All the solutions were prepared by deionized water using Q-H2O, Millipore Corp. deionizer until 18.2 MΩcm of resistivity. As₂O₃ (99.9 % from Sigma-Aldrich) was dissolved in deionized water for 50 mg/L As(III) stock solution. Na₂HAsO₄.7H₂O salt (99.9 % from Sigma-Aldrich) was dissolved in deionized water for 50 mg/L As(V) stock solution. The working solutions were prepared by diluting these stock solutions with deionized water. All stock solutions were prepared weekly and frozen to prevent oxidation.

3.2.2. Preparation of Ferric Ion Loaded Red Mud (FRM)

10 g of RM was washed with deionized water and dried at about 100°C for 24 h. Then, 6 g of the dried RM was mixed with 100 mL of 0.05 M FeCl₃.6H₂O solution, and the pH of mixture was adjusted to ~4.0 by the addition of 5 M sodium hydroxide (NaOH) solution. The resulting solution was precipitated and dried at 80°C for 2 days. The dried material was washed with deionized water until the washing liquid became free from iron.

3.2.3. Adsorption Experiments

Experiments for the effect of varied pH on adsorption efficiency were carried out by adjusting pH values of 1 mg/L As (III) or As (V) solution from 2.0 to 10.0 with the addition of 1 g/L adsorbent material. The pH of solutions was adjusted to specified values with diluted HCl or NaOH, and the mixtures were shaken in an incubator shaker at 180 rpm mixing rate for 12 h at 25°C. At the end of experiment, the solution was separated from the solid adsorbent by using 0.45 µm PVDF membrane filter. In kinetic experiments, 100 mL of 1 mg/L As(III) or As (V) solution with 1 g/L adsorbent material at pH 2.0 were used and sampled at different time intervals. A series of batch adsorption tests were conducted by using a known amount of adsorbent with 50 mL aqueous solution of As (III) or As (V) of desired initial concentrations of 0.04-20 mg/L at pH 2.0 and 7.0 to develop adsorption isotherms. Each adsorption experiment in the present study was repeated three times and average values were reported below.

3.2.4. Characterization

Leo Supra 35VP field emission scanning electron microscope, Leo 32 and electron dispersive spectrometer software was used for images and analysis. Imaging was generally done at 2-5 keV accelerating voltage, using the secondary electron imaging technique. X-ray diffraction (XRD) measurements of all samples were done with a Bruker axs advance powder diffractometer fitted with a Siemens X-ray gun and equipped with Bruker axs Diffrac PLUS software. The sample was swept from $2\theta = 10^\circ$ through to 70° . The X-ray generator was set to 40kV at 40 mA. Fourier transform infrared spectroscopy (FTIR) of the samples was conducted on an Nicolet iS10 spectrometer ranging from 525 to 4000 cm^{-1}

Arsenic concentrations of the solutions were measured with a Varian, Vista-Pro CCD simultaneous inductively coupled plasma ICP-OES spectrophotometer. Samples before and after adsorption experiments were analyzed to obtain residual arsenic concentration.

3.3. Results and Discussion

3.3.1. Characterization of Adsorbent Materials

The SEM image of FRM indicated visual differences in terms of surface roughness and cavities as compared to RM (Figure 3.1a and 3.1b). Loading red mud with FeCl_3 was the reason for the development of some irregularities on the surface of red mud.

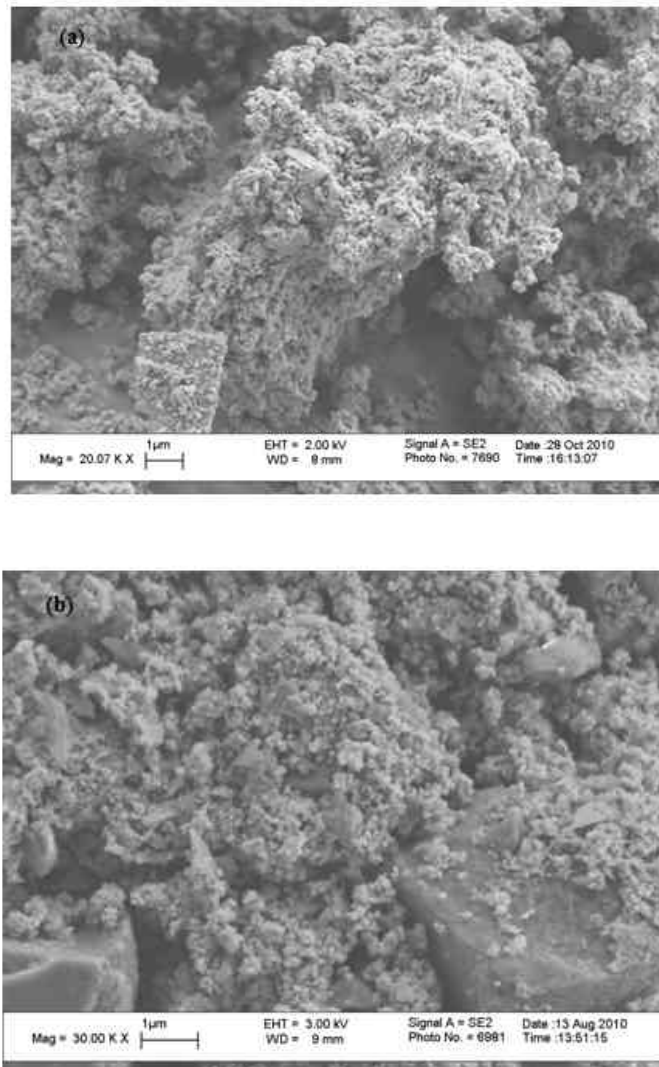


Figure 3.1. (a) SEM micrograph of the particles of the RM and (b) SEM micrograph of the particles of the FRM

The mineralogical compositions of the samples were determined by X-ray diffraction analyses over a range of 10-70° in Figure 3.2.a. The increase in the content of Fe in FRM was also validated by XRD characterization. The characteristic peaks of ferric oxide (α -Fe₂O₃), which gives the brick red color to the adsorbent material, were observed at 24.07°, 33.13°, 35.61°, 40.88°, 49.41°, 53.94°, 62.43° and 64.1° for FRM with an increase in the intensity of those peaks as compared to the XRD graph of RM. However, the other mineralogical constituents of iron as goethite (FeOOH) and iron hydroxide (Fe(OH)₃) were not detected in both adsorbent material. In addition, XRD analysis revealed the existence of compounds including mainly aluminum oxide at 14.14°, and calcite at 29.68°. Those characteristic peaks of aluminum oxide and calcite were reduced in the XRD graph of FRM.

In order to investigate functional groups on the surface of RM and FRM, FTIR measurements were performed. The positions of absorption bands were roughly similar in both adsorbent materials (Figure 3.2.b). Characteristic bands correspond to Si-O vibration were observed at ~978 cm⁻¹ proved the presence of silica groups in the structure of RM and FRM. In addition, the two peaks at ~1642 and ~530 cm⁻¹ indicated the presence of the stretching vibrations of Fe³⁺-O²⁻ bond [111]. Intensities of these peaks were increased in FRM, which confirmed successful ferric ion loading of red mud. Furthermore, the FTIR spectrum of FRM indicated a broad band at ~3396 cm⁻¹ due to the O-H stretching vibrations of adsorbed H₂O during the ferric ion loading process. The absorption bands at ~1421, and ~1455 cm⁻¹ of RM represented the existence of calcite (CaCO₃) and for the case of FRM, this absorption band were not detected as consistent with the results obtained from the XRD analysis.

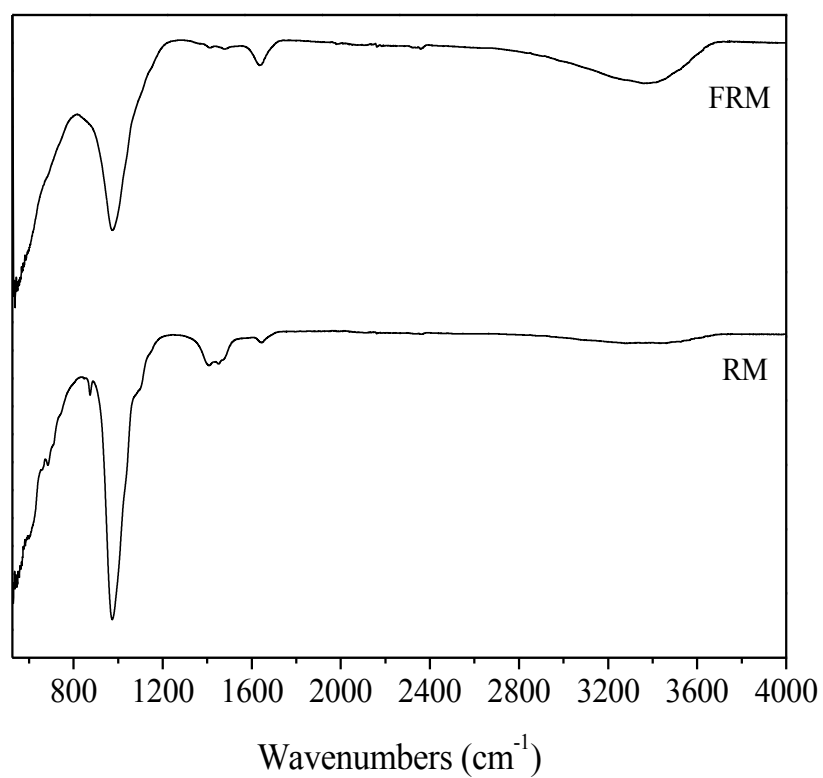
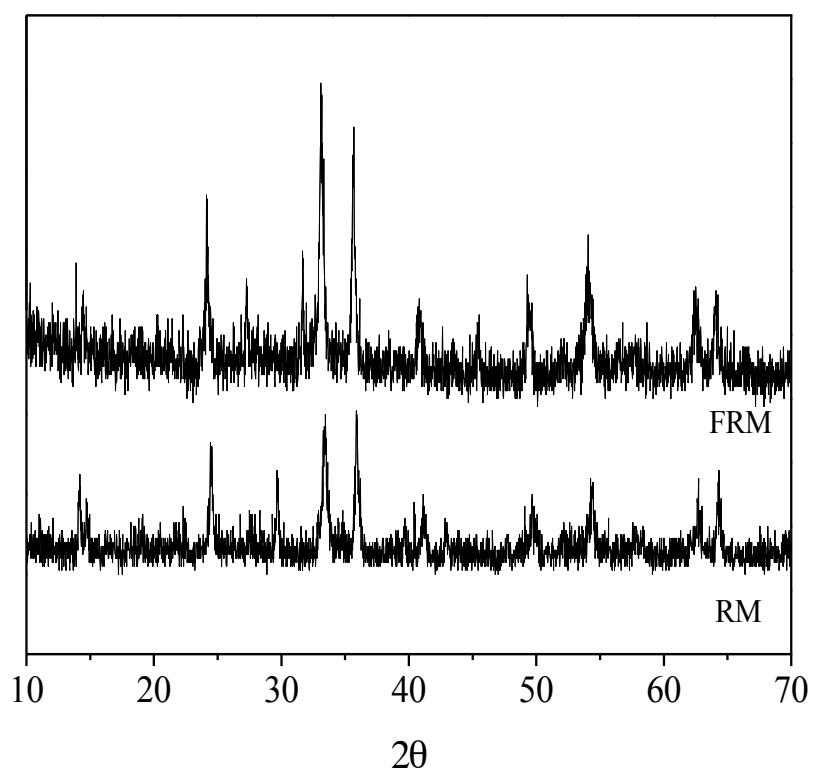


Figure 3.2. (a) X-ray diffractogram of RM and FRM and (b) Infrared spectra of RM and FRM

3.3.2. Effect of pH

The pH of aqueous solution can affect considerably the removal of As(III) and As(V) ions, and the formation of surface charge groups onto adsorbent. The adsorptions of an initial As(III) and As(V) concentration of 1 mg/L onto FRM have been conducted using the initial pH range ($\text{pH}_{\text{initial}}$) of 2.0-10.0. After completion of reaction, equilibrium pH (pH_{final}) values as well as the arsenic uptake, q_e (mg/g) were measured and results were shown in Figure. 3.3. For the adsorption of As(III), the pH_{final} had a plateau, that was found at the $\text{pH}_{\text{initial}}$ range of 6.0-7.0, near to pH 6.0 and then again started to increase with the initial pH. However, for the adsorption of As(V), the pH_{final} increased gradually with the increase of $\text{pH}_{\text{initial}}$. The maximum arsenic uptakes were found 0.57 mg/L for As(III) at pH 7.6 and 0.98 mg/L for As(V) at pH 3.3, respectively.

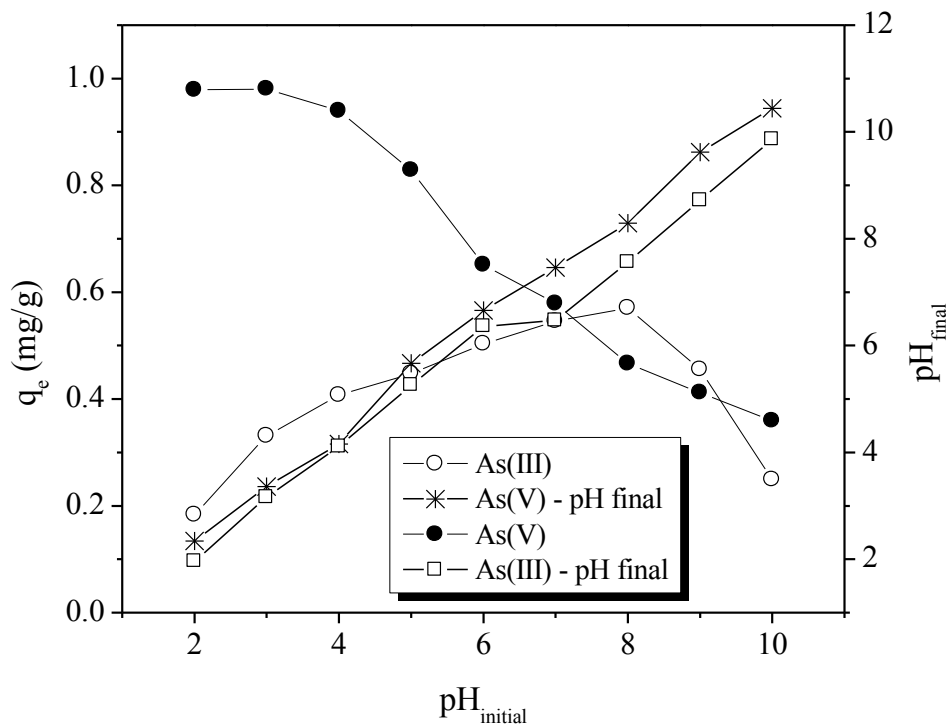


Figure 3.3. The pH_{final} and arsenic uptake, q_e as a function of $\text{pH}_{\text{initial}}$ for adsorptions of As(III) and As(V) onto FRM. (initial arsenic concentration: 1mg/L adsorbent amount: 1 mg/L, temperature: 25°C and contact time: 12 h).

According to Figure 3.3 favorable adsorption took place in the pH range of 2.3-4.2 for As(V) and in the pH 7.6 for As(III). In terms of the ionic character of the arsenic species that varies with pH, the predominant As(III) species are available as H_3AsO_3 and H_2AsO_3^- in the pH range of 4.0-9.5, while the predominant As(V) species show variations with pH values: H_3AsO_4 (pH 0.0-2.0), H_2AsO_4^- (pH 3.0-6.0), and HAsO_4^{2-} (pH 7.0-11.0) [112]. In the study carried out by Zhang et al. [109], the higher As(V) removal percentage was obtained at lower pH values for modified RM and a similar decline in As(V) uptakes through the basic pH values was also observed in our results. This decline could be explained by the decrease in the number of positively charged surface groups onto the FRM when the pH value increased from acidic to a basic condition.

The FRM contained oxides of iron, aluminum, silicon, and calcium which are responsible for the forming of charges on the adsorbent surface. At acidic pH conditions, the surface of adsorbent is covered with positively charged surface groups that boost the adsorption of the negatively charged As(V) anions through the electrostatic attraction [113]. The strong electrostatic attraction between adsorbent and adsorbate along with chemical interaction provides a higher As(V) removal efficiency. Indeed, the As(V) species became more negatively charged at basic pH values (7.0-11.0), but the active sites of adsorbent were negatively charged that reduce their interactions with As(V) anions. The maximum arsenic uptake of FRM was observed at pH 7.6 for As(III). In the removal of As(III) by amorphous ferric hydroxide [114, 115], modified calcined bauxite [116] and granular ferric hydroxide [117], similar results were reported in terms of optimum pH value. The considerable reduction of arsenic uptake was observed for As(III) at pH 9.9 because of the electrostatic repulsion between the surface groups of adsorbent and As(III) species. In other words, with the increase in pH value, H_3AsO_4 species is drastically reduced and anionic As(III) species such as H_3AsO_3^- $\text{H}_3\text{AsO}_3^{2-}$ are dominant at pH 9.0 [104]. In conclusion, the negatively charged nature of adsorbent surface and anionic As(III) species may result in the electrostatic repulsion that attributes the reduction in As(III) removal.

3.3.3. Effect of Initial Arsenic Concentration

Initial arsenic concentration influenced the removal percentage of arsenic species from water. At constant adsorbent amount which was 1 g/L for RM and FRM, different initial As(III) and As(V) concentrations, varied between 0.04-20 mg/L at pH 2.0, were chosen for both adsorbent material. The experimental results (Figure 3.4) indicated that removal percentage of arsenic species decreased with increase in initial arsenic concentration. For an initial arsenic concentration of 0.04 mg/L, FRM was able to remove ~91% of As(III) from water while this percentage decreased to 38 for RM. At an initial concentration lower than 0.12 mg/L, the FRM with a dosage of 1 g/L was able to reduce As(III) below its MCL of 0.01 mg/L. In case of As(V) adsorption onto FRM considerably high arsenic adsorption percentages were observed for initial arsenic concentrations lower than 5 mg/L and the percent removal increased from 95.26% at 5 mg/L to 99.35% at 2 mg/L. In general, at higher arsenic concentrations, most of the active binding sites of adsorbents were covered with arsenic species and further adsorptions were prevented leading to lower arsenic removal percentages for both adsorbents. The sharper decrease in arsenic removal percentage was also observed in the case of RM due to the rapid saturation of active sites with arsenic species. Moreover, the results demonstrated that, RM had nearly no adsorption ability when As(V) concentration was higher than 1 mg/L. Essentially, the FRM which was neutralized with iron chloride to obtain environmentally safe adsorbent material provided better As(III) and As(V) removal performances rather than RM for all of the initial arsenic concentrations. The present results are promising for the use of FRM in drinking water contaminated with low concentrations of arsenic species.

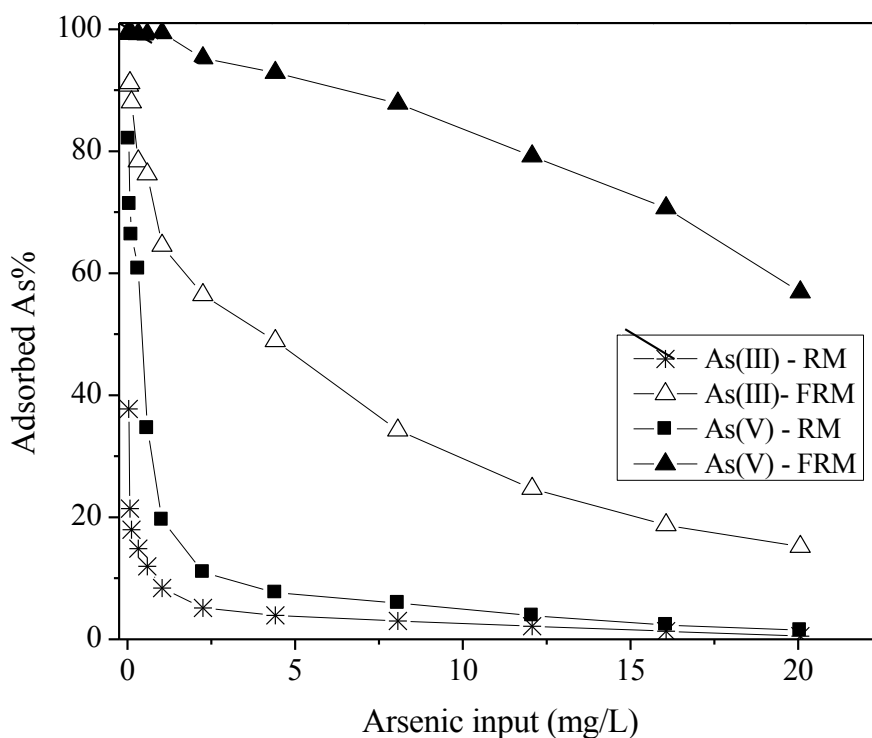


Figure 3.4. Effect of initial arsenic concentration on arsenic removal by FRM and RM. (initial arsenic concentration: 0.04-20 mg/L, adsorbent amount: 1 mg/L, pH: 2.0, temperature: 25°C and contact time: 5 h).

3.3.4. Effect of Contact Time and Sorption Kinetics

The kinetic studies were conducted in order to understand the adsorption behavior of the FRM by taking subsamples at different time intervals. The experiments were performed with 0.1 g of adsorbent material and 100 mL of As(III) and As(V) solutions at a desired concentration (1, 2 and 4 mg/L) for 1, 5, 10, 20, 40, 60, 100, 140, 180, and 260 min reaction times at pH 2.0. The plots of arsenic uptake versus adsorption time t at three initial As(III) and As(V) concentrations were presented in Figure 3.5a and 3.5b. The results revealed that the adsorption of arsenic species was greatly dependent on contact time and the sorption of As(V) ions from water was rapid in contrast with the adsorption of As(III) species. Adsorption due only to the electrostatic forces is quite rapid and can occur in the order of milliseconds [118] to seconds [119]. Adsorptions of As(III) and As(V) in this study were in the order of minutes, indicating a specific adsorption site preference of those arsenic species onto the FRM surface. At all initial

As(III) and As(V) concentrations, the arsenic uptake increased fast in the initial stage of adsorption followed by a slower increase before achieving a plateau.

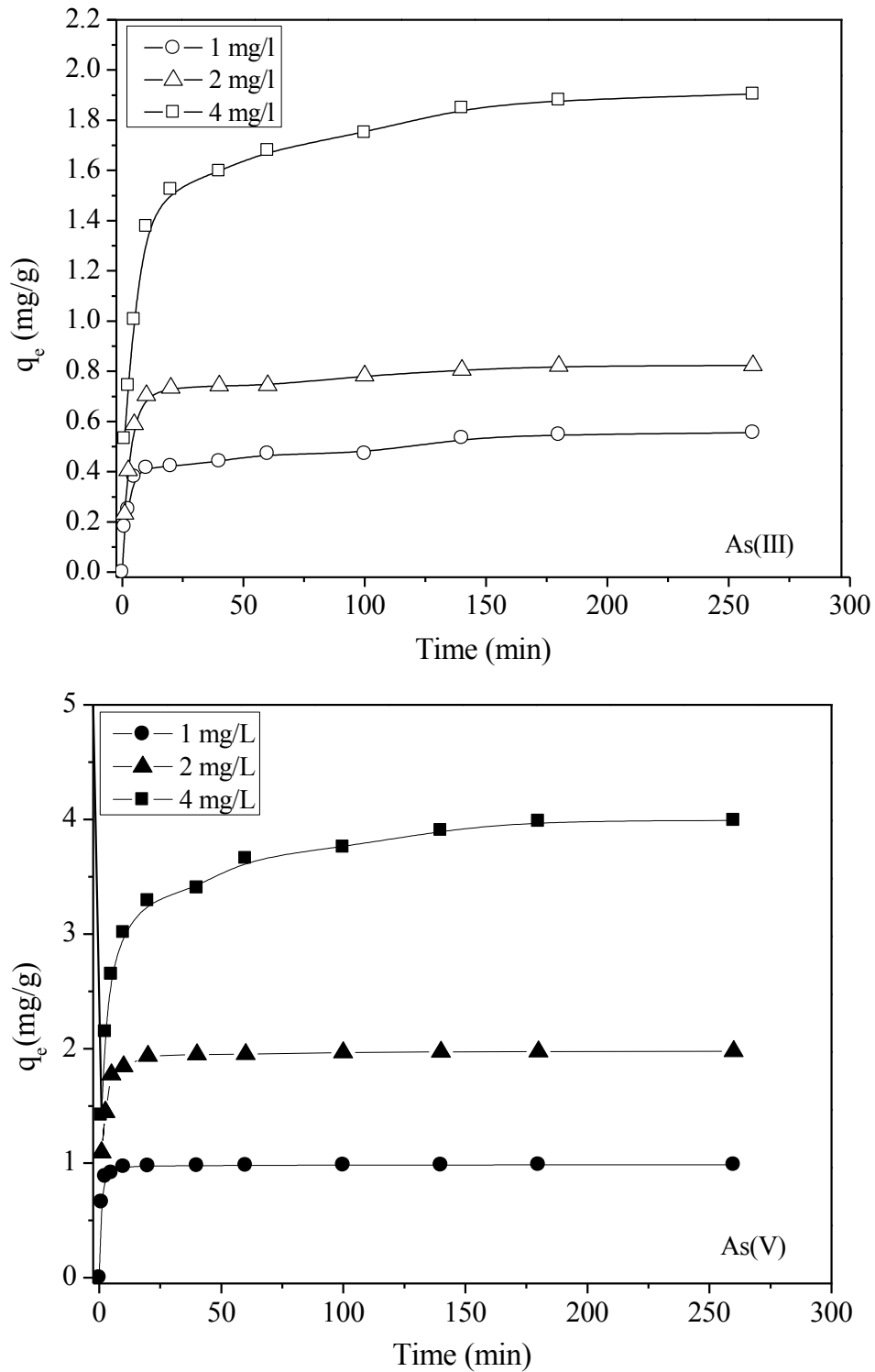


Figure 3.5. Arsenic uptake on FRM versus adsorption time at different initial arsenic concentrations (a) pure As(III) (b) pure As(V). (initial arsenic concentration: 1, 2, and 4 mg/L, adsorbent amount: 1 mg/L, pH: 2.0, temperature: 25°C).

The initial As(V) uptake by FRM was high since a large number of adsorption sites were available for the adsorption by loading red mud with ferric chloride solution. According to Deliyanni [110] and Pedersen's [120] results, As(V) species showed a strong adsorption behavior on the iron and aluminum sites of adsorbent. The adsorption efficiency of As(V) increased onto those sites and this could be one of the explanations of the lower As(III) uptake. Secondly, the removal of As(III) from water was usually poor compared to that of As(V) due to the predominant neutral As(III) compound in terms of charge [121].

For the usage of an adsorbent in sorption processes, the understanding of adsorption kinetics is necessary in order to predict the adsorption rate, the mechanism of adsorption and identifying the rate-determining steps. The kinetic data obtained from this study were first analyzed by employing the pseudo-first order (Equation 3.1) and the pseudo-second-order (Equation 3.2) equations [122, 123];

$$\log(q_e - q_t) = \log(q_e) - \frac{k_1 t}{2.303} \quad (3.1)$$

$$\frac{t}{q_t} = \frac{1}{k_2 q_e^2} + \frac{t}{q_e} \quad (3.2)$$

where, q_t is the amount of arsenic adsorbed (mg/g) at time t , q_e is the maximum adsorption capacity (mg/g) for the pseudo first-order adsorption and pseudo second order adsorption, k_{ad} is the pseudo-first-order rate constant for the arsenic adsorption process (1/min), k_2 is the pseudo second order rate constant (g/mg.min).

The experimental data were fitted with both the linearized pseudo first order and linearized pseudo second order models. The parameters calculated from the pseudo first order and pseudo second order linearized equations were listed in Table 3.1. The adsorption process did not follow the pseudo first order, as observed by the poor fit in all three different As(III) and As(V) initial concentrations. However, the higher regression coefficients (R^2) were obtained after the application of pseudo-second order to the experimental data of As(III) and As(V) initial concentrations (Figure 3.6). The pseudo first-order kinetic model has been used for reversible reaction between liquid

and solid phases [124]. In contrast, the pseudo second-order kinetic model may consider chemical adsorption as the rate-determining step [125].

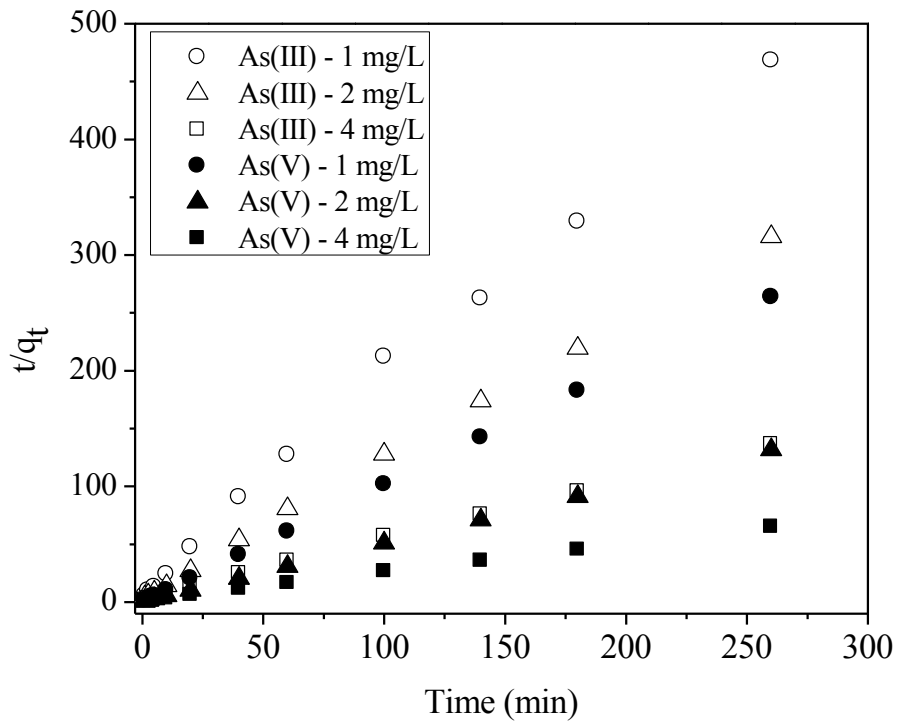


Figure 3.6. Linearized pseudo-second-order reaction kinetics of As(III) and As(V) on FRM. (initial arsenic concentration: 1, 2, and 4 mg/L, adsorbent amount: 1 mg/L, pH: 2.0, temperature: 25°C)

Table 3.1. Parameters of pseudo first order and pseudo second order kinetic models for adsorption of As(III) and As(V) on FRM at pH 2.0.

C_o	As(III)			As(V)		
	1 mg/L	2 mg/L	4 mg/L	1 mg/L	2 mg/L	4 mg/L
q_{e-exp} (mg/g)	0.555	0.823	1.903	0.986	1.975	3.921
<u>Pseudo first order</u>						
q_e (mg/g)	0.371	0.547	1.070	0.457	0.963	2.750
k_{ad} (min^{-1})	0.032	0.029	0.009	0.074	0.043	0.046
R^2	80.97	92.54	84.66	67.82	66.69	85.53
<u>Pseudo second order</u>						
q_2 (mg/g)	0.559	0.829	1.928	0.987	1.977	4.043
k_2 (g/mg min)	3.590	0.352	0.092	3.036	1.448	16.82
R^2	99.62	99.96	99.92	99.99	99.99	99.94

The physical and chemical adsorption processes contain namely diffusion to bulk solution, external diffusion, internal intraparticle diffusion, and adsorption [126, 127]. In fact, the controlling steps occur at which the adsorbate transports through the exterior surface of the adsorbent (external diffusion), and at which the adsorbate diffuses into the adsorbent surface of internal pores (intraparticle diffusion) [126]. In order to understand the adsorption mechanism and to obtain the process of rate-determining steps, external diffusion and intraparticle diffusion models were investigated.

The external diffusion model [128] was considered to analyze the experimental results by employing the following equation.

$$\ln \frac{C_t}{C_0} = -k_{ext}t \quad (3.3)$$

where k_{ext} is the external diffusion rate constant (1/min) and C_t is the equilibrium solution concentration (mg/L) and C_o is the initial solution concentration (mg/L). A linear plots of $\ln C_t$ versus time t indicated in Figure 3.7a and 3.7b for the adsorptions of As(III) and As(V) onto FRM.

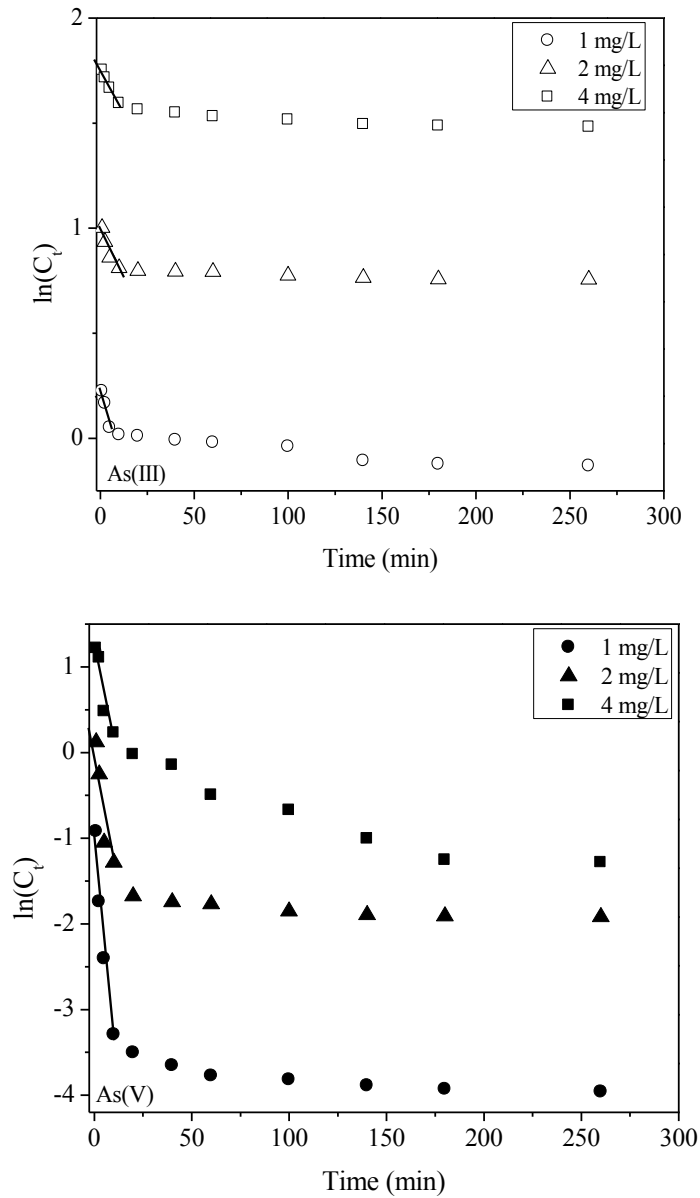


Figure 3.7. Analysis of adsorption process using external diffusion model (a) pure As(III) (b) pure As(V). (initial arsenic concentration: 1, 2, and 4 mg/L, adsorbent amount: 1 mg/L, pH: 2.0, temperature: 25°C).

For the rate of intraparticle diffusion process, the equation 3.4, which was proposed, by Weber and Morris [127] was used ;

$$q_t = A + k_{int}^{0.5} t^{0.5} \quad (3.4)$$

where k_{int} ($\text{mg}/(\text{g min}^{0.5})$) is the internal diffusion rate constant and A is the intercept of the linear plot of q_t versus $t^{0.5}$ (Figure 3.8a and 3.8b). The modeling results of our kinetic data were shown in Table 3.2.

From the short straight trend lines in Figure 3.7a and 3.7b, external film diffusion model was the rate-determining mechanism only at the initial stage of As(III) and As(V) adsorptions. The plots obtained from the intraparticle diffusion model indicated the presence of three linear sections of experimental data for three different initial As(III) and As(V) concentrations. At the first linear stage, fast adsorptions of arsenic species were observed due to the external surface adsorption. However, in the second linear stage, slower adsorptions of As(III) and As(V) onto FRM indicated the intraparticle diffusion process which was rate determining mechanism for both arsenic species. The third stage was the final equilibrium stage where the intraparticle diffusion rates of As(III) and As(V) were reduced and the processes reached the plateau.

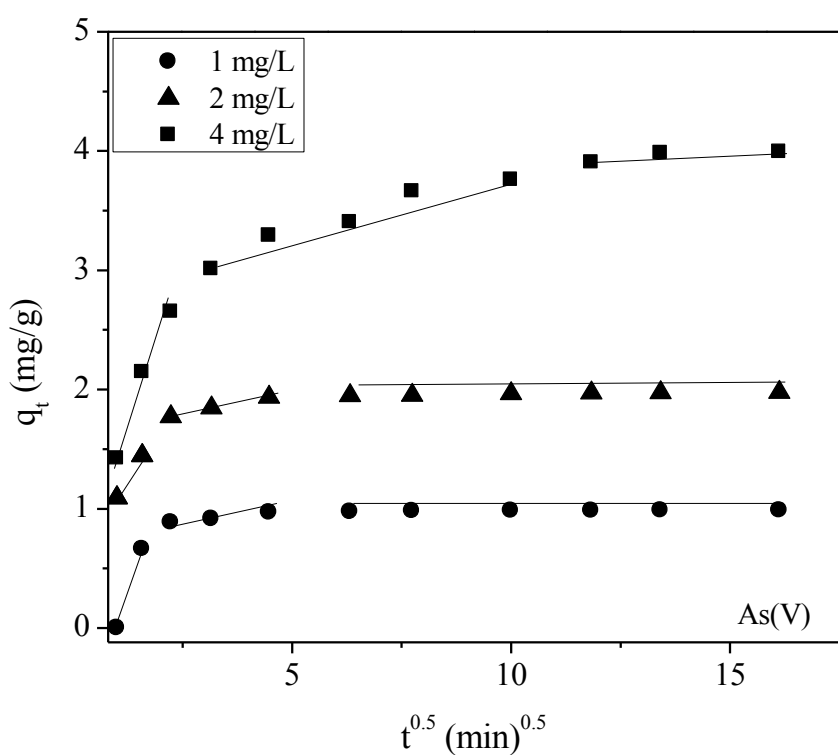
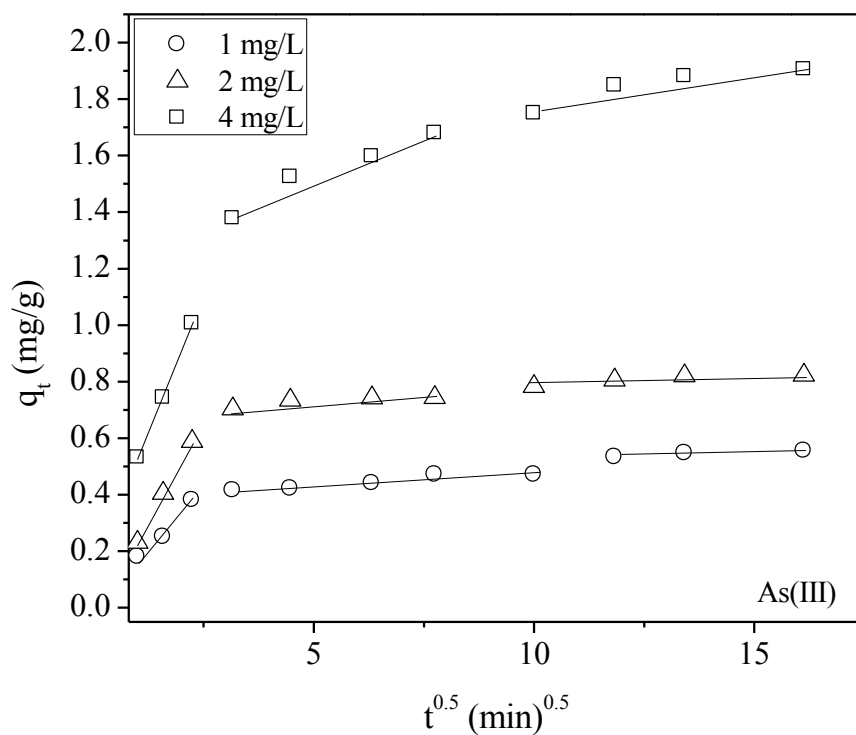


Figure 3.8. Analysis of adsorption process of arsenic onto FRM using intraparticle diffusion model (a) pure As(III) (b) pure As(V). (initial arsenic concentration: 1, 2, and 4 mg/L, adsorbent amount: 1 mg/L, pH: 2.0, temperature: 25°C).

Table 3.2. Parameters of external diffusion and intraparticle diffusion models for adsorption of As(III) and As(V) on FRM at pH 2.0.

C_o	As(III)			As(V)		
	1 mg/L	2 mg/L	4 mg/L	1 mg/L	2 mg/L	4 mg/L
<u>External diffusion model</u>						
k_{ext} (min^{-1})	0.048	0.034	0.017	0.247	0.154	0.115
R^2	99.22	98.88	98.71	94.35	84.61	89.09
<u>Intraparticle diffusion model</u>						
$k_{1\ int}$ ($\text{mg}/(\text{g min}^{1/2})$)	0.178	0.289	0.3853	0.223	0.607	0.989
R_1^2	96.97	99.96	99.93	99.99	99.99	98.15
$k_{2\ int}$ ($\text{mg}/(\text{g min}^{1/2})$)	0.008	0.009	0.062	0.025	0.072	0.107
R_2^2	96.05	76.33	95.27	75.73	99.81	94.17
$k_{3\ int}$ ($\text{mg}/(\text{g min}^{1/2})$)	0.005	0.007	0.023	0.001	0.003	0.018
R_3^2	91.04	81.42	82.94	89.70	88.66	69.50

3.3.5. Adsorption Capacity

The adsorption of arsenic, initially ranging from 0.04 to 20 mg/L concentration onto FRM has been performed at pH 2.0 and pH 7.0 using 1 g/L adsorbent material in the batch mode. A time of 300 min. was used to reach equilibrium in the experiments to construct the adsorption isotherms. The relationship between the adsorption capability, (q_e) and equilibrium concentration, (C_e) of arsenic onto FRM was shown in Figure 3.9, indicating better As(V) removal capabilities of FRM compared to As(III) for the two

different pH values. It was apparent that the extent of As(V) adsorption at pH 2.0 was higher than that at pH 7.0 over the entire range of equilibrium concentration values. However, the adsorption of As(III) onto FRM at pH 7.0 exhibited the comparable increase with respect to the adsorption at pH 2.0. Since the surface of FRM was covered with positively charged surface groups at acidic pH conditions and the strong electrostatic attraction between negatively charged As(V) anions and positively charged surface groups provided a higher As(V) removal efficiency. In the case of As(III), the maximum uptake of FRM was observed at pH 7.0, since the predominant As(III) species were available as H_3AsO_3 and $H_3AsO_3^-$ in the pH range of 4.0-9.5.

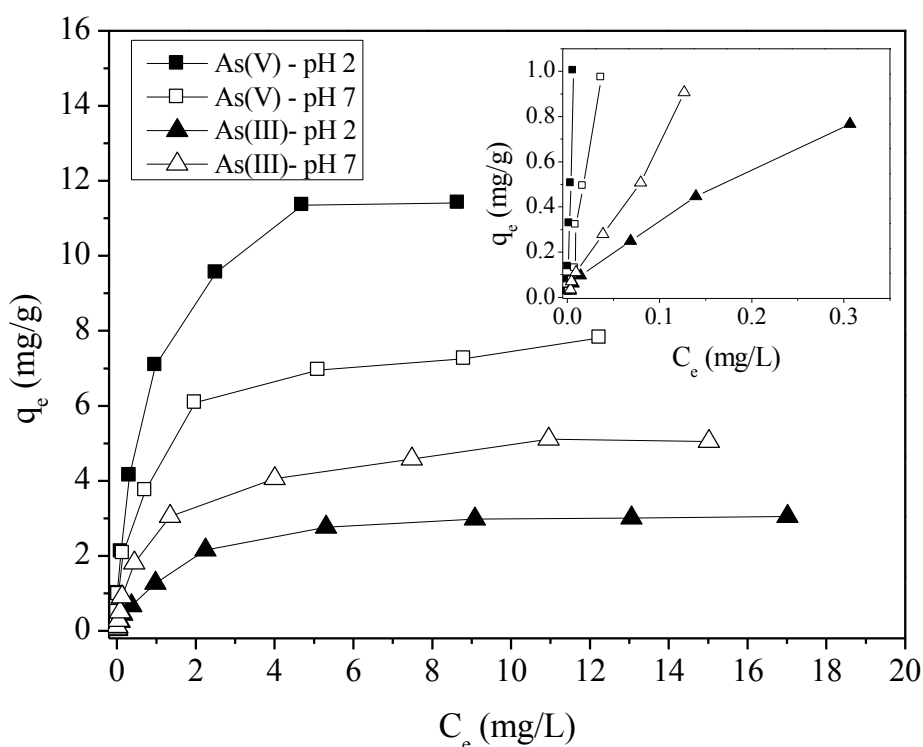


Figure 3.9. Adsorption isotherm of As(III) and As(V) on the FRM (initial arsenic concentration: 0.04-20 mg/L, adsorbent amount: 1 mg/L, pH: 2.0 and 7.0, temperature: 25°C and contact time: 5 h).

The theoretical adsorption capacity of an adsorbent can be obtained through the adsorption isotherm [129]. In this study, the Langmuir and Freundlich isotherm models were investigated to evaluate adsorption patterns of arsenic on FRM with respect to its

concentration of equilibrium in solutions. The Langmuir model assumes monolayer adsorption onto homogenous surface with a fixed number of energetically identical sites [130], while the Freundlich model is derived from the multilayer adsorption and the adsorption occurs first the most energetically favorable sites [131]. The linearized forms of the Langmuir, (Equation 3.5) and Freundlich, (Equation 3.6), isotherms are;

$$\frac{C_e}{q_e} = \frac{1}{q_{mon}b} + \frac{C_e}{q_{mon}} \quad (3.5)$$

$$\ln q_e = \ln K_F + \frac{1}{n} \ln C_e \quad (3.6)$$

where q_e is the amount adsorbed on solid (mg/g), C_e is the equilibrium solution concentration (mg/L), q_{mon} is adsorption capacity (mg/g), b is a constant related to enthalpy of sorption which should vary with temperature (L/mg), K_f , (mg/g) is related to the adsorption capacity of the adsorbent and $1/n$ is a constant known as the heterogeneity factor is related to surface heterogeneity [132, 133]. Table 3.3 summarized the results of the adsorption parameters. According to the regression coefficient values for As(III) and As(V) adsorption onto FRM for the two different pH values, the Langmuir model described the isotherm better than the Freundlich model. The maximum adsorption capacity of FRM at pH 2.0 was about 1.5 times higher than that at pH 7.0 for As(V), whereas the greatest adsorption capacity of FRM was found at pH 7.0 for As(III). The adsorbed arsenic species onto FRM at equilibrium were relatively 5 times lower than those reported by Zhang et al. [109] and Li et al. [108], however such a difference in the results of adsorption capacity was not related to the FRM investigated in this study was a poor adsorbent. Indeed, those studies dealt with much higher initial arsenic concentration at least 5 times higher than ours.

Table 3.3. Calculated isotherm parameters for As(III) and As(V) adsorption onto FRM at pH 2.0 and 7.0

Isotherm models		Isotherm parameters		
<u>Langmuir</u>	q_{max} (mg/g)	b (L/mg)	$-\Delta G^0$ (kJ/mol)	R^2
As(III) – pH 2.0	3.192	1.226	0.504	99.60
As(V) – pH 2.0	11.640	4.014	3.444	99.26
As(III) – pH 7.0	5.254	1.432	0.889	99.70
As(V) – pH 7.0	7.917	2.004	1.722	99.69
<u>Freundlich</u>	K_f (mg/g)	n	$-\Delta G$ (kJ/mol)	R^2
As(III) – pH 2.0	0.997	1.883	17.101	97.83
As(V) – pH 2.0	6.145	1.889	21.653	96.08
As(III) – pH 7.0	1.729	1.736	18.473	95.52
As(V) – pH 7.0	3.126	1.661	19.931	90.13
<u>DKR</u>	β (mol ² /kJ ²)		$-E$ (kJ/mol)	R^2
As(III) – pH 2.0	0.0035		11.952	99.31
As(V) – pH 2.0	0.0028		13.363	99.18
As(III) – pH 7.0	0.0030		12.910	98.24
As(V) – pH 7.0	0.0039		11.322	93.97

The other significant parameter of the Langmuir isotherm, L , is the equilibrium constant relating the rates of adsorption and desorption. For As(V) adsorption onto FRM the L value was higher than the corresponding value for As(III). In fact, the higher L values, in adsorption As(V) onto FRM could be explained by the higher rates of adsorption rather than desorption, which suggested more material adsorbed on the surface of adsorbent. Also from the equilibrium constant of Langmuir isotherm, the dimensionless constant separation factor (R_L), which was the indicative of the isotherm shape, could be obtained by using the following equation:

$$R_L = \frac{1}{1 + bC_o} \quad (3.7)$$

where, C_o is the initial As(III) concentration (mg/L). The value of R_L demonstrates the nature of adsorption as unfavorable ($R_L > 1$), linear ($R_L = 1$), favorable ($0 < R_L < 1$) and irreversible ($R_L = 0$). The calculated values of R_L were found to be 0.9532 to 0.0391 for As(III) and 0.8616 to 0.0123 for As(V) at pH 2.0, indicating highly favorable adsorption of As(V) onto FRM.

Standard Gibbs free energy (ΔG^0 , kJ/mol) for the adsorption process was calculated using the following equation:

$$\ln \frac{1}{b} = \frac{\Delta G^0}{RT} \quad (3.8)$$

where R is the ideal gas constant (0.00831447 kJ/K.mol), and T is the temperature (K). In this study, the negative ΔG^0 values obtained for As(III) and As(V) adsorption on FRM by confirming the feasibility of the adsorption processes and the spontaneous nature of adsorptions.

From the linearized equation of Freundlich model, the calculated K_f values were 1.729 mg/g for As(III) at pH 2.0 and 6.145 mg/g for As(V) at pH 2.0, while the n values for As(III) and As(V) were 1.736 and 1.889, respectively. In fact, the numerical value of n which is between 1 and 10 indicates beneficial adsorptions [134]. By knowing the K_f value, the free energy change of arsenic adsorption onto FRM can be calculated using the equation:

$$\Delta G = -RT \ln(K_f \times 1000) \quad (3.9)$$

Similarly, in the adsorption of As(V) on FRM, free energy change was more negative (Table 3) as compared to As(III) adsorption for the two different pH values of 2.0 and 7.0. Dubinin-Kaganer-Radushkevich (DKR) isotherm model was investigated to determine the physical and chemical adsorption [135] of As(III) and As(V). DKR isotherm equation [136] is:

$$\ln q_e = \ln X_m - k\varepsilon^2 \quad (3.10)$$

where ε is Polanyi potential, equal to $RT \ln (1+1/C_e)$, X_m is the adsorption capacity (mol/g), k is a constant related to adsorption energy (mol²/kJ²). X_m and k values were obtained by plotting $\ln q_e$ versus ε^2 at 25 °C. The slope of line yields k (mol²/kJ²) and the intercept is equal to $\ln X_m$.

In order to evaluate the interaction between arsenic and binding sites of FRM, the mean free energy of adsorption ((E)-the free energy change one mol adsorbate in transferred from infinity in solution to the surface of the adsorbent) was calculated from the following relationship [133].

$$E = -(2k)^{-0.5} \quad (3.11)$$

The calculated E values for As(III) and As(V) were respectively -12.910 kJ/mol for pH 7.0 and -13.363 kJ/mol for pH 2.0. Since E values found in the present study were less than 8 kJ/mol, the physical adsorption due to weak van der Waals forces [137, 138] was also occurring in addition to the chemisorption that was observed by the Type I isotherms which assumes the continuous increase in the amount of adsorbed component with concentration until a plateau is reached where surface of the adsorbent is practically saturated.

Table 3.4 interprets a comparative evaluation of the tested adsorbent material in this study with some commercially available and synthesized adsorbents. The evaluation has been made in terms of maximum arsenic adsorption capacities from isotherm model used. The most important observation is that FRM exhibits higher adsorption capacities obtained from Langmuir isotherm model than most of the adsorbent materials reported earlier.

Table 3.4. Comparison of adsorption performance of tested adsorbent with previous works

Adsorbent	Adsorption isotherm model	As ₀ (mg/L)	Capacity (mg/g)		Ref.
			As(III)	As(V)	
Beydellite-Fe	Langmuir	5	0.789	0.794	[139]
Modified light expanded clay aggregate (LECA)	Langmuir	0.1-0.3	0.035	0.058	[140]
Fe-exchange zeolite (Fe-eZ)	Freundlich	0.1-20	0.100	0.050	[141]
Copper oxide incorporated mesoporous alumina (COIMA)	Langmuir	1	2.161	2.017	[142]
Commercial Titanium dioxide (Degussa P25)	Langmuir	37.5	3.450	4.650	[143]
Red mud	Langmuir	2.5-30	0.884	0.941	[104]
Feric ion loaded red mud (FRM)	Langmuir	0.4-20	5.254	11.640	This work
Iron-containing ordered mesoporous carbon (FeOMC)	Langmuir	1-24	8.156	6.465	[144]
Activated Alumina	Langmuir	20-100	0.180	11.02	[145]

3.4. Concluding Remarks

FRM is very effective adsorbent that reduce both As(III) and As(V) concentrations below the MCL requirements for drinking water. In the current study, evaluation of the arsenic removal efficiency of FRM was performed considering effect of pH, initial arsenic concentration, and contact time. It is important to note that using of 1 g/L FRM dosage for an initial arsenic concentration of 1 mg/L, the maximum arsenic uptakes were found 0.57 mg/g for As(III) at pH 7.6 and 0.98 mg/g for As(V) at pH 3.3, respectively. Moreover, according to kinetic sorption experiments, the higher regression coefficients (R^2) were obtained after the application of pseudo-second order to the experimental data of As(III) and As(V) initial concentrations. In terms of adsorption mechanisms of As(III) and As(V) onto FRM, external diffusion mechanism governed the initial stage of adsorptions and while the intraparticle diffusion mechanism was rate-determining step for the later stages of adsorption. The most important observation was that the higher adsorption capacities achieved from Langmuir isotherm model was found for As(V) at pH 2.0 as compared to As(III) at pH 7.0 and the calculated maximum adsorption capacity values were 11.640 mg/g for As(V) pH 7.0 and 5.254 mg/g for As(III). Essentially, present results are promising for the usage of FRM in drinking water contaminated with low concentration of arsenic species.

CHAPTER 4

As(V) REMOVAL FROM WATER BY IRON OXIDE/ACTIVATED CARBON SYSTEM MANUFACTURED BY MICROWAVE HEATING

4.1. Background

The most efficient ways to remediate waters are probably adsorption and catalytic oxidation of the pollutants. Surely, for such a process to be economical, the catalyst and the adsorbent should have a high catalytic activity and adsorption capacity, and be inexpensive. Many high surface area materials, especially metal oxides, are studied for their special catalytic properties [87, 146, 147] One of these metal oxides is iron oxide, which is studied and used in areas like catalysis [148-151] and environmental applications [152-157]. It is known that synthesizing iron oxides in nano dimensions enhances their catalytic and adsorption properties [158, 159]. These materials are perfect adsorbents for their high specific surface areas. The high surface area-to-mass ratio of nanomaterials can show high adsorption capacities [159].

Iron oxide nanoparticles can be synthesized with various methods like oxidation, hydrolysis of metal alkoxide, micro emulsion, pyrolysis, ultrasonic-assisted methods and decomposition of a metal complex [159-164]. Other than these methods, it has been reported that iron oxide and other metal oxide nanoparticles can be formed by hydrothermal techniques [165-167]. At the supercritical region, with fast reaction rates, metal oxide nanoparticles can be synthesized at an extremely high nucleation rate [165].

The advantage of hydrothermal treatment is, while fine particles are formed in water, these particles can be easily impregnated deep in to the porous support by the help of water. Oshima et al. [166] showed that some metal and metal oxide nano particles can be crystallized onto the alumina support surface, and could reach into the deeper part of the support with an increase of reaction time. On the other hand, Teja et al. [168, 169], used supercritical water to synthesize and disperse iron oxide nanoparticles in activated carbon (AC) pores. They managed to deposit iron oxide particles deep in to hydrophobic pores of AC.

Microwave hydrothermal (MH) synthesis is a new technique for the production of materials like metal oxides, zeolites, and other nanoporous materials [170-173]. Komarneni et al. [170] was the first group using this technique and they synthesized TiO_2 , ZrO_2 , KNbO_3 , BaTiO_3 successfully. According to Tompsett et al. [174], when MH is utilized, the synthesis duration is reduced by over an order of magnitude. In addition, the synthesized material has a more uniform dimension and composition. Date et. al [172] was able to synthesize $\alpha\text{-Fe}_2\text{O}_3$ and Fe_3O_4 particles from FeSO_4 solution by changing the pH of the solution during MH synthesis. On the other hand, studies of iron oxide nanoparticle deposition on a support are quite few. Garcia-Martinez et al. [175] deposited FeO and Fe_2O_3 nanoparticles on MCM-41 support with microwave radiation and studied its catalytic performance on selective oxidation of benzyl alcohol to benzaldehyde and alkylation of toluene with benzyl chloride. Additionally, Suggs et al. [176] prepared carbon/iron oxide nanocomposites starting with sugar and 1,1'-dilithioferrocene. However, to our knowledge there are not any studies about microwave deposition on AC and its adsorption behavior.

In the present chapter, we utilized microwave hydrothermal techniques, to synthesize iron oxide nano particles on AC and ACO support. The effects of parameters like oxidation, heating time and pH on As(V) removal using this material in water cleaning were studied.

4.2. Experimental

4.2.1. Materials

Charcoal activated (powder extra pure food grade) was used as a support material and supplied from Merck Millipore. To obtain oxidized activated carbon (ACO), some portion of the charcoal activated was treated with KMnO_4 (Ak Kimya). The iron precursor was ferric chloride ($\text{FeCl}_3 \cdot 6\text{H}_2\text{O}$) and was purchased from Merck Millipore. As(V) solutions were prepared with $\text{Na}_2\text{HAsO}_4 \cdot 7\text{H}_2\text{O}$ salt (Sigma-Aldrich). Additionally pH values of the solutions were controlled with HCl (Merck Millipore) and NaOH (Merck Millipore) solutions. All chemicals were used as received and all solutions were prepared with de-ionized (DI) water. MH synthesis were performed in a Teflon autoclave using microwave radiation (Delonghi EMD MW 311 adjustable power <800 W, 230 V, 50 Hz).

4.2.2. Deposition of iron oxide nanoparticles on AC

The deposition method was a microwave-modified version of Shemer et al.'s iron oxide deposition on AC. Before starting the deposition of iron oxide nano particles, AC was washed thoroughly and dried overnight at 100 °C. For the iron oxide deposition, AC was used without any additional treatment. However, for the deposition on ACO, AC was treated with KMnO_4 . In this oxidation step, 7.5 g of dried AC was mixed with 0.5 M KMnO_4 solution for 30 min at 150 rpm and 25 °C in a glass Erlenmeyer flask. The mixing was followed by repeated rinsing of the ACO with DI water until no purple color was observed.

After drying, 1 g of AC or ACO were mixed with 5 mL of $\text{FeCl}_3 \cdot 6\text{H}_2\text{O}$ solution at 25 °C (20 g/L (0.36 M) of total iron) and put into Teflon autoclave. Then, the samples were treated for 3, 6 or 9 minutes under microwave radiation of 280 W. Following the treatment, the samples were washed with DI water to remove residual iron. After the

washing step, iron loaded AC (AC-x) and ACO (ACO-x) were dried overnight at 100 °C, where x is 3, 6, or 9 representing the MH treatment duration.

4.2.3. Sample characterization

The deposited amount iron oxide and the ash content of AC and ACO were determined by burning a known mass of the material. For this purpose, NETZSCH 449C thermogravimetric analyzer (TGA-DTA) was utilized. Samples were heated from room temperature to 1000 °C at 10 °C/min in a pure alumina crucible and the residue left after burning away all the carbon were weighed.

For the XRD characterization, a Bruker AXS-D8 advanced powder diffractometer fitted with a Siemens X-ray gun and equipped with Bruker AXS DIFFRAC Plus software was used at room temperature. Measurements were performed in the 2θ range of 5°–90°, at 40 kV and 40 mA, using Cu-K α 1.5406 Å radiation. The step size was always 0.01° and data collection was in 1-s steps.

The surface areas and pore size distribution of the supports and loaded supports were determined using a NOVA 2200e Surface Area and Pore Size Analyzer (Quantachrome Instruments Co., USA). The analyses were performed in boiling liquid nitrogen (77 K). Samples were outgassed at 150 °C overnight. BET surface areas were calculated by the multipoint method using adsorption data in the relative pressure (P/P_0) with a range of 0.05–0.3. The pore volume and pore size distributions were estimated from the desorption branch of the isotherms by the Barrett-Joyner-Halenda (BJH) method. Also standard DR model were applied to derive micropore structural information.

A Leo G34-Supra 35VP field emission scanning electron microscope (SEM) coupled to energy dispersive spectrometer software was used for morphological analysis. Iron loaded samples were first coated with carbon by an Emitech T950 Turbo Evaporator to provide a conducting surface layer. The gun chamber pressure was $\sim 10^{-11}$ mbar. The SEM electron column was equipped with a secondary electron detector, a back-scattering electron detector, and an in-lens detector for secondary electron detection.

Imaging was done at the extractor voltage of 5.2 keV and accelerating voltages ranging between 2 and 5 keV using the secondary electron detector.

4.2.4. Batch adsorption experiments

Arsenic stock solutions with various concentrations were prepared by dissolving As(V) $\text{Na}_2\text{HAsO}_4 \cdot 7\text{H}_2\text{O}$ salt in DI water. Batch adsorption experiments were carried out in 100 mL flasks with 30 mL As(V) solutions with appropriate concentrations. To reach a 0.75 loading (g adsorbent / 1 L solution), 0.0225 g of adsorbent were added to solutions. Afterwards, the bottles were shaken in a controlled incubator shaker at 150-rpm and 25 °C for 24 h. The kinetic experiment were carried out at different time intervals (5 min to 48 h) in an initial As(V) concentration of 5 mg/L at pH 7.0. Several initial concentrations ranging from 0.5 to 20 mg/L aqueous solutions were used for equilibrium studies at fixed pH 7.0 for 24 h. The effect of pH on the adsorptions were studied by using 5 mg/L of As(V) solution in a pH range of 3.0–8.0 at 25 °C. At the end of each experiment, the solution was separated from the solid adsorbent by using 0.45 μm PVDF membrane filter. As(V) concentrations of the solutions were measured with a Varian, Vista-Pro CCD simultaneous inductively coupled plasma ICPOES spectrophotometer. Samples before and after adsorption experiments were analyzed to obtain residual adsorbate ion concentrations. In order to test the reproducibility, the experiments were carried in triplicate and average results were reported.

4.3. Results and Discussion

4.3.1. XRD characterization of the Samples

Figure 4.1 shows XRD patterns of iron deposited AC samples with different heating times. Initially before iron deposition, XRD pattern of the AC confirmed that there was not any detectable crystalline phase. However, after 3 minutes, particles started to deposit on the support with the structure of $\beta\text{-FeOOH}$. On the other hand, further

microwave heating for 3 minutes transformed them to α - Fe_2O_3 . Finally, after a total 9 minutes of heating the structure was still α - Fe_2O_3 . Since essentially the peak heights of the main XRD peaks of α - Fe_2O_3 were the same height, it could be suggested that after α - Fe_2O_3 was formed, extra heating did not have any effect on the crystal structure. Forced hydrolysis of FeCl_3 solutions has been used to synthesize β - FeOOH [177].

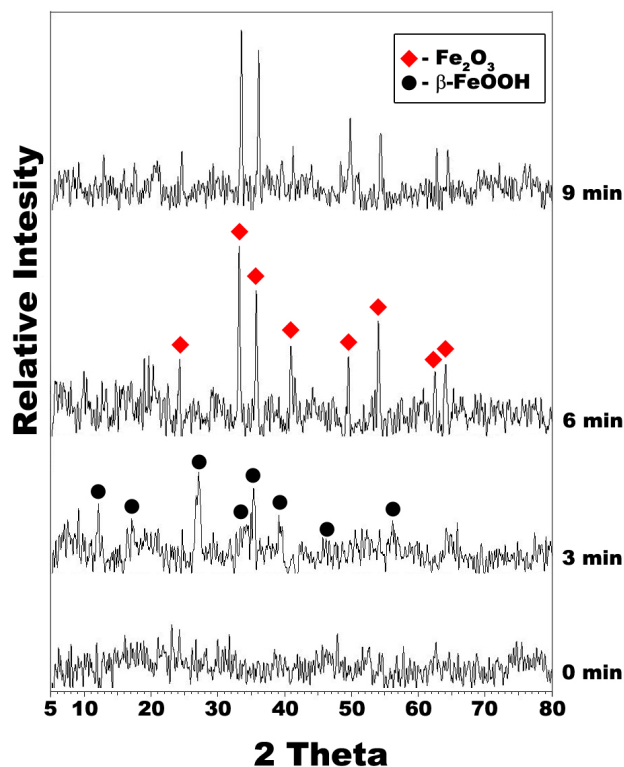
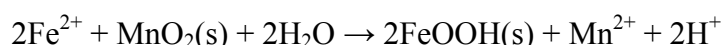
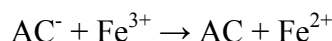


Figure 4.1. XRD patterns of iron deposited AC

4.3.2. SEM Characterization of the Particles

Representative SEM images of iron deposited AC and ACO are shown in Figure 2. Treatment with KMnO_4 created rough surfaces. The roughness was most probably caused by the surface restructuring in oxidative medium. After 3 minutes of heating under microwave radiation, homogeneously distributed particles began to appear on both AC and ACO surfaces. XRD results (Figure 4.1) indicated that these particles were β -

FeOOH. While for AC (3 min.) the particles size was around 60 nm, the particle size on ACO (3 min.) was about 55 nm. When the surfaces were examined, it was observed that the surface of ACO was completely covered with β -FeOOH particles. However, the AC surface was not that crowded with particles. This complete coverage can be explained by the mechanism suggested by Shemer et al. [178]. The mechanism is as follows:



Therefore, initially Fe^{2+} ions reacted with residual MnO_2 particles on the ACO surface and adsorbed as β -FeOOH. On the other hand, for AC, β -FeOOH particles formed not on the surface but in the liquid medium, which caused a less covered AC surface. At the end of 9 minutes of heating, it could be seen that ACO surface was completely covered with a thick layer. On the contrary, AC surface is not covered with such a structure. Instead, there were large clumps of particles near AC particles. In addition to that, daisy like disks could be seen on AC surfaces.

When particle deposition at 9 minutes was examined (Figure 4.2), we observed quite large particles on the surface or near the surface. For instance, 500 nm particles cover the ACO surface. Nevertheless, when these particles were examined at high optical magnifications, we observed a porous microstructure (Figure 4.3). In fact, these large clumps consisted of 50 nm iron oxide particles. At the initial stages of hydrolysis, β -FeOOH particles with similar dimensions started to cover the surface. It seemed that once the surface was covered, new particles started to form in the liquid and aggregated on each other, thus creating porous particles. Actually, reaction rates are very high with microwave heating [179], so this kind of heating may have caused bigger particles.

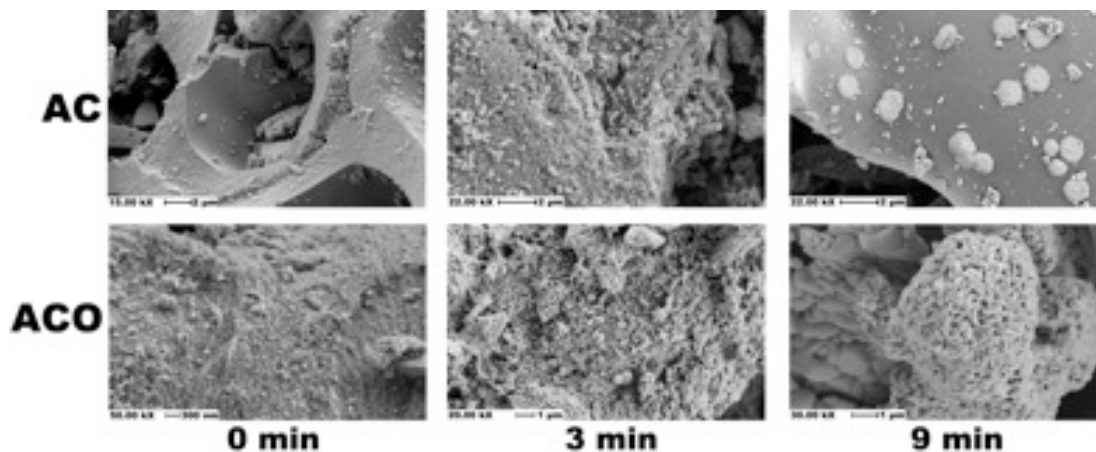


Figure 4.2. Iron deposited AC and ACO with various heating times

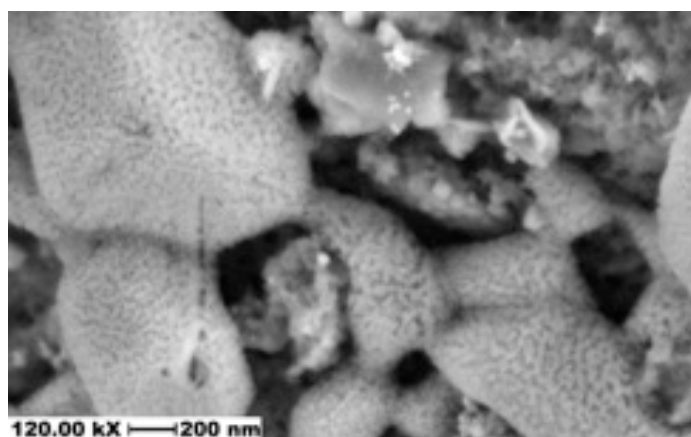


Figure 4.3. Close up of iron deposited ACO heated for 9 minutes

4.3.3. Porous Texture of the Adsorbents

The adsorption–desorption characteristics of the AC and ACO was characterized by N_2 physisorption. The isotherms for iron deposited AC prepared at different heating times are shown in Figure 4.4. All of the isotherms indicated similar trends to those of virgin AC. It was determined that the isotherms showed a type IV (IUPAC classification) behavior which characteristic for mesoporous materials. According to IUPAC, the hysteresis loop obtained belongs to type H4 hysteresis. These types of loops are often associated with narrow slit pores and include pores in the micropore region [180]. For both AC and ACO, we observed a decrease in adsorption-desorption characteristics with increasing heating time, which caused a decrease in the specific surface areas and

total pore volumes (Figure 4.4 and Table 4.1). The decrease in specific surface area and pore volume seemed to be mostly because of a decrease in the microporous volume. As a result, it could be suggested that during oxidation and iron oxide deposition, pore blockage and filling might have occurred. When meso and micropore volume fractions of AC and ACO were compared, we observed that they almost had the same values suggesting that oxidative medium affected the meso and micropores equally. Moreover, ACO supports' micropores were filled faster when compared with AC due easier penetration of pores with oxygen groups.

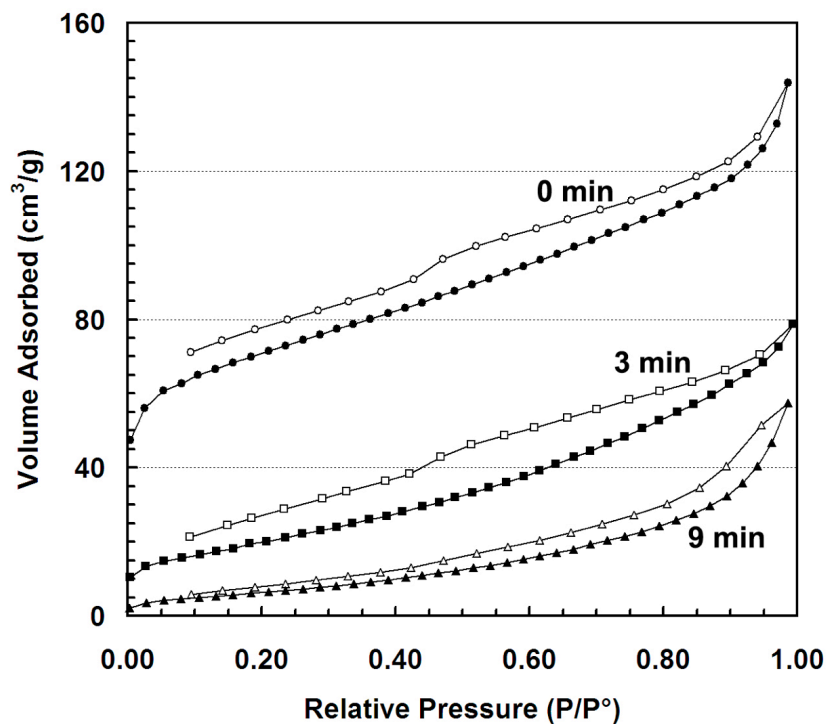


Figure 4.4. Nitrogen adsorption and desorption isotherms of ACO samples prepared at different heating durations

Table 4.1. Surface area and pore structure parameters for iron deposited AC & ACO

Sample	BET surface area (m ² /g)	V _{micro} (cm ³ /g)	V _{meso} (cm ³ /g)	Volume fractions (X _{meso} - X _{micro})	Pore size(Å)
AC-0	1313	0.505	0.679	0.57 – 0.43	18.1
AC-3	770	0.293	0.442	0.60 – 0.40	18.1
AC-9	43	0.014	0.071	0.84 – 0.16	17.9
ACO-0	256	0.098	0.120	0.55 – 0.45	18.0
ACO-3	74	0.025	0.093	0.79 – 0.21	17.8
ACO-9	26	0.007	0.090	0.93 – 0.07	18.0

4.3.4. Effect of Heating Duration on Iron Loading

The amount of iron deposited on supports with changing heating time is shown in Table 4.2. The effect of oxidation on iron oxide deposition can be clearly seen from the results. Even after 3 minutes of heating, iron deposition on ACO was 19.37 %. On the other hand, for AC under the same condition, iron content was just 2.13 %. Since ACO surface was covered with carbon-oxygen groups, hydrolysis started easily anywhere on the surface at the early stages of heating. However, for AC, hydrolysis would be delayed because of the lack of oxygen containing species. The hydrolysis most probably would occur in liquid, not on the surface, due to the hydrophobic nature of AC. That was the reason of obtaining low iron loading on AC. After 9 minutes of heating, iron loading on ACO reached to 20.37 %. For AC, the amount of iron was close to that value. This explained that once the iron oxide species were formed, hydrolysis became easier on AC.

Table 4.2. Iron loading on AC & ACO

Sample	Fe loading wt (%)	
	3 min	9 min
AC	2.13	19.53
ACO	19.37	20.37

4.3.5. Adsorption Isotherms

The As(V) sorption studies onto the synthesized nanoparticles were investigated by changing the initial sorbate concentrations ranging from 0.5 to 20 mg/L. As a potential water treatment material, these materials performance were studied at pH 7.0. The nonlinear As(V) adsorption isotherms of these materials are given in Figure 4.5. The maximum adsorption capacity was 27.78 mg/g, which was obtained with ACO-9 min. To examine adsorption performance, Langmuir [130], Freundlich [181], and Sips (Langmuir–Freundlich) [182] isotherm models were utilized. The calculated isotherm parameters of all three models were summarized in Table 4.3. Langmuir model assumes that single species of the sorbate adsorbs on specific homogenous adsorption sites within the sorbent by forming monolayer coverage. On the other hand, in Freundlich model, heterogeneous adsorption sites and interactions are considered [130, 181]. Langmuir (Equation 4.1) and Freundlich (Equation 4.2) isotherms can be expressed with the following equations:

$$q_e = \frac{q_{mon} b C_e}{1 + b C_e} \quad (4.1)$$

$$q_e = K_F C_e^{1/n} \quad (4.2)$$

where q_e is the solute amount adsorbed per unit weight of adsorbent (mg/g), C_e is liquid phase sorbate concentration in equilibrium, q_{mon} is the monolayer adsorption capacity (mg/g), K_F indicates the adsorbent's relative adsorption capacity (mg/g), $1/n$ is the constant representing adsorption intensity and b is the adsorption equilibrium constant (L/mg) related to adsorption enthalpy.

The Sips isotherm model is a combined form of Langmuir and Freundlich equations and possesses a finite saturation limit when the initial sorbate concentration is sufficiently high. The nonlinear form of Sips sorption isotherm is:

$$q_e = \frac{K_{LF} C_e^{n_{LF}}}{1 + (a_{LF} C_e)^{n_{LF}}} \quad (4.3)$$

where K_{LF} , a_{LF} , and n_{LF} are the Sips isotherm constants. The variation of Sips from Langmuir equation is the additional n_{LF} parameter. If n_{LF} parameter is 1 then the equation reduces to the Langmuir equation which represents homogeneous surfaces. However, the deviation further away from unity points out heterogeneity of the system.

Considering the R^2 values shown in Table 4.3 and Figure 4.5, the adsorption isotherm behavior of As(V) was better fitted to Langmuir isotherm when compared with Freundlich model. As(V) removal with fresh AC and ACO is very low and almost stays constant with changing initial concentration. For that reason, R^2 values are relatively smaller but still satisfies Langmuir model. In addition to that, for Sips model, the calculated n_{LF} values were found to be close to unity, which actually satisfies the Langmuir model. This means that a homogeneous adsorption occurs on these surfaces with monolayer coverage. From q_{mon} data, it can be concluded that with increasing heating time, adsorption capacity increases. However, when iron oxide loading and surface area values (Table 4.1 & 4.2) were put side by side with these capacity values, we observed that after 9 minutes of heating, although iron oxide amount increased, capacity did not increase that much. This suggested that available iron oxide surface disappeared after certain duration of heating. Highest capacity was calculated as 27.78 mg/g, when ACO was heated for 9 minutes. Nevertheless, these values were still high when compared with literature. For example Rangel-Mendez & Vitela-Rodriguez [183], and Fierro et al. [184] studied As(V) removal with iron-doped activated carbons. Maximum capacities obtained were 1.250 and 0.036 mg/g respectively. However, there are also some studies with higher uptake values like 51.3 mg/g [82].

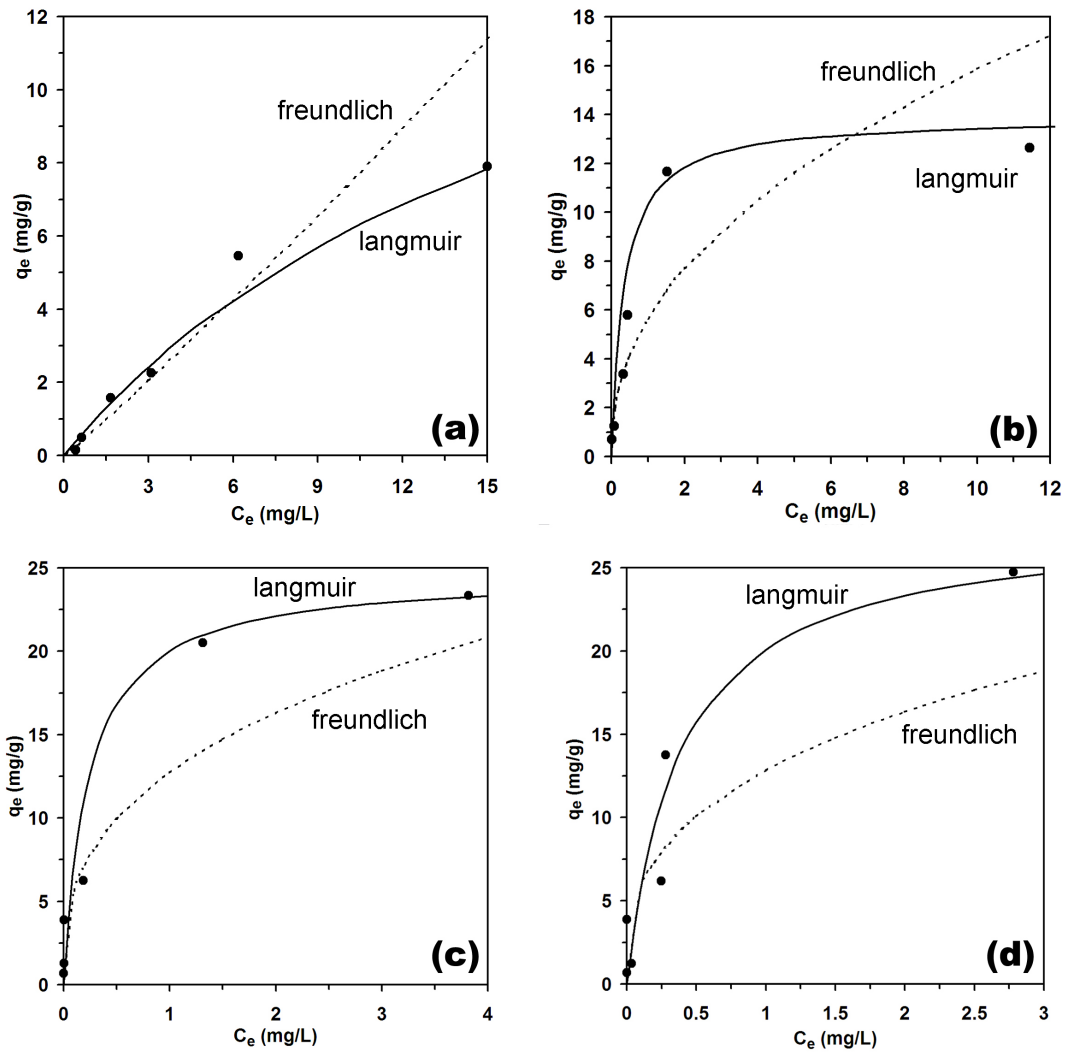


Figure 4.5. Adsorption isotherm of As(V) adsorbed by **(a)** AC-3min, **(b)** ACO-3min, **(c)** AC-9min and **(d)** ACO-9min (initial concentration = 0.5–20 mg/L, pH = 7.0, S:L = 750 mg/L, contact time = 24 h)

Table 4.3. Langmuir, Freundlich, and Sips isotherm parameters for fresh and iron deposited AC and ACO

Isotherm Parameters	AC	AC-3min	AC-9min	ACO	ACO-3min	ACO-9min
Langmuir						
q _{mon} (mg/g)	1.22	15.34	24.69	0.35	13.89	27.78
b (L/mg)	1.393	0.068	4.263	1.035	2.880	2.609
R ²	0.881	0.962	0.984	0.794	0.998	0.903
Freundlich						
K _F (mg/g)	0.769	0.639	12.747	1.651	5.648	12.844
1/n	0.508	1.061	0.355	1.054	0.449	0.348
R ²	0.748	0.941	0.867	0.430	0.912	0.650
Sips						
K _{LF} (L/g)	1.70	0.92	143.68	0.34	25.45	72.46
a _{LF} (L/mg)	1.392	0.044	5.966	1.03	1.922	2.611
n _{LF}	0.999	0.999	0.999	0.999	0.999	0.999
R ²	0.880	0.921	0.984	0.794	0.996	0.903

4.3.6. Adsorption Kinetics

In 1993, WHO lowered the guideline value for arsenic in drinking water from 50 µg/L down to 10 µg/L [185]. Furthermore, it is stated that ground water arsenic contamination can reach from 100 to 3900 µg/L [186]. Therefore, for kinetic modeling, an initial concentration like 5.0 mg/L, which was at the upper limit, would be appropriate. Highest adsorption capacities were obtained with samples heated for 9 minutes. For that reason, kinetic modeling was studied with AC, AC-9 min, ACO, and ACO-9min. The kinetic profiles of As(V) adsorption with AC-9 min and ACO-9min are illustrated in Figure 4.6. It was noted that at the very beginning of the experiment, adsorption percentages of As(V) reached to high values. For AC-9min, just at the 5th minute, adsorption percentage reached 99.56% and for ACO-9min, at that instant the percentage is 99.90%. When profiles were compared, ACO-9 min reached equilibrium

much faster than AC-9 min. Most probable reason for this was, for ACO version, the surface was covered more homogeneously with iron oxide, while for AC version there were large aggregates of iron oxide. Diffusion through these aggregates might have taken much more time. Actually, it is reported that such biphasic behavior is likely to occur from the variety of reactive sorption sites and/or the diffusion of adsorbate ions on the surface for seeking available sites [187]. After 24 hours, with ACO-9 min, concentration dropped to below detection limits, and with AC-9 min concentration was 6 µg/L. Conversely, supports without any iron deposition did not show any good performance. Their uptake values were low and stayed almost constant. While average uptake for AC was 0.72 mg/g, it decreased to 0.18 mg/g for ACO. This decrease might be probably because of surface charges. Zhang et al. [188], showed that after oxidation with KMnO₄, carbon surface becomes more basic after pH of 5.1. Consequently, at pH 7.0, surface of ACO became negatively charged and it started to repel anions, thus resulting in smaller uptake values.

To investigate the rate-controlling step for the sorption processes, four different kinetic models were studied. These models were pseudo-first-order equation (Equation 4.4) [122], the pseudo-second-order equation (Equation 4.5) [189], the Elovich equation (Equation 4.6) [190] and intraparticle diffusion (Equation 4.7) [127]. The linear mathematical forms of kinetics equations used are shown below:

$$\log(q_e - q_t) = \log(q_e) - \frac{k_1}{2.303}t \quad (4.4)$$

$$\frac{t}{q_t} = \frac{1}{k_2 q_e^2} + \frac{t}{q_e} \quad (4.5)$$

$$q_t = \frac{1}{\beta} \ln(\alpha\beta) + \frac{1}{\beta} \ln(t) \quad (4.6)$$

$$q_t = k_{\text{int}} t^{0.5} + C \quad (4.7)$$

where q_t is the amount of adsorbed contaminant (mg/g) at time t , q_e is the maximum adsorption capacity (mg/g) for the pseudo-first-order adsorption and pseudo-second-order adsorption, k_1 is the pseudo-first-order rate constant for the adsorption process (1/min), k_2 is the pseudo-second-order rate constant (g/mg min), constant α (mg/g min) is the initial adsorption rate, β (g/mg) is related to surface coverage, and k_{int} is the constant for the particle diffusion rate (mg/g min^{1/2}). The sorption modeling parameters are summarized in Table 4.4.

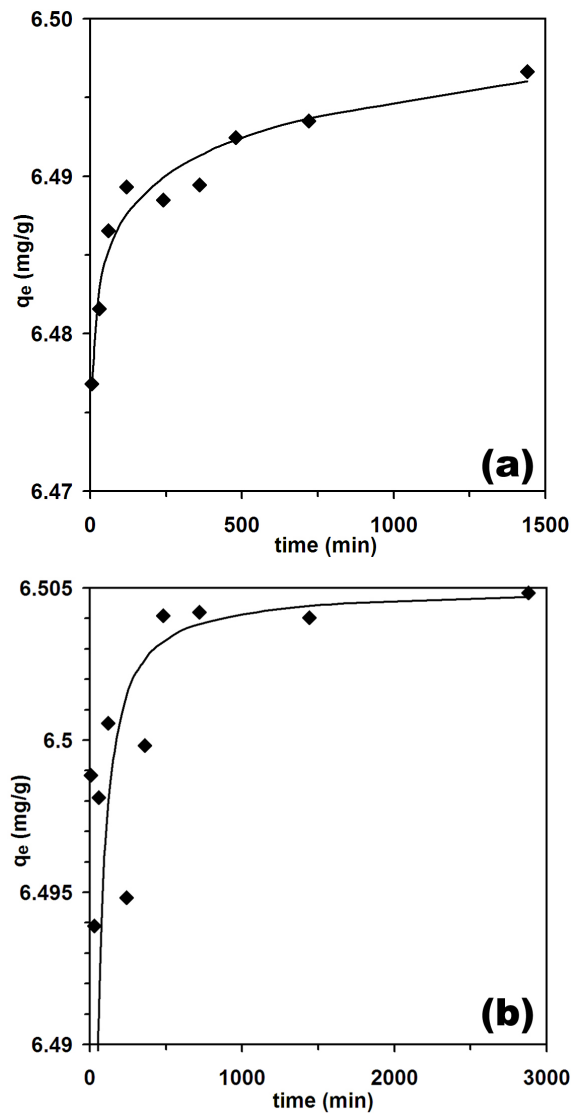


Figure 4.6. Kinetic profile and pseudo-second-order model fit of As(V) onto (a) AC-9min, and (b) ACO-9min (initial concentration = 5.0 mg/L, pH = 7.0, S:L = 750 mg/L).

Table 4.4. The kinetic sorption modelling parameters of As(V) on AC-9min and ACO-9min.

Model	Parameters	AC-9min	ACO-9min
Pseudo-first-order	k_1 (1/min)	0.0025	0.0007
	q_{e1} (mg/g)	0.016	0.007
	R^2	0.959	0.610
Pseudo-second-order	k_2 (g/mg min)	0.677	1.177
	q_{e2} (mg/g)	6.50	6.51
	R^2	0.999	0.999
Elovich equation	β (g/mg)	294.118	714.286
	α (mg/g min)	-	-
	R^2	0.958	0.464
Intraparticle diffusion	$k_{1\text{ int}}$ (mg/g min ^{1/2})	0.0015	0.0012
	R_1^2	0.975	0.939
	$K_{2\text{ int}}$ (mg/g min ^{1/2})	0.00026	0.00002
	R_2^2	0.996	0.997

The pseudo-second-order model appeared to be the best-fitting model for the removal of As(V) for the highest R^2 values (Table 4.4, Figure 4.6). This good fit with the pseudo-second-order model suggested that chemical adsorption is the rate limiting step on iron deposited AC and ACO [189] and the adsorption rates were proportional with the square of the number of sites on the adsorbent surface. Profile of ACO-9 min did not fit pseudo-first-order or Elovich model. On the other hand, profile of AC-9 min also fitted to these models with a little smaller R^2 values. Also in literature, with similar structures, pseudo-second-order model was suggested for As(V) adsorption [183].

For the aim of comparison, kinetic data were also evaluated using the intraparticle diffusion equation. The intraparticle diffusion can be considered as the rate-determining step, if the linearized curve passes through the origin (0, 0). Actually, the obtained R^2 values were high for pseudo-second-order model, and the results of fitting did not pass through the origin (0, 0) but very close to it. Therefore, it could be considered that

intraparticle diffusion might have some contribution. In Table 4.4 and Figure 4.7 intraparticle diffusion parameters and model fit are shown. A plot of q_e vs. $t^{0.5}$ showed two separate regions with different slopes. Region I of the plot reflects film diffusion while region II, which illustrates a less steep slope, stands for the diffusion within the adsorbent. In fact, parameters for these models were too small because of almost instantaneous adsorption. However, they could still be interpreted. As can be seen from Figure 4.7, the diffusivities in film were same for both of the samples. This result was expected since both of the materials were similarly synthesized iron oxide particles. After being diffused through the film, for ACO-9min, diffusion ended at region II. This might suggest that all of adsorption has occurred at the surface of particle but not in the particle because of high uptake amount and thin iron oxide layer. Conversely, since AC-9 min had large aggregates of iron oxide, thus intraparticle diffusion could be observed.

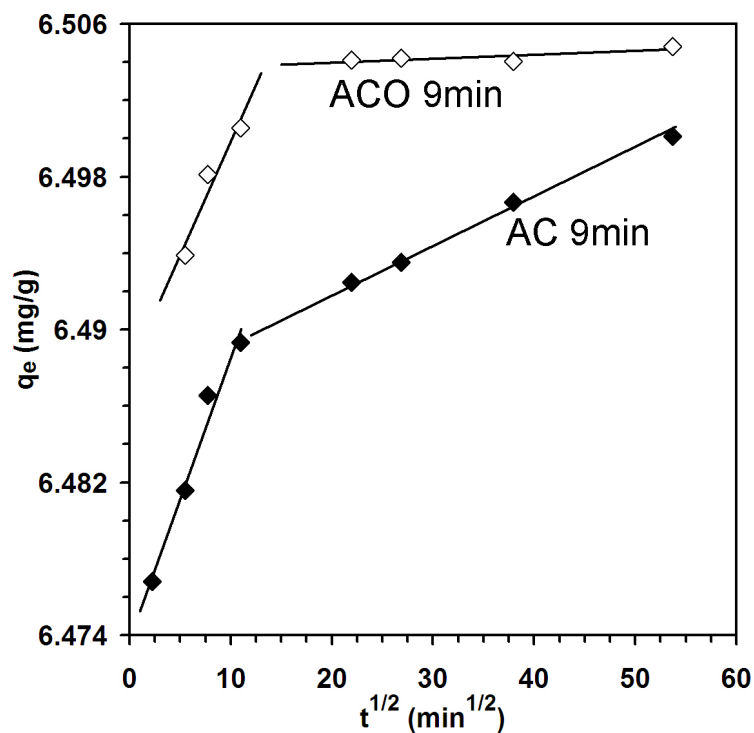


Figure 4.7. Intraparticle diffusion model fit of As(V) onto AC-9min, and ACO-9min (initial concentration = 5.0 mg/L, pH = 7.0, S:L = 750 mg/L)

4.3.7. Effect of solution pH

The As(V) uptake onto iron oxide deposited supports for an initial concentrations of 5.0 mg/L within a pH range of 3.0–8.0 are shown in Figure 4.8. The pH was an important parameter, which had an effect on surface properties of adsorbent. At pH was close to 4.0, uptake was 41.54 %. Moreover, with increasing pH, uptake amount decreased and the uptake value was close to zero at pH 7.7. According to Zhang et al. [188], point of zero charge pH of ACO is 5.1, so at pH values greater than that, no significant adsorption is expected. Also Luo et al.'s study shows that at pH values lower than 4.0 As(V) is in the form of H_3AsO_4 [191]. This means that no attraction will occur at pH values lower than 4.0. On the contrary, AC uptake capacity was relatively inferior. From pH 3.0 to 8.0, uptake amount increased slightly from 0.42 to 0.56 mg/g (not shown in figure). After deposition with iron oxide, AC-9 min and ACO-9 min responded similarly to changing pH. From pH 4.0, with increasing pH value, the As(V) uptake increased. For AC-9 min maximum percentage of 99.96% was reached at pH 5.8 and for ACO-9min, uptake of 99.97% was obtained at 6.2. Similar findings were also reported in literature [192, 193]. Iron oxide has a zero point of charge pH of 8.5 [194]. This means that iron oxide deposited materials' surface charge is positive below that point. Because of that, adsorption is expected to occur below that point. In addition to that, at the pH range of 4.0 to 9.0, As(V)'s structure changes from $H_2AsO_4^-$ to $HAsO_4^{2-}$ [191]. According to that, with increasing pH, adsorption and electrostatic attraction between arsenate and iron oxide should increase until pH 8.5. This also the situation happened in our case.

Variations of pH_{final} against $pH_{initial}$ of batch experiments for As(V) sorption are also illustrated in Figure 4.8. For adsorption on ACO, it has been seen that the solution pH_{final} was greater than $pH_{initial}$. This was likely due to the uptake of H^+ ions by the oxidized solid surface at the studied pH range. On the other hand, for iron deposited samples, pH_{final} was lower than $pH_{initial}$. Which means that, during adsorption, positively charged surface starts to release H^+ ions.

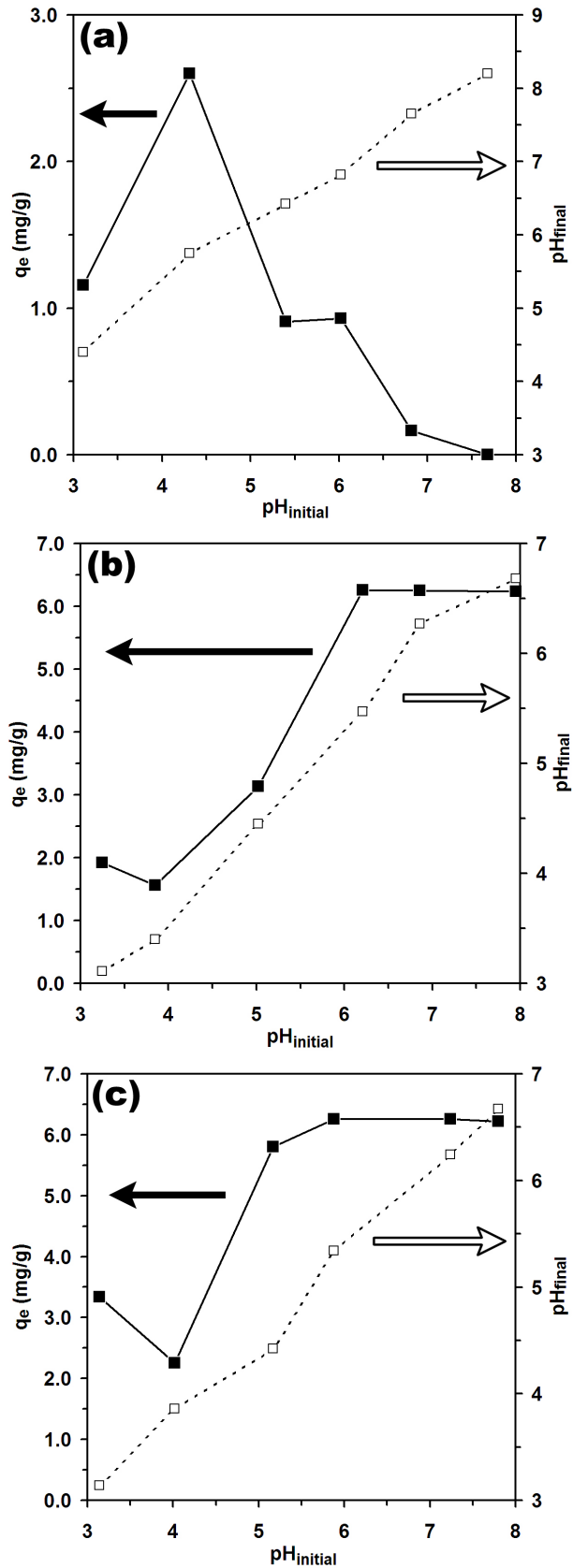


Figure 4.8. Adsorption of As(V) as a function of pH and by pH_{final} versus $pH_{initial}$ for (a) AC0, (b) ACO-9min, and (c) AC-9min (initial concentration = 5.0 mg/L, S:L = 750 mg/L, contact time = 24 h)

4.4. Concluding Remarks

In the present chapter, iron oxide nanoparticles were deposited on to activated carbon with a new technique and showed very promising results. Moreover, this material can also find its place in catalysis area. Iron oxide nanoparticles could be deposited uniformly on activated carbon support rapidly with high loadings with microwave hydrothermal treatment. XRD analyses revealed that not only α -Fe₂O₃, but also β -FeOOH particles could be generated with the adjustment of heating duration. With this method, about 20% of iron loading was obtained in less than 9 minutes. Uniformity and amount of iron oxide could be adjusted with surface oxidation and duration of microwave heating. However, adsorption isotherms and porous texture studies indicated that, available sites started to disappear at extended times of heating due to agglomeration of iron oxide particles on the surface. Nevertheless, for ACO, high As(V) uptake value like 27.78 mg/g was obtained and 99.90% of uptake was reached within 5 minutes of batch adsorption process. With adsorption isotherm and kinetic studies, it was understood that As(V) adsorption onto iron oxide deposited AC and ACO fits Langmuir and pseudo-second order models. High As(V) uptakes were obtained in the range of pH 6.0-8.0. The high As(V) adsorption performance, especially at pH 7.0, makes the material a good candidate for water treatment processes.

CHAPTER 5

**SYNTHESIS AND CHARACTERIZATION OF ANATASE NANOADSORBENT
AND APPLICATION IN REMOVAL OF LEAD, COPPER AND ARSENIC
FROM WATER**

5.1. Background

Lead, copper, and arsenic are well-known inorganic contaminants in drinking water [195]. Arsenic is introduced into environment by geochemical reactions, natural weathering reaction, mining activities, industrial wastes and volcanic emissions [9]. However, the primary sources of lead and copper are the corrosion of pipes, faucets, household plumbing systems, mining, smelting and battery manufacturing [196, 197]. Especially, the accumulation of arsenic, lead, and copper in the body may reach toxic levels. Long-term consumption of even low levels of arsenic could be dangerous as it can result in lung, skin, liver, bladder, and kidney cancers [198, 199]. Similarly, lead poisoning in human causes severe harm to the kidney, nervous system, liver and brain. Moreover, chronic exposure to lead has been correlated with sterility, abortion, stillbirths and neo-natal deaths [200]. Although copper is one of the essential nutrients for good health, an excess of the metal can cause Wilson's disease [201]. The current allowable maximum contamination level (MCL) of lead, arsenic, and copper in drinking water as set by the United States Environmental Protection Agency (U.S. EPA) are 15 parts per billion (ppb), 10 ppb, and 1.3 parts per million (ppm), respectively [202].

The most common methods, which have been proposed to remove arsenic and heavy metal ions from an aqueous medium, contain solvent extraction, ultra-filtration, reverse osmosis, chemical precipitation, nanofiltration, ion exchange and adsorption [16, 97, 203]. Among these methods, adsorption is the most preferred method since it is highly efficient technique with particularly low operational cost and widely applicable range of adsorbents. The materials that are extensively used for the removal of arsenic, lead, and copper from water may comprise activated carbon, ion-exchange resins, red mud, activated alumina, biomass, chitosan, and carbon nanotubes [204-209].

The use of nanoparticles in water treatment has received a substantial interest due to their high specific surface area, mobility, and activity [210, 211]. Remarkably, titanium dioxide (TiO_2), which has many properties such as non-toxicity, relative cheapness and hydrophilicity, is becoming a new class of adsorbent material in the removal of organic and inorganic pollutants from water [31, 212]. Previous studies interpreted arsenic and heavy metals adsorption onto commercial TiO_2 containing both rutile and anatase crystalline forms of TiO_2 [213]. Anatase crystalline form of TiO_2 is well known as a matter with a high photocatalytic activity due to its strong oxidizing power and favorable band gap energy. As anatase is illuminated, electrons and holes are generated and various chemical redox reactions are initiated due to the migration of those pairs to the anatase surface [214]. The electrons placed on the surface can promote the hydroxyl formation at the interface between surface and water [215]. Then, the formation of hydroxyl groups can increase the adsorption rate of metals from water. Moreover, the inherent capability of TiO_2 to convert As(III) to As(V) by photo-oxidation can provide an extra advantage [213]. Considering these properties, anatase crystalline type of TiO_2 can be used as sorbent material for the removal of contaminants from water.

This chapter presented a successful synthesis of anatase nanoadsorbent, and demonstrated fast and effective Pb(II), Cu(II) and As(III) removal from synthetically polluted water with the utilization of the nanoadsorbent. To the best of our knowledge, this is a comprehensive work about the assessment of the synthesized phase pure anatase nanoadsorbent for the removal Pb(II), Cu(II) and As(III) considering kinetics, equilibrium and thermodynamic properties.

5.2. Materials and Methods

5.2.1. Synthesis of Anatase Nanoadsorbent

Anatase nanoadsorbent was synthesized by sol-gel method at low temperature using titanium tetraisopropoxide (TTIP) ($C_{12}H_{28}O_4Ti$, 97%). A metal organic solution was prepared by mixing TTIP (10 mL) with 30 mL of 2-propanol (C_3H_8O , 99%) in a 250 mL flask and was kept stirring for 5 min under air. Secondly, the mixture of distilled water and 2-propanol was prepared separately with a volume ratio of 1:2. Afterwards, the metal organic solution was slowly added to the vigorous stirred second solution. After completion of the addition, the mixture was continued to mix for 2 h at 40°C. The sample was dried for several hours at 100°C and annealed at 400°C for 3 h.

5.2.2. Characterization

X-ray diffraction (XRD) measurement was done with a Brukeraxs advance powder diffractometer fitted with a Siemens X-ray gun and equipped with Brukeraxs Diffrac PLUS software. The sample was swept from $2\theta = 10^\circ$ through to 70° . The X-ray generator was set to 40kV at 40 mA. Raman spectrum was obtained from an InVia Reflex Raman microscope and spectrometer using a 532 nm diode laser excitation. Leo Supra 35VP field emission scanning electron microscope, Leo 32 and electron dispersive spectrometer software was used for images and analysis. Imaging was generally done at 2-5 keV accelerating voltage, using the secondary electron and in lens imaging techniques. The XPS measurements were performed using a Thermo K-alpha X-ray photoelectron spectrometer with a monochromated Al $K\alpha$ radiation and a combined low-energy electron/ion flood gun for charge neutralization. The binding energy scale for final calibration was corrected by C1s peak to 285.0 eV.

5.2.3. Batch Adsorption Experiments

The stock solutions containing 1000 mg/L of each lead and copper were prepared separately by dissolving 1.599 g $\text{Pb}(\text{NO}_3)_2$ (99.9%) and 2.9515 g $\text{Cu}(\text{NO}_3)_2$ (99.9%) in 1 L of deionized water. On the other hand, a standard arsenic solution (1000 mg/L) was prepared by dissolving 1.320 g As(III) (As_2O_3 , 99.9%) in 10 mL 5% (w/v) NaOH and making up to 1 L with deionized water. Batch adsorption experiments were carried out in 100 mL flasks, each containing 30 mL Pb(II), Cu(II) or As(III) ions solutions with appropriate concentrations. After the addition of 0.015 g of anatase nanoadsorbent each, the bottles were shaken in a controlled incubator shaker at 150-rpm and 25°C for 24 hours. The kinetic experiment were carried out at different time intervals (5 minutes to 36 hours) in an initial metal ion concentrations of 10 mg/L Pb(II), Cu(II), and As(III) in the solution at pH 6.0. Several initial concentrations ranging from 0.1 to 20 mg/L initial Pb(II), Cu(II), and As(III) of homogenous aqueous solutions were used for equilibrium studies at fixed pH 6.0 for 12 h. The effect of pH on the adsorptions were studied by using separately prepared 10 mg/L of Pb(II), Cu(II), and As(III) solutions in a pH range of 3.0-9.0 at 25°C. In the effect of temperature on Pb(II), Cu(II), and As(III) adsorptions, the temperatures were controlled to 298 K, 308 K and 318 K, respectively. At the end of each experiment the solution was separated from the solid adsorbent by using 0.45 μm PVDF membrane filter. Pb(II), Cu(II), and As(III) concentrations of the solutions were measured with a Varian, Vista-Pro CCD simultaneous inductively coupled plasma ICP-OES spectrophotometer. Samples before and after adsorption experiments were analyzed to obtain residual adsorbate ion concentrations. The blank experiments including different adsorbate concentrations were performed in the absence of the adsorbent to verify that no chemical precipitation occurred in the batch adsorption studies. In order to test the reproducibility, the experiments were carried in triplicate and average results were reported.

5.3. Result and Discussion

5.3.1. Characterization of the Nanoadsorbent

Figure 5.1 showed that XRD pattern of the anatase nanoadsorbent obtained by sol-gel synthesis. The characteristic diffraction peaks were indexed at 2θ of 25.2° (101), 37.8° (004), 48.0° (200), 54.8° (211), and 62.6° (220) planes of anatase phase of TiO_2 , respectively [216]. No other irrelevant peaks were observed indicating the sample was pure in anatase phase. The average size of the anatase crystallite was calculated by applying the Debye-Scherrer formula [217] to the main anatase (101) peak in XRD spectrum and the average crystallite size was found to be 7.97 nm.

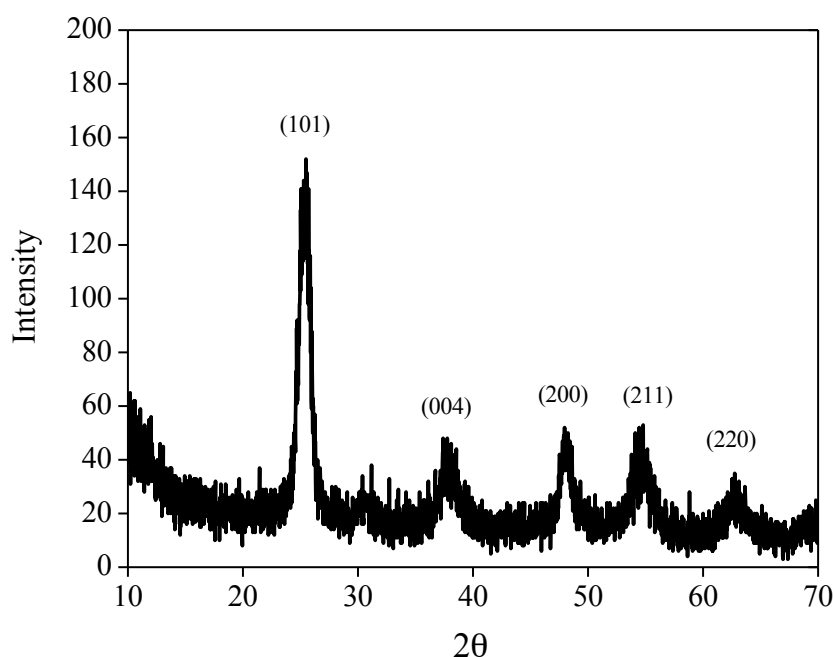


Figure 5.1. XRD pattern of the synthesized anatase nanoadsorbent.

Raman spectroscopy provides a rapid way of obtaining the surface crystal structure of the TiO_2 . The Raman spectrum of the adsorbent material used in here was shown in Figure 5.2, with the characteristic Raman lines giving evidence for the crystalline type of anatase rather than rutile and brookite. Anatase has six Raman active modes ($A_{1g} + 2B_{1g} + 3E_g$) and the Raman lines observed at 152.0 cm^{-1} , 399.0 cm^{-1} , 516.0 cm^{-1} , and

635.0 cm^{-1} assigned to the E_g , B_{1g} , A_{1g} , and E_g vibrational modes of anatase, respectively [212, 217]. The conclusion obtained from Raman spectra of sample was consistent with the XRD result indicated in Figure 5.1.

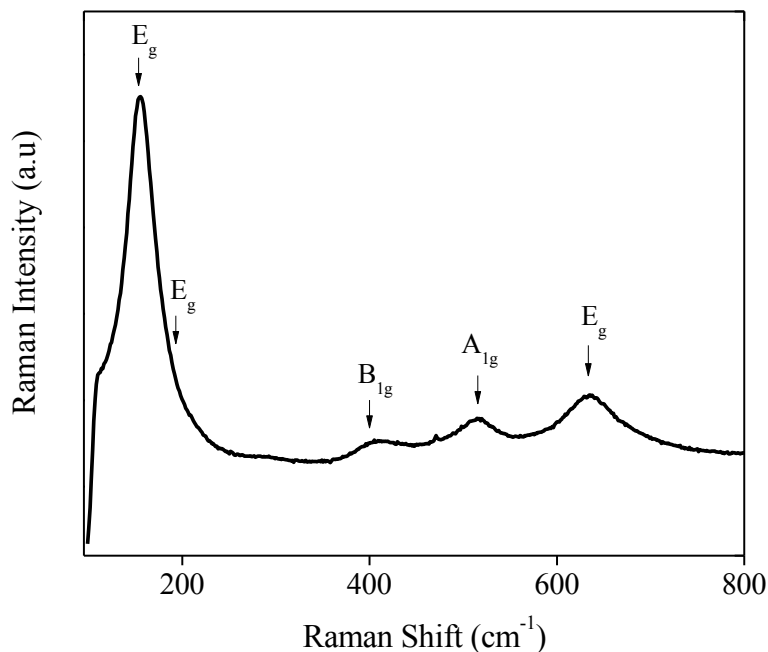


Figure 5.2. Raman spectra of the synthesized anatase nanoadsorbent.

The SEM (Figure 5.3) micrographs clearly indicated spherical morphology. The anatase nanoadsorbent was composed of spherical particles that were 20-60 nm in diameter. The observed particle sizes in SEM were found to be larger than the crystallite size calculated from the XRD line broadening due to agglomeration of the primary particles after the calcination. Similar finding was also found in previous works [218].

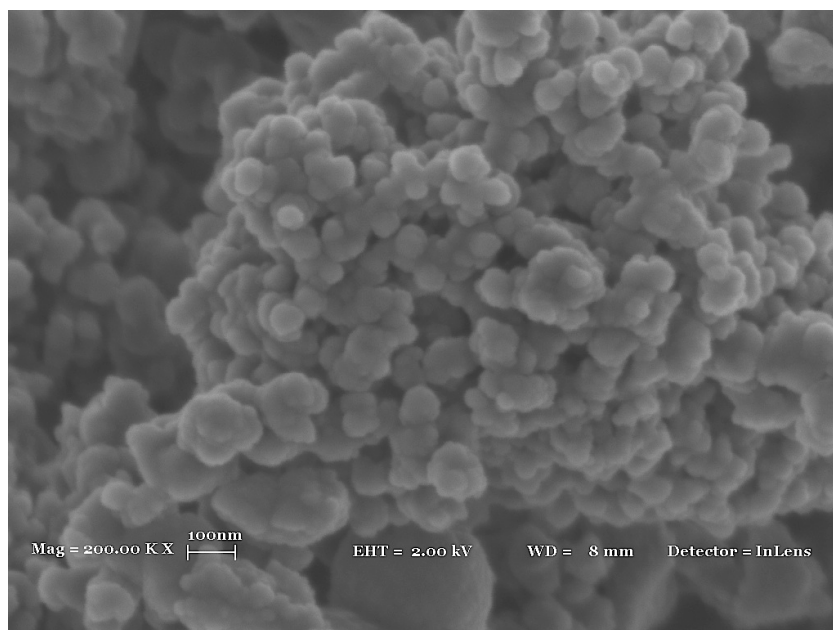


Figure 5.3. SEM image of (in lens detector) the synthesized anatase nanoadsorbent.

XPS, a highly surface selective technique, can provide quantitative chemical information as well as oxidation and structural environment of elements except hydrogen and helium. A typical wide scan XPS survey spectrum of the anatase nanoadsorbent was shown in Figure 5.4a and the distinct photoelectron peaks were observed for Ti2p and O1s peaks of the titanium dioxide. The total surface concentrations of Ti, O and C were 30.3, 62.3, and 7.4 at%, respectively. The titanium to oxygen ratio was 0.49:1, which is close to that expected from the stoichiometry of TiO_2 . A C1s peak was seen due to the deposition of adventitious hydrocarbon on the surface of sample from the pumps evacuating the analysis chamber [212]. The Ti2p and O1s narrow scans were illustrated in Figure 5.4b and Figure 5.4c. The $\text{Ti}2p_{1/2}$ and $\text{Ti}2p_{3/2}$ peaks were observed at 458.7 and 464.4 eV with a split of 5.7 eV between the doublets, indicating that Ti exists in the Ti^{4+} form [219]. The O1s XPS spectra demonstrated at least two O chemical states according to the binding energy range of 530.0-531.2 eV. The main contribution was attributed to Ti-O in the nanoadsorbent. The other minor peak was assigned to the OH groups presented on the surface of nanoadsorbent. The difference between the binding energies of the assigned oxide (O^{2-}) and hydroxyl (OH) species was 1.2 eV, which is close to reported differences of 1.5-1.9 eV in the literature [220].

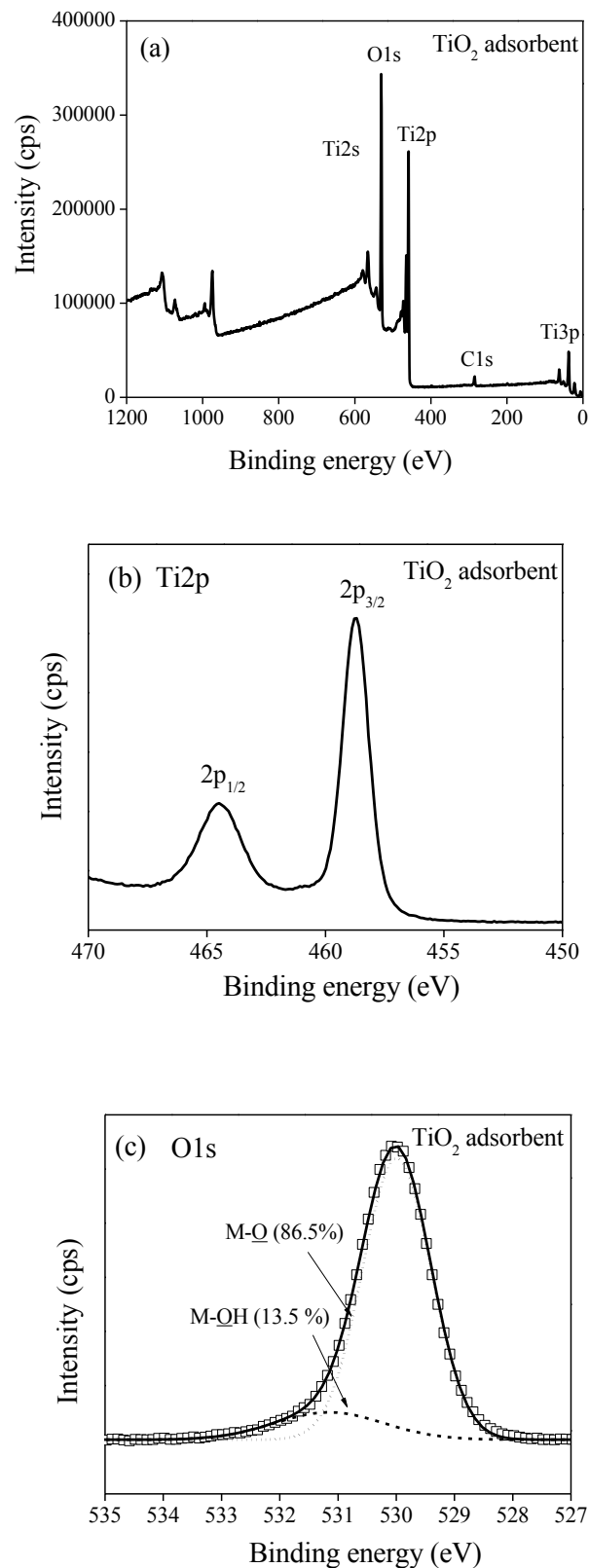


Figure 5.4. XPS spectra of (a) survey scan, (b) Ti2p, (c) O1s of anatase nanoadsorbent surface at pH 6.0.

5.3.2. Kinetic Studies and Mathematical Modeling

The kinetic profiles of Pb(II), Cu(II), and As(III) adsorption at pH 6.0 were illustrated in Figure 5.5. It was noted that at the beginning of the experiment the adsorption percentages of arsenic and heavy metal ions increased remarkably and then reached equilibrium. As can be seen in Figure 5.5a, there was a substantial increase in the As(III) adsorption percentage when contact time was increased from 5 to 180 min and the maximum As(III) uptake was obtained at 480 min of contact. On the other hand, Figure 5.5b and Figure 5.5c indicated the rapid adsorptions of Pb(II) and Cu(II) ions within the first 5 min of contact time because of the high affinity to the sorption sites. The fast adsorption trend at initial stage is mostly observed phenomenon in the removal of contaminants from water and it is most likely caused reactive chemical groups readily presented on the surface [221]. After initial fast reactions of adsorbate ions with the nanoparticles, the slower reactions were observed especially in the cases of removal of Cu(II) and As(III). Such biphasic behavior was likely resulted from the variety of reactive sorption sites and/or the diffusion of adsorbate ions on the surface for seeking available sites [222].

In order to investigate the rate-controlling step for the sorption processes, four kinetic models were studied by applying the experimental sorption data to the pseudo-first-order equation (Equation 5.1) [122], the pseudo-second-order equation (Equation 5.2) [189], the Elovich equation (Equation 5.3) [190] and intraparticle diffusion (Equation 5.4) [127]. The linear mathematical forms of kinetics equations used are shown below:

$$\log(q_e - q_t) = \log(q_e) - \frac{k_1}{2.303} t \quad (5.1)$$

$$\frac{t}{q_t} = \frac{1}{k_2 q_e^2} + \frac{t}{q_e} \quad (5.2)$$

$$q_t = \frac{1}{\beta} \ln(\alpha\beta) + \frac{1}{\beta} \ln t \quad (5.3)$$

$$q_t = k_{\text{int}} t^{0.5} + C \quad (5.4)$$

where, q_t is the amount of adsorbed contaminant (mg/g) at time t , q_e is the maximum adsorption capacity (mg/g) for the pseudo-first-order adsorption and pseudo-second-order adsorption, k_1 is the pseudo-first-order rate constant for the adsorption process (1/min), k_2 is the pseudo-second-order rate constant (g/mg.min), constant α (mg/(g.min)) is the initial adsorption rate, β (g/mg) is related to surface coverage, and k_{int} is the constant for the particle diffusion rate (mg/g.min^{1/2}). The fitting ability of kinetic and adsorption models were analyzed according to the average percent error (APE) given in below:

$$APE = \frac{\sum_{i=1}^n \frac{q_{exp} - q_{cal}}{q_{exp}}}{N} \times 100 \quad (5.5)$$

where N is the number of data points. The subscripts “exp” and “calc” show the experimental and calculated values. Error function was employed in this study to find out the most suitable isotherm model to represent the experimental data. The APE minimizes the fractional error distribution across the entire concentration range [223]. Small values of APE represent better fits of the model to the data. The sorption modeling parameters and APE values were summarized in Table 5.1.

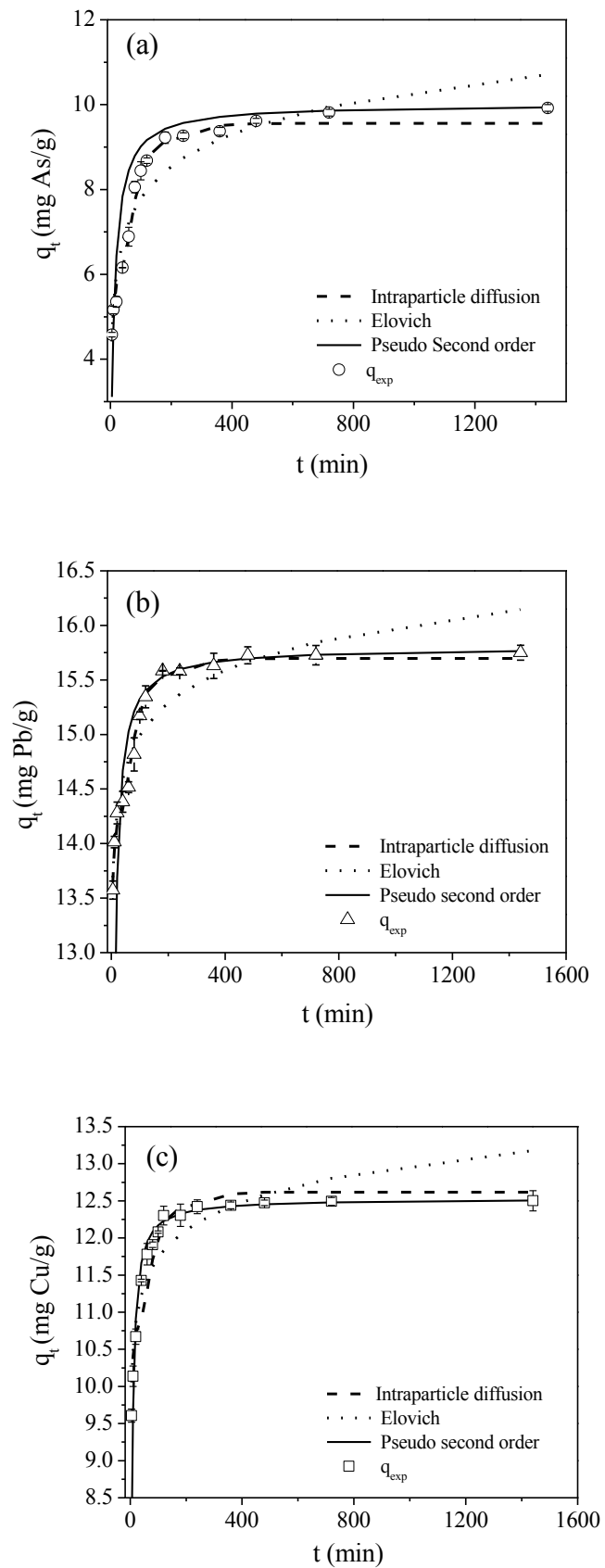


Figure 5.5. Kinetic modeling of sorption of (a) As(III), (b) Pb(II), and (c) Cu(II) onto synthesized anatase nanoparticles [Temperature = 25°C, pH = 6.0, S:L = 500 mg/L].

Table 5.1. The kinetic sorption modelling parameters of Pb, Cu, and As on the anatase nanoparticles at pH 6.0.

Model	Parameters	Pb(II)	Cu(II)	As(III)
Pseudo First Order	$k_1(1/\text{min})$	0.001	0.001	0.003
	$q_{e1}(\text{mg/g})$	1.198	8.356	3.119
	R^2	0.539	0.493	0.646
	APE	98.17	97.98	64.29
Pseudo Second Order	$k_2(\text{g/mg}\cdot\text{min})$	0.021	0.027	0.005
	$q_{e2}(\text{mg/g})$	15.79	12.53	9.980
	R^2	0.999	0.999	0.998
	APE	2.605	1.139	5.178
Elovich Equation	$\beta (\text{g/mg})$	2.306	1.840	0.911
	$\alpha (\text{mg/g}\cdot\text{min})$	4506	1289	13.16
	R^2	0.917	0.986	0.939
	APE	0.002	0.104	0.452
Intraparticle Diffusion	$k_{\text{int}}(\text{mg/g}\cdot\text{min}^{1/2})$	22.04	27.58	55.20
	R^2	0.986	0.919	0.990
	APE	0.001	0.080	0.069

The pseudo second order model appeared to be the better-fitting model for the removal of Pb(II), Cu(II), and As(III) because it has the highest R^2 (0.999, 0.999, 0.998) and lower APE (2.605, 1.139, 5.178) values. Good agreements with the pseudo-second-order model suggested that chemical adsorption was the rate-limiting step [189] and the adsorption rates were proportional to the square of the number of sites on the adsorbent

surface. On the other hand, the higher R^2 values found in the Elovich model for Cu(II) and As(III) indicated that the adsorbing surface was heterogenous and therefore exhibited different activation energies for chemisorption. The constant α is related to the rate of chemisorption [223] and higher value for α was obtained for Cu(II) indicating a fast kinetic process. For comparison purposes, kinetic data were also evaluated using the intraparticle diffusion equation. The intraparticle diffusion can be considered as the rate-determining step, if the linearized curve passes through the origin (0, 0). Although, the obtained R^2 values were comparably high with the pseudo-second-order model for all three adsorbates, the results of fitting did not pass through the origin (0, 0) interpreting that intraparticle diffusion was not the rate-determining step in the adsorption processes. Such a finding was similar to that made in previous works on adsorption [224]. Moreover, due to the apparent lack of linear behavior, the pseudo-first-order, which considers specifically single class of sorbing sites, was not suitable to describe the kinetic profiles. According to the results in Table 5.1 obtained from the above kinetic studies and based on the R^2 and APE values considering the entire contact time for the three contaminants, it can be concluded that the pseudo-second-order and Elovich models best explained the Cu(II) and As(III) adsorption kinetics, whereas the pseudo-second-order model described the Pb(II) adsorption kinetics. Furthermore, the experimental data indicated better agreement for models that describe adsorption to heterogeneous surfaces except for Pb(II) adsorption.

5.3.3. Adsorption Isotherms

The Pb(II), Cu(II), and As(III) sorption studies onto the nanoparticles were investigated by varying the initial sorbate concentrations ranging from 0.1 to 20 mg/L at pH 6.0. The nonlinear Pb(II), Cu(II), and As(III) adsorption isotherms were given for the anatase nanoparticles in Figure 6. The maximum adsorption capacities were found 31.25 mg/g for Pb(II), 23.74 mg/g for Cu(II), and 16.95 mg/g for As(III). In order to investigate adsorption performance, Langmuir [130], Freundlich [225], Redlich-Peterson [226], and Sips (Langmuir-Freundlich) [182] isotherm models were utilized. The calculated isotherm parameters of all four models were summarized in Table 5.2. Langmuir model assumes that single specie of the sorbate adsorbs on specific homogenous adsorption

sites within the sorbent by forming monolayer coverage. However, Freundlich model is derived considering a theory of the heterogeneous adsorption sites and interactions [130, 225]. Langmuir (Equation 5.7) and Freundlich (Equation 5.8) isotherms can be expressed by the following equations:

$$q_e = \frac{q_{mon} b C_e}{1 + b C_e} \quad (5.7)$$

$$q_e = K_F C_e^{1/n} \quad (5.8)$$

where q_e is the solute amount adsorbed per unit weight of adsorbent (mg/g), C_e is liquid phase sorbate concentration in equilibrium, q_{mon} is the monolayer adsorption capacity (mg/g), K_F indicates the adsorbent's relative adsorption capacity (mg/g), $1/n$ is the constant representing adsorption intensity and b is the adsorption equilibrium constant (L/mg) related to adsorption enthalpy ($b \propto \exp^{-\Delta H/RT}$).

The Redlich-Peterson isotherm model, which can be applied in either homogeneous or heterogeneous systems due to its versatility, can be described as follows:

$$q_e = \frac{K_{RP} C_e}{1 + a_{RP} C_e^{\beta_{RP}}} \quad (5.9)$$

where K_{RP} is Redlich-Peterson isotherm constant (L/g), a_{RP} is Redlich-Peterson isotherm constant (L/mg) ^{β_{RP}} and β_{RP} is the exponent which lies between 0 and 1. The β_{RP} parameter (dimensionless) represents the heterogeneity of the binding surface. If β_{RP} tends to unity Redlich–Peterson model results in Langmuir model. When β_{RP} tends to zero Redlich–Peterson model represents Henry law. The Sips isotherm model, which is combined form of Langmuir and Freundlich equations, possesses a finite saturation limit when the initial sorbate concentration is sufficiently high. The nonlinear form of Sips sorption isotherm is:

$$q_e = \frac{K_{LF} C_e^{n_{LF}}}{1 + (a_{LF} C_e)^{n_{LF}}} \quad (5.10)$$

where K_{LF} , a_{LF} , and n_{LF} are the Sips isotherm constant. The difference between this equation and Langmuir equation is the additional n_{LF} parameter in the Sips equation. If n_{LF} parameter is unity, the equation effectively reduces to the Langmuir equation appropriate for ideal surfaces. On the other hand, the deviation further away from unity indicates heterogeneity of the system.

Considering the APE error percentages and R^2 values, the adsorption isotherm behavior of Pb(II) was better fitted to Sips isotherm, followed by Langmuir isotherm. The calculated n_{LF} value was found to close to unity, therefore, the Langmuir model successfully explained the adsorption of Pb(II) ions onto the nanoparticles. Additionally, the suitability of Langmuir isotherm model to the Pb(II) sorption data was also supported by the obtained dimensionless parameter value in Redlich-Peterson, which was also close to unity. On the other hand, the deviation of n_{LF} parameter further away from unity indicates heterogeneity of the system. This was the case of adsorption of Cu(II), which fitted better to the Freundlich model, followed by the Sips model. However, the system heterogeneity might be resulted from the sorbate or sorbent or a combination of both. Moreover it can be seen that As(III) fitted better to the Langmuir isotherm model followed by Redlich-Peterson isotherm model according to R^2 values. However, Langmuir model with the high APE error reduced the applicability of model to the experimental data. Therefore, the lower APE error in between experimental and calculated data was required to obtain the appropriate evaluation for the adsorption of As(III). As can be seen in Table 5.2, the Freundlich and Redlich-Peterson isotherm models indicated a good agreement according to APE error percentages. The Redlich-Peterson isotherm equation reduced to Freundlich isotherm equation since the calculated a_{RP} value for As(III) adsorption was large enough. It can be concluded that the Langmuir model was more suitable for Pb(II) uptake supported with lower APE and higher R^2 value, in contrast the higher correlation between experimental and calculated adsorption data of Cu(II) and As(III) were observed in Freundlich isotherm model. Moreover, the K_F values achieved from the Freundlich model were 9.948 mg/g for Cu(II) and 8.729 mg/g for As(III), suggesting higher binding affinity of Cu(II) as compared to As(III).

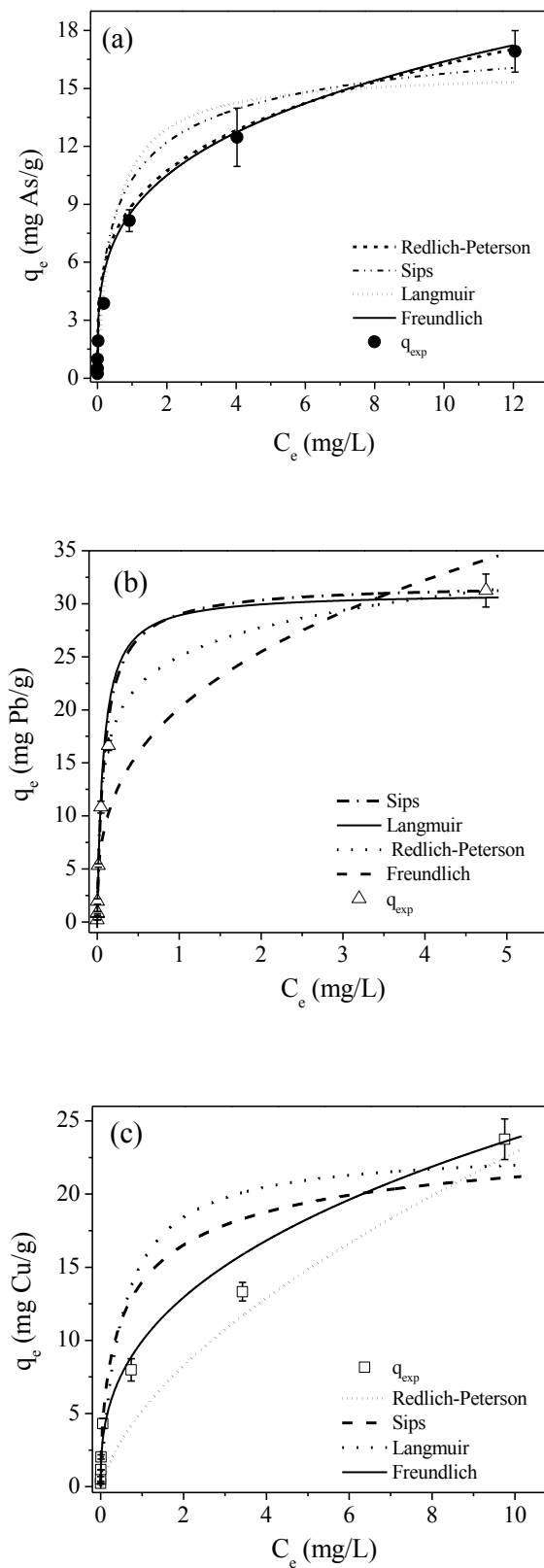


Figure 5.6. Adsorption isotherm of (a) As(III), (b) Pb(II), and (c) Cu(II) adsorbed by synthesized anatase nanoparticles [Initial concentration = 0.3–20 mg/L, Temperature = 25°C, pH = 6.0, S:L = 500 mg/L].

Table 5.2. Langmuir, Freundlich, Redlich_Peterson, and Sips, isotherm parameters for Pb(II), Cu(II), and As(III) removal on the anatase nanoparticles

Isotherm Parameters	Pb(II)	Cu(II)	As(III)
q_{exp}(mg/g)	31.25	23.74	16.95
Langmuir			
q _{mon} (mg/g)	31.05	23.09	16.83
b(L/mg)	13.42	1.968	3.644
R ²	0.999	0.929	0.986
APE	0.696	36.98	39.62
Freundlich			
K _F (mg/g)	30.17	9.948	8.729
1/n	0.539	0.379	0.354
R ²	0.836	0.989	0.951
APE	26.39	1.139	5.393
Redlich-Peterson			
K _{RP} (L/g)	90.09	3.966	2.490
a _{RP} (L/mg) ^{β_{RP}}	25.31	0.280	277.1
β _{RP}	0.876	0.331	0.743
R ²	0.995	0.968	0.981
APE	0.701	63.75	7.051
Sips			
K _{LF} (L/g)	31.94	25.71	21.99
a _{LF} (L/mg)	9.859	1.192	1.244
n _{LF}	0.950	0.592	0.588
R ²	0.999	0.987	0.965
APE	0.014	3.377	25.43

5.3.4. Adsorption Thermodynamics

In order to analyze the effect of temperature, experiments were carried out at temperatures of 25, 35, and 45°C and the following equations were used to calculate the thermodynamic parameters:

$$K_c = \frac{q_e}{C_e} \quad (5.11)$$

$$\Delta G = -RT \ln K_c \quad (5.12)$$

$$\ln K_c = \frac{\Delta S}{R} - \frac{\Delta H}{RT} \quad (5.13)$$

where K_c is an equilibrium constant between the adsorbed equilibrium concentration and the aqueous equilibrium concentration (L/g). Furthermore, ΔH (kJ/mol) and ΔS (kJ/mol K), which are the variation of enthalpy and entropy, were calculated (Table 5.3) from the slope and the intercept of $\ln K_c$ versus $1/T$ graphs.

Table 5.3. Thermodynamic parameters for Pb(II), Cu(II), and As(III) sorption on the anatase nanoparticles

$^{\circ}\text{C}$	<u>Pb(II)</u>			<u>Cu(II)</u>			<u>As(III)</u>		
	25	35	45	25	35	45	25	35	45
ΔG (kJ/mol)	-14.4	-17.9	-21.5	-6.56	-9.54	-12.5	-4.63	-4.08	-3.53
ΔH (kJ/mol)		91.76			19.36			-21.20	
ΔS (kJ/mol.K)		0.356			0.117			-0.055	

It has been stated that the value of ΔG found below 8 kJ/mol is consistent with a physical adsorption involving electrostatic interaction between adsorption sites and the adsorbate ion. Moreover, it has been noted that if the value of ΔG is in between 8 and 16 kJ/mol, the adsorption proceeds via a chemical ion exchange mechanism. The more negative ΔG values imply chemisorption mechanism by forming stable complexes on the adsorbent surface [227]. According to the results presented in Table 5.3, the values of ΔG for Pb(II) were found to range from -14.4 to -21.5 kJ/mol suggesting chemical adsorption as major mechanism responsible for the adsorption process. In the case of Cu(II) adsorption, the most probable type of reaction would be ion-exchange according to the values of ΔG . Furthermore, the calculated ΔS values were positive and the favorable Gibbs energies were entropically controlled since the adsorptions of Pb(II) and Cu(II) were endothermic signifying the decrease in uptake capacity by increasing the temperature. Due to increase in the randomness of the system at the adsorbate-adsorbent interface, the positive values for ΔS were observed for Pb(II) and Cu(II) together with the structural change during the adsorption process. In the case of As(III), physical adsorption might be the main mechanism since the calculated ΔG values were in the range of electrostatic interactions. Especially, the negative ΔH value of As(III) might be suggested that the physical adsorption was the leading mechanism of the adsorption.

The negative ΔG values were obtained for Cu(II), Pb(II), and As(III) adsorptions on the adsorbent by confirming the feasibility of the adsorption processes and the spontaneous nature of adsorptions. Moreover, the numerical values of $1/n$ which is calculated from the linearized form of Freundlich model was found between 0 and 1, indicated beneficial adsorptions [211]. In addition to that, from the adsorption equilibrium constant in Langmuir model, the dimensionless separation factor (R_L), which was the indicative of the isotherm shape, could be obtained by using the following equation:

$$R_L = \frac{1}{1 + b C_o} \quad (5.14)$$

where, C_o is the initial adsorbate concentration (mg/L). The value of R_L demonstrates the nature of adsorption as unfavorable ($R_L > 1$), linear ($R_L = 1$), favorable ($0 < R_L < 1$) and irreversible ($R_L = 0$) [207]. The R_L were found to be 0.427 to 0.0037 for Pb(II),

0.8356 to 0.0248 for Cu(II) and 0.4777 to 0.01353 respectively for As(III) indicating irreversible adsorptions of the sorbates on the anatase nanoadsorbent with the increase of initial sorbate concentration.

5.3.5. Effect of Solution pH

The uptakes of Pb(II), Cu(II), and As(III) onto the anatase nanoparticles for an initial concentrations of 10 mg/L within a pH range of 3.0-9.0 were shown in Figure 5.7a. The pH is a significant parameter for determining the adsorption between the adsorbent and aqueous interface. At pH 3.0, the adsorption percentages of the nanoadsorbent to Pb(II), Cu(II), and As(III) were 29.73%, 1.15%, and 51.76%, respectively. From pH 3.0 to 8.0, the uptake percentages of contaminants increased, 97.41% of Pb(II), 62.57% of Cu(II) and 49.29% of As(III) were removed at pH 6.0. Similar findings were also found in literature [208, 211, 215]. Compare to Pb(II) and Cu(II), the effect of pH on As(III) sorption on the anatase nanoadsorbent was nearly negligible in the pH range of 3.0-8.0 [213].

According to surface complex formation theory (SCF), the increase in the pH value leads to the decrease in the competition between proton and metal ions for the adsorption sites [228]. At acidic pH conditions surface of the anatase nanoparticles was mostly covered with positively charged surface groups, leading to more coulombic repulsion of the metal ions. Additionally, at lower pH values heavy metal ions possibly found less chance to form a complex with the adsorbent material due to the competition with hydrogen and heavy metal ions for the sorption sites. At higher pH values, the surface of adsorbent was covered with more negative charges and more sorption sites were available to attract the heavy metal ions. However, Pb(II) and Cu(II) ions could begin to precipitate as $Pb(OH)_2$ and $Cu(OH)_2$ at $pH > 6.0$. In the case of As(III) adsorption, the amount of negatively charged As(III) increased when the pH value was shifted to higher pH values [213]. Therefore, at higher pH value was not suitable for efficient As(III) adsorption onto the nanoparticles. At pH values from 3.0 to 8.0, the neutral As(III) species mostly existed and the interaction of neutral species with some hydroxyl groups presented on the surface of the nanoparticle could be observed [229].

Variations of pH_f against pH_i of batch experiments for Pb(II), Cu(II), and As(III) sorptions were illustrated Figure 5.7b. For As(III) adsorption, it has been seen that the solution pH_f was greater than the pH_i in the range of 3.0–8.0. However, after that, the final pH of the solution was decreased during sorption of As(III) by anatase nanoadsorbent. This was likely due to the uptake of H^+ ions by the solid surface at pH_i ranging from 3.0 to 8.0. In addition to that, the lowering of pH_f than pH_i can be ascribed by the releasing H^+ ions. In the case of Pb(II) and Cu(II) adsorption, the pH_f were higher than pH_i until pH 5.0. However, the decrease in final pH values were observed due to liberating H^+ ions after the reaction between the heavy metal ions with anatase nanoadsorbent.

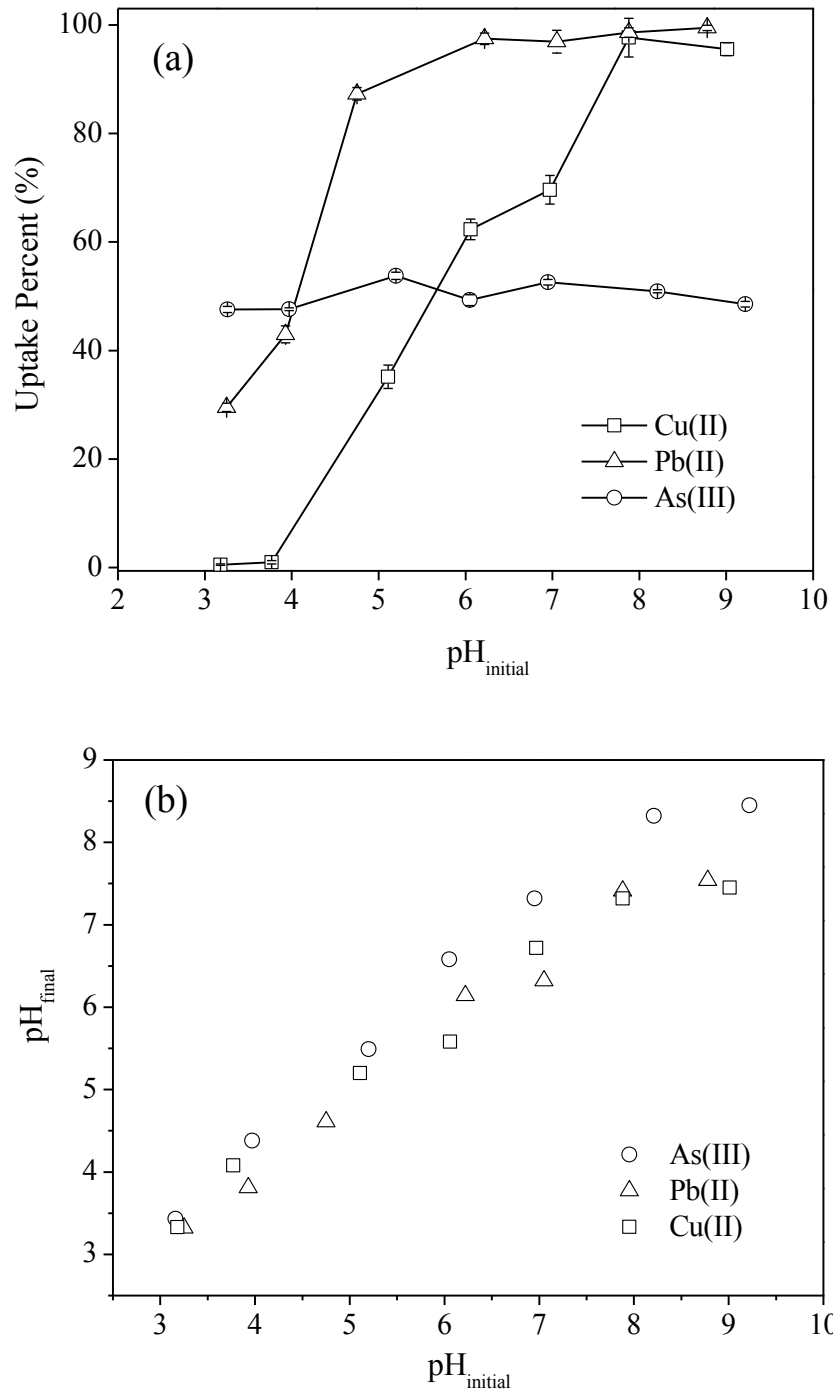


Figure 5.7. (a) Adsorption of 10 mg/L Pb(II), Cu(II), and As(III) as a function of pH by 500 mg/L synthesized anatase nanoparticles 25 °C (b) pH_{final} versus $pH_{initial}$ during the adsorption.

5.3.6. Proposed Binding Mechanism

The binding mechanisms of Pb(II), Cu(II), and As(III) to the anatase nanoparticles were mainly depended on the type of active sites on the surface of adsorbent and the concentrations of the produced sorbate species at measured pH value. In literature, the point of zero charge (pzc) for the anatase nanoparticles was approximately found in between 5.9-6.9 [230]. The anatase nanoparticles are composed of the mixture of positively charged TiOH_2^+ and neutral species of TiOH^0 when pH is below. However, the primary species of the nanoparticles include the neutral species of TiOH^0 and the negatively charged TiO^- when pH is above pH_{pzc} [143, 213]. Therefore, the surface of nanoparticles mostly covered with the neutral TiOH^0 and negatively charged TiO^- at pH 6.0. Bonato et al. presented experimental study in order to determine the active lead species in aqueous solution as a function of pH. In aqueous solution at $\text{pH} < 10$, the main lead species were Pb^{2+} , PbOH^+ and $\text{Pb}_3(\text{OH})_4^{2+}$. Additionally, the anionic $\text{Pb}(\text{OH})_3^-$ was only found under alkaline conditions. They observed that $\text{Pb}(\text{OH})_2(\text{aq.})$ was the prevalent molecule at pH 10, but due to the low solubility constant of $\text{Pb}(\text{OH})_2(\text{s})$ it precipitated at high lead concentration (when the total lead concentration was greater than 20.72 mg/L) [2]. According to study conducted by Deng et al., the hydrolysis of Cu(II) to form $\text{Cu}_2(\text{OH})_2^{2+}$ and $\text{Cu}(\text{OH})^+$, $\text{Cu}(\text{OH})_2$, and $\text{Cu}(\text{OH})_3^{3-}$ species occurred in dilute solution with increasing pH from 8 to 12 when the total copper concentration was 100 mg/L). Additionally, $\text{Cu}(\text{OH})_4^{2-}$ was observed in the more alkaline solutions [231]. At pH 6.0, the predominant specie of lead and copper was Me^{2+} , followed by $\text{Me}(\text{OH})^+$ [2, 230]. The stable complexes might easily form between the metal cations/ hydroxyl metal cations and active surface sites. At pH 6.0-9.4, the available As(III) species were the combination of H_3AsO_3^0 and H_2AsO_3^- [229]. The negatively charged surface would not tend to attract the negatively charged As(III) ions, therefore the less favorable interactions were observed in the case of As(III) adsorption.

Besides the influence of concentrations of absorbate species and active sorbing sites on the sorption, the defined kinetic and adsorption modeling could be supportive evidence in order to comprehend the adsorption mechanism. Kinetic sorption analysis indicated that adsorption of Pb(II), Cu(II), and As(III) were better described by pseudo-second-order that assumes more than one binding pathway. Essentially, the adsorbed amount of

Pb(II) and Cu(II) increased through the basic pH values and this supported the formation of surface complexation rather than electrostatic interactions with surface sites [221]. In addition to that, from the calculated dimensionless separation factor (R_L) for Pb(II), the more irreversible adsorptions were observed and this could be the indication of chemical adsorption. In contrast, heterogeneity of the surface due to involvement of both strong and weaker binding sites for adsorption were favored for Cu(II) with a higher suitability to the Freundlich isotherm model [143]. Apart from that, according to the obtained ΔG values for Cu(II), the removal of adsorbate from solution with the nanoparticles was mainly governed by ion exchange mechanism rather than physical adsorption, and chemical adsorption might also contribute to the adsorption of Cu(II). In the case of As(III) adsorption, the uptake capacity was remain almost constant as the pH value was changed from 3.0 to 8.0 and the reason might be related to low affinity of the available As(III) species towards the active surface sites.

To further probe into the removal mechanisms of Pb(II), Cu(II), and As(III) by the anatase nanoadsorbent, XPS analyses on the nanoadsorbent were carried out after adsorptions of arsenic and heavy metals. The O1s narrow scans were illustrated in Figure 5.8. The spectra were divided into two peaks positioned at 530.0 and 531.3 eV, which could be assigned to metal oxide (M-O) and hydroxyl bonded to metal (M-OH), respectively [232]. After adsorption, it was found that the area ratio of the peak at 530.0 eV assigned to M-O increased due to the formation of Ti-O-R (R: functional groups), Pb-O, Cu-O or As-O groups on the anatase surface. On the other hand, the peak area ratio of the oxygen at 531.3 decreased after Pb(II), Cu(II), and As(III) adsorption, suggesting that hydroxyl groups created on the surface of anatase participated in the adsorption.

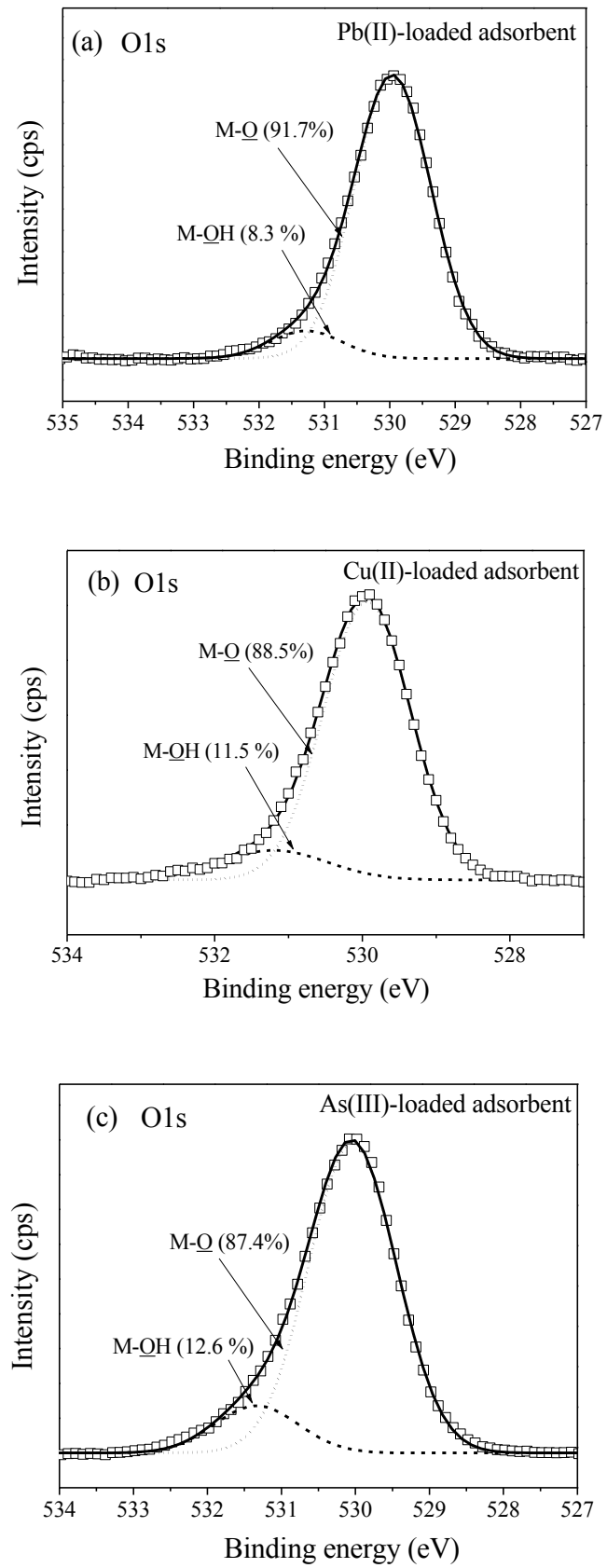


Figure 5.8. XPS spectra of O1s after (a) Pb(II), (b) Cu(II), (c) As(III) adsorption at pH 6.0.

Figure 5.9a illustrated the Pb4f spectrum of the adsorbent after Pb(II) adsorption, and the Pb4f_{7/2} and Pb4f_{5/2} binding energies of 138.8 eV and 143.6 eV were attributed to PbO₂ and PbO forms [2, 232], respectively. Figure 5.9b showed the XPS spectrum of Cu2p region. The XPS spectrum of Cu2p_{3/2} indicates that there are two components after deconvolution, attributed to Cu₂O (932.5eV) and CuO (934.3 eV) on the surface of anatase nanoadsorbent, respectively. Peaks at 941.3 and 943.8 eV were assigned to CuO satellites [233]. The As 3d spectrum of adsorbent after As(III) adsorption was shown in Figure 5.9c, and only one peak observed at 44.6 eV ascribing to As(III) species verified its successful binding to the adsorbent surface [233]. This result indicated that As(III) was not oxidized into As(V) during the sorption process. According to the XPS analysis, the metal oxide and hydroxyl groups on the anatase nanoadsorbent surface were responsible for Pb(II), Cu(II), and As(III) sorption. Those groups on the surface of nanoadsorbent could react with arsenic and heavy metals directly to form stable inner-sphere complexation and outer-sphere complexation through electrostatic binding reactions. Moreover, it was supposed that Pb(II), Cu(II), and As(III) could adsorb onto the nanoadsorbent by forming surface complexes of monodentate and bidentate.

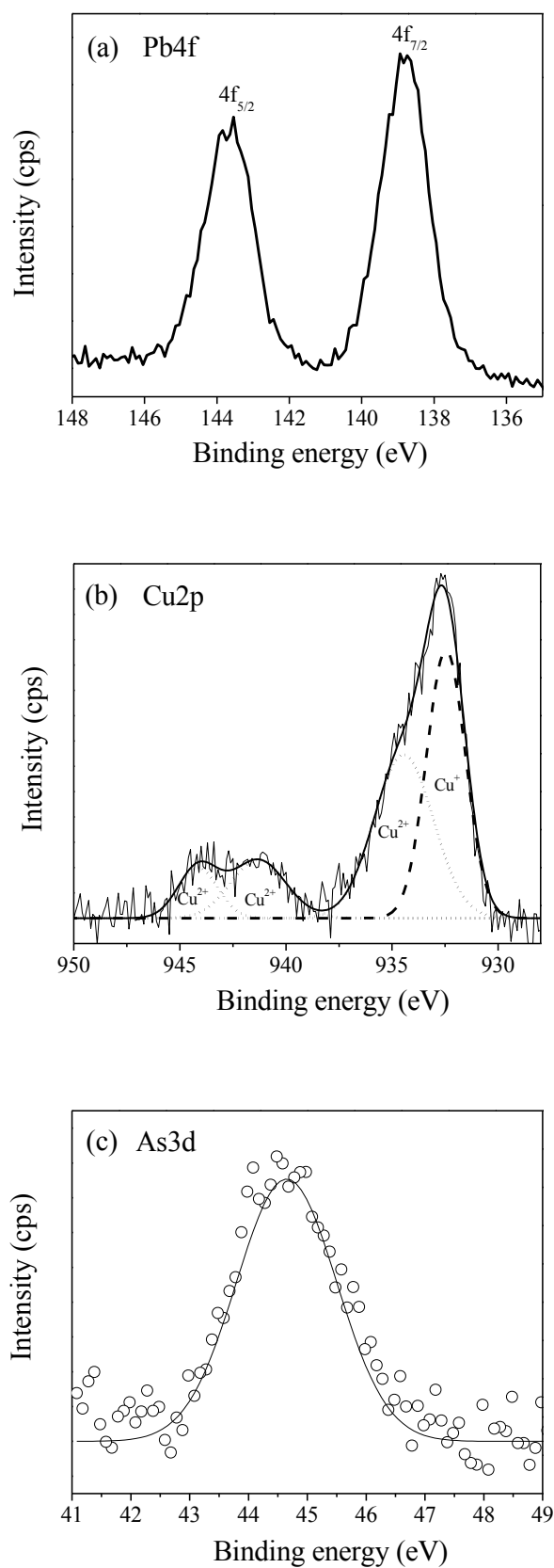


Figure 5.9. XPS (a) Pb 4f, (b) Cu 2p, (c) As 3d XPS core-level spectra on the anatase nanoadsorbent surface after adsorption at pH 6.0.

5.4. Concluding Remarks

The synthesized anatase nanoparticles indicated greater potential for the removal of Pb(II) and Cu(II) from drinking water. Additionally, the nanoparticles were able to reduce As(III) concentrations below the MCL requirements for drinking water up to moderate initial concentrations. The amount of Pb(II) and Cu(II) ions removed from water was strongly influenced by the pH and the type of reactive adsorbate species and active sites on the surface of adsorbent. In the case of As(III) adsorption, the uptake percentages were almost same upon entire pH value. Based on the R^2 and APE values, the pseudo-second-order model described the Pb(II), Cu(II), and As(III) adsorption kinetics. Langmuir model fitted well for Pb(II) uptake supported with lower APE and higher R^2 value, on the other hand the higher relationship between experimental and calculated adsorption data for Cu(II) and As(III) were observed in Freundlich isotherm model. Based on experimental data, the maximum adsorption capacity for Cu(II), Pb(II), and As(III) ions were 31.25 mg/g, 23.74 mg/g, and 16.95 mg/g respectively. Thermodynamic parameters indicated that the calculated ΔS values were positive and the favorable Gibbs energies were entropically controlled in the adsorptions of Pb(II) and Cu(II), while the As(III) adsorption was thermodynamically favorable without any limitations. XPS analyses revealed that the surface oxygen-containing functional groups including hydroxyl groups were involved in the adsorption process. Thus, the whole Pb(II), Cu(II), and As(III) sorption studies on the nanoparticles indicated that the synthesized nanoparticles can be effectively used in the treatment of water polluted with the arsenic and heavy metal ions.

CHAPTER 6.

A FACILE SYNTHESIS OF ACTIVATED CARBON/TITANIUM DIOXIDE NANOCOMPOSITES FOR ENHANCED AS(III) REMOVAL FROM WATER

6.1. Background

Water is one of the vital components for the continuity of life on earth. The existence of arsenic in water supplies poses the greatest risk to human health, due to its extreme toxicity and carcinogenicity [234]. Considering technical simplicity, applicability, and cost, adsorption is acquired a great importance in the removal of arsenic from water [74]. In natural water, inorganic arsenic generally exists in two predominant oxidation states, As(III) and As(V) and various studies have found that among the two species, As(III) is more toxic, mobile, and uncharged than the negatively charged As(V) species [207, 235]. The number adsorbents, which are extensively used for arsenic removal, include activated carbon, zeolite, ferric ion loaded red-mud, magnetite-doped activated carbon nanotubes, and graphene sheets [20, 22, 23, 207, 236, 237]. Titanium dioxide (TiO_2) is a widely used photocatalyst due to its strong oxidizing power and favorable band gap energy. It is effective in arsenic removal since it is capable of converting As(III) to less toxic and more adsorbable As(V) species under UV irradiation [213]. However, TiO_2 has suffered from continuously converting arsenic species under a visible light. Furthermore the difficulties in separation of small particles after adsorption have limited its wider industrial-scale operations [234, 238]. In order to address these challenges, nanoparticles can be embedded onto a support material. Embedding provides not only the prevention of release of metal oxide nanoparticles to the

environment but also the preservation of their reactivity [239, 240]. Activated carbon (AC) has been frequently used as the supporting material that enhances the applicability of metal oxide nanoparticles in the water treatment by adsorption [20, 241]. Moreover, introducing AC as a support material into TiO₂ not only allows visible light absorption but also provides trap sites within the TiO₂ bands by increasing the lifetime of photo-generated charge carriers [8].

Recently, some studies have recently emerged on the enhancement of sorption of arsenic species by combining metal oxide nanoparticles with carbonaceous materials [20, 234, 242-244]. The AC treatment provides a good cost-effective matrix for TiO₂ and by providing a pathway for the electron transfer simultaneously promotes more effective separation between photo-generated electrons and holes [245, 246]. However, no studies have focused on the As(III) adsorption properties of the TiO₂ nanoparticles are combined with various amount of AC. Therefore, in this chapter, AC/TiO₂ nanocomposites were fabricated successfully via a simple sol-gel method in order to enhance the removal of As(III) from water. The adsorption capabilities of AC, TiO₂, and AC/TiO₂ nanocomposites were evaluated in terms of contact time and pH.

6.2. Experimental

6.2.1. Synthesis of AC/TiO₂ Nanocomposites

The method used to prepare TiO₂ nanoparticles was described in detail in a previous study [187]. Briefly, titanium dioxide nanoparticles were synthesized by sol-gel method using titanium tetraisopropoxide (TTIP) (C₁₂H₂₈O₄Ti, Aldrich, 97%) as a metal organic precursor. TTIP (5 mL) was added to mixture of distilled water and 2-propanol (C₃H₈O, Merck, 99%). The gel preparation process was started when the pH of solution was adjusted to ~1 by the addition of 1 M HNO₃ under continuous stirring at 80°C. After the color of solution became transparent, a different amount of commercial activated carbon powder, which was used as a support material, was added to the solution. The nanocomposites synthesized with sol-gel method were denoted as x-AC/TiO₂, where x is 10, 20 and 40 present the weight percent of AC. The obtained solids were dried for

several hours at 100°C and annealed at 400°C for 2 h.

6.2.2. Characterization

Leo Supra 35VP field emission scanning electron microscope, Leo 32 and electron dispersive spectrometer software was used for imaging which was mostly done at 2-5 keV accelerating voltage, using the secondary electron imaging technique. X-ray diffraction (XRD) measurement was performed with a Brukeraxs advance powder diffractometer fitted with a Siemens X-ray gun and equipped with Brukeraxs Diffrac PLUS software. The sample was swept from $2\theta = 10^\circ$ through to 70° . The X-ray generator was set to 40kV at 40 mA. Raman spectrum was obtained from an InVia Reflex Raman microscope and spectrometer using a 532 nm diode laser excitation. Thermogravimetric analyses (TGA) were performed with a NETZSCH 449C thermogravimetric analyzer from room temperature to 1000°C at a heating rate of 10°C/min under air flow in a pure alumina crucible. Surface area was measured by Quantachrome NOVA 2200e series Surface Analyzer. The adsorption isotherms of nitrogen at 77 K were investigated using the Brunauer–Emmett–Teller (BET) method in the P/P_0 range of 0.05–0.3. All samples were outgassed for 24 h at 150°C. Total pore volume and pore diameter were calculated based on BJH (Brett–Joyner–Halenda) method and the desorption branch of isotherm.

6.2.3. Batch Adsorption and Desorption Experiments

A standard arsenic solution (1000 mg/L) was prepared by dissolving 1.320 g As(III) (As_2O_3 , 99.9%) in 10 mL 5% (w/v) NaOH and making up to 1 L with deionized water. Adsorption kinetics was studied by adding 0.025 g of adsorbent to 50 mL of As(III) solution with an initial As(III) concentration of 4 mg/L in a flask, the pH value was adjusted to 7.0 by adding HCl and NaOH solution, measurements of As(III) concentrations were performed different time intervals (5 minutes to 24 hours). Several initial As(III) concentrations ranging from 0.5 to 17 mg/L were used for equilibrium studies at fixed pH 7.0 for 12 h. The effect of pH on the adsorptions was studied by

using a prepared 5 mg/L of As(III) solution in a pH range of 3.0-10.0 at 25°C. At the end of each experiment the solution was separated from the solid adsorbent by using 0.45 µm PVDF membrane filter.

Five cycles of adsorption and desorption were carried out in order to analyze the reusability of the 10-AC/TiO₂. For the adsorption test, 0.5 g/L of adsorbent was added into a vessel containing 25 mg/L As(III) and the solution was stirred for 24 h and maintained at about pH 7.0, and then the adsorbent was separated from the solution and the solution was kept for the measurement of arsenic concentration. For the desorption test, four different eluents were studied: distilled water, HCl, HNO₃, and NaOH solution. For all these solutions, 50 mL of 1 M eluent solutions were separately mixed with 0.5 g/L adsorbent for 12 h and temperature of the system was arranged to 25 °C. For the adsorption-regeneration cycles, arsenic-containing adsorbent was added into a 50 mL of 1 M eluent solution. The mixture was stirred for 12 h and then regenerated adsorbent was separated from the solution. After washing and drying steps, it was used in the next adsorption–desorption cycle. As(III) concentrations of the solutions were measured with a Varian, Vista-Pro CCD simultaneous inductively coupled plasma ICP-OES spectrophotometer. Samples before and after adsorption experiments were analyzed to obtain residual As(III) concentrations. The experiments were carried in triplicate and average results were reported.

6.3. Results and Discussion

6.3.1. Characterization of AC/TiO₂

The SEM (Figure 6.1a) micrograph clearly indicated spherical morphology of TiO₂ nanoparticles. The images for AC/TiO₂ nanocomposites where the nanoparticles were located on the AC surface were illustrated in Figure 6.1b-d. Increasing the content of TiO₂ nanoparticles in the composites caused the agglomeration of larger amount of TiO₂ on the AC surface. The SEM image of AC, which was used in the nanocomposites, revealed layered structure with some pores illustrated in Figure 6.1e.

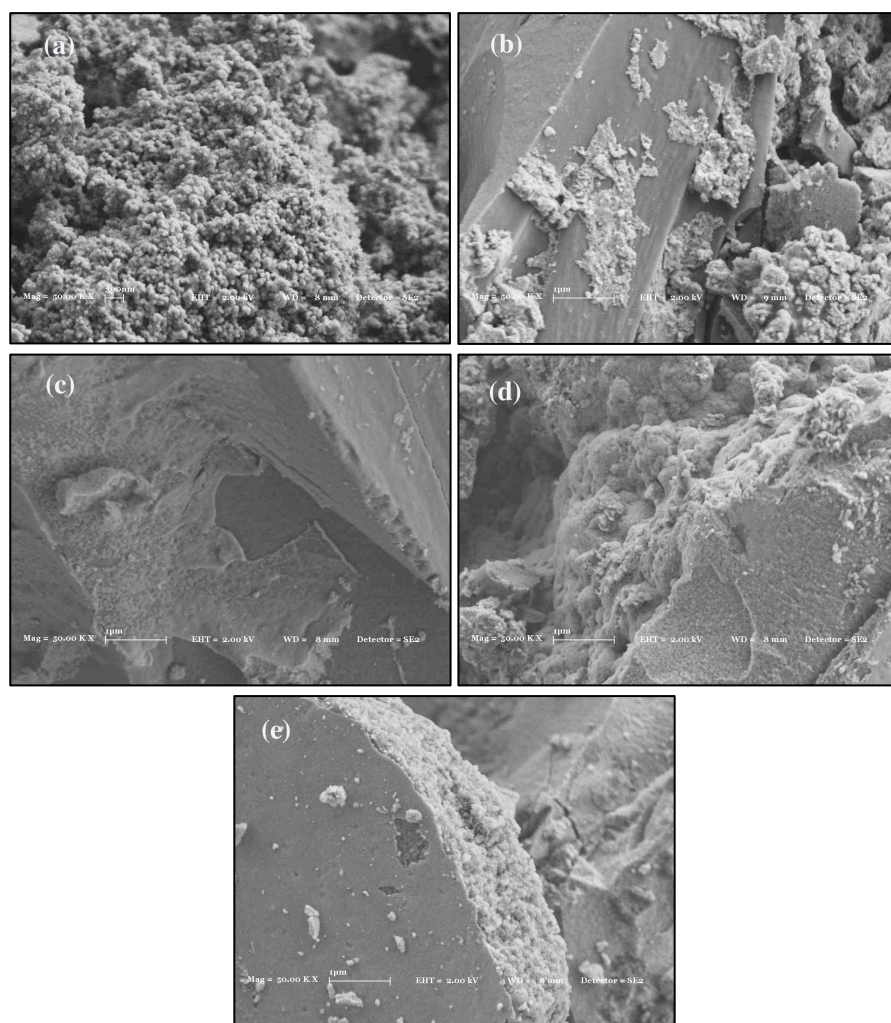


Figure 6.1. SEM images of TiO₂ (a), 40-AC/TiO₂ (b) 20-AC/TiO₂ (c), 10-AC/TiO₂ (d) and AC (e).

In Figure 6.2, XRD patterns of AC/TiO₂ nanocomposites, AC, and TiO₂ nanoparticles were illustrated. The characteristic diffraction peaks, which were indexed at 2θ of 25.6° (101) of the anatase phase of TiO₂, were clearly detected for TiO₂ nanoparticles and AC/TiO₂ nanocomposites [216]. No other irrelevant peaks were observed indicating the sample was pure in anatase phase. After the combination of TiO₂ with AC, XRD patterns were almost the same except there was some gradual decrease in the intensity of main peak with the decrease in TiO₂ content. Moreover, no crystalline peaks were detected for the AC because of its amorphous structure.

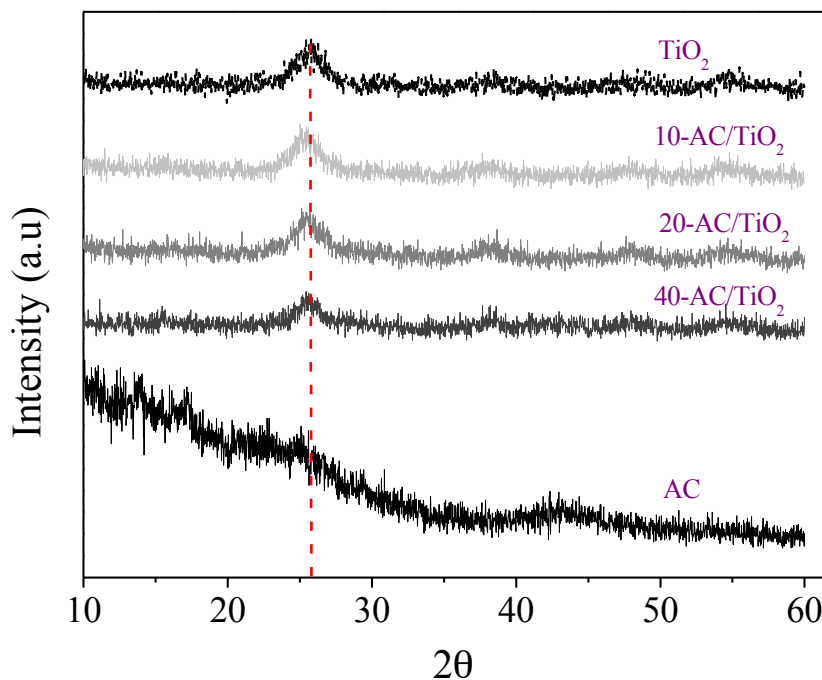


Figure 6.2. XRD patterns of the TiO₂, AC, and AC/TiO₂ nanocomposites

Raman spectroscopy provides a rapid way of obtaining the surface crystal structure of the TiO₂. The Raman spectra of AC, 10-AC/TiO₂ and 20-AC/TiO₂ nanocomposites, were shown in Figure 6.3. Two peaks approximately at 1348.3 and 1605.5 cm⁻¹ were attributed to the disordered structure and the graphite structure of activated carbon in the samples AC and AC/TiO₂ nanocomposites [247, 248]. In addition, the characteristic peaks of anatase were also found for AC/TiO₂ nanocomposites with the characteristic Raman lines giving evidence for the crystalline type of anatase rather than rutile and brookite. Anatase has six Raman active modes ($A_{1g} + 2B_{1g} + 3E_g$) and the Raman lines observed at 150.5 cm⁻¹, 398.0 cm⁻¹, 518.0 cm⁻¹, and 639.0 cm⁻¹ assigned to the E_g, B_{1g}, A_{1g}, and E_g vibrational modes of anatase, respectively [217, 249].

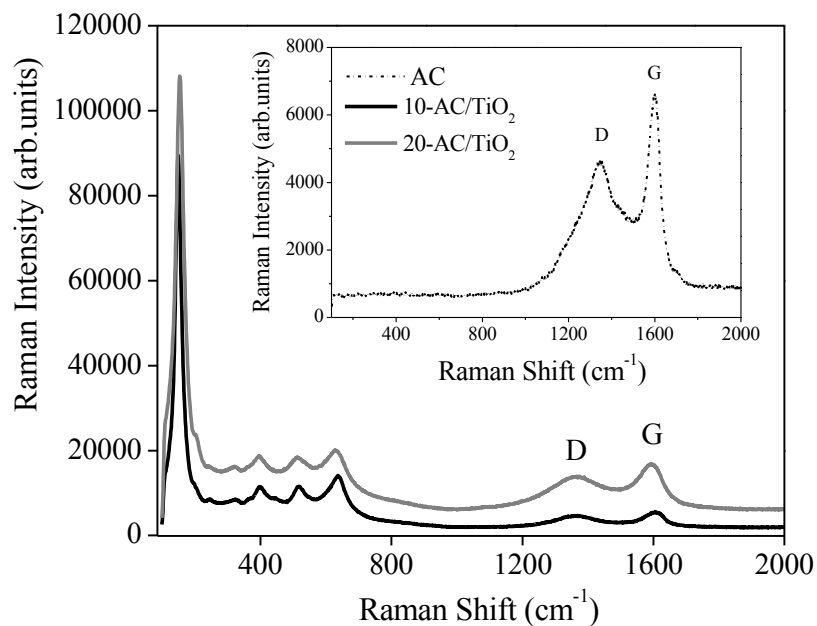


Figure 6.3. Raman spectra of AC, 10-AC/TiO₂, 20-AC/TiO₂

The TGA curves for the AC, TiO₂ nanoparticles, AC/TiO₂ nanocomposites were shown in Figure 6.4. AC was stable up to 400°C. However, the presence of TiO₂ nanoparticles in the system led to a weight loss at an earlier stage approximately at 100°C for AC/TiO₂ nanocomposites. The TiO₂ and nanocomposite samples demonstrated two main weight losses. The first rapid weight losses were observed from 100 to 150°C mainly corresponded to the removal of the adsorbed water and the dehydration of hydroxyls on the surface TiO₂ [250]. As the temperature was further increased, the second weight loss appeared in the range of 200–400 °C, which was mainly due to decomposition of some oxygen containing groups. The weight loss at 1000°C provided comparable information about the content of TiO₂ in the nanocomposites. The residual weights for AC, TiO₂ nanoparticles and 10-AC/TiO₂ nanocomposites were achieved at 860°C, 400°C and 650°C, respectively.

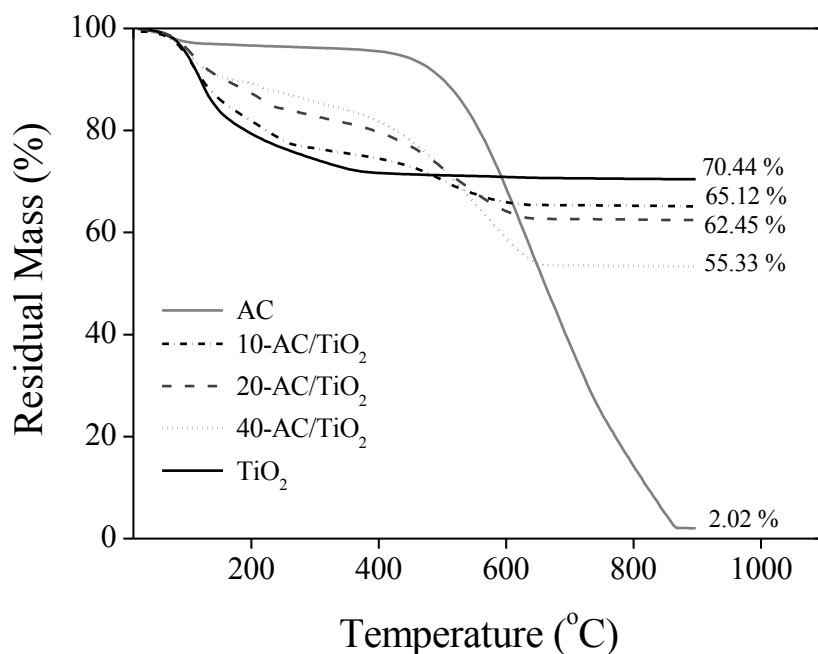


Figure 6.4. TGA curves of the TiO₂, AC, and AC/TiO₂ nanocomposites

The nitrogen adsorption/desorption isotherms of AC/TiO₂ nanocomposites and AC were illustrated Figure 6.5. Typical type IV hysteresis that is often associated with narrow slit-like pores for distinctive mesoporosity [251], was observed in all of the samples. In addition to that, there was an inverse proportion between the amounts of AC content in nanocomposites and surface area. The BET surface area of 10-AC/TiO₂ nanocomposite was 176.81 m²/g, decreased by approximately 86% when compared to 1252.84 m²/g of AC support. The reason for this dramatic decrease in the surface areas could be associated with aggregation of TiO₂ nanoparticles on the external surface and inside the pores of AC. The porosity parameters, which were calculated from desorption isotherms by BJH model of the samples, were summarized in Table 6.1. The reductions in pore volumes as increasing the TiO₂ nanoparticles content were attributed to agglomeration of the nanoparticles on the AC surface by blocking the most of the pore entrance and effect of calcinations at 400°C to stimulate the formation of anatase TiO₂ [252].

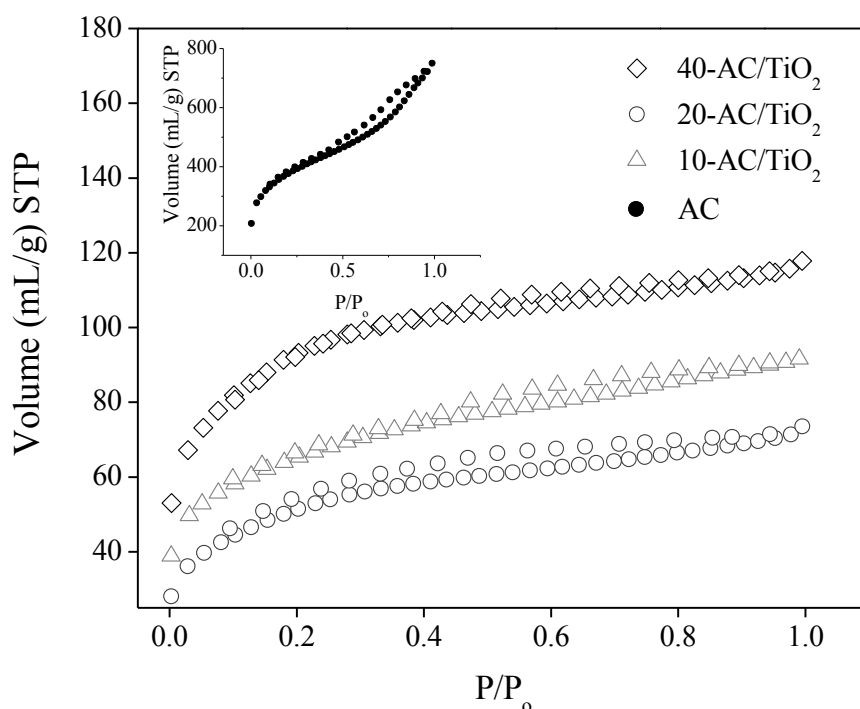


Figure 6.5. Nitrogen adsorption/desorption isotherms of AC and AC/TiO₂ nanocomposites.

Table 6.1. Structural characteristic parameters of AC and AC/TiO₂.

Adsorbent	BET surface area (m ² /g)	Pore volume (mL/g)	Pore diameter (Å)
AC	1252.84	0.90	16.97
40-AC/TiO ₂	306.40	0.11	16.77
20-AC/TiO ₂	217.84	0.09	16.76
10-AC/TiO ₂	176.81	0.08	16.69

6.3.2. Sorption Kinetics of the AC/TiO₂ Nanocomposites

The sorption of As(III) on the AC, TiO₂ nanoparticles, and AC/TiO₂ nanocomposites as a function of contact time are shown in Figure 6.6. Clearly, the combination of TiO₂ nanoparticles with AC significantly enhanced the As(III) uptake. It could be seen that the As(III) adsorption by 10-AC/TiO₂ nanocomposite occurred very quickly reaching adsorption equilibrium after 5 minutes. The fast adsorption trend at initial stage is

frequently observed phenomenon in the removal of contaminants from water and it is most likely caused by reactive chemical groups readily presented on the surface [221]. On the other hand, there was a gradual increase in the As(III) adsorption by 20-AC/TiO₂ and 40-AC/TiO₂ nanocomposites, and TiO₂ nanoparticles when contact time was increased from 5 to 240 min and the maximum As(III) uptake was obtained after 480 minutes of contact. Therefore, a contact time of 480 minutes was selected for all batch adsorption experiments in order to ensure that equilibrium was established in each case. Moreover, due to the apparent lack of adsorption behavior, AC was found to be unsuitable to remove As(III) ions from water.

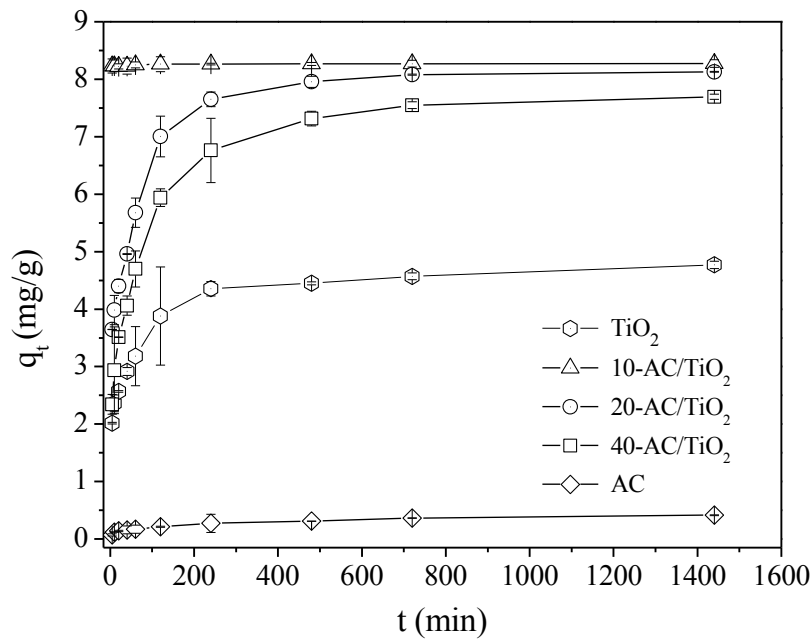


Figure 6.6. Effect of contact time for As(III) adsorption onto TiO₂, AC, and AC/TiO₂ nanocomposites [Temperature = 25°C, pH = 7.0, S:L = 500 mg/L].

To investigate the adsorption kinetics for the sorption processes, four kinetic models were studied by applying the experimental sorption data to the pseudo-first-order (Equation 6.1) [122], the pseudo-second-order equation (Equation 6.2) [189]. The linear mathematical forms of kinetics equations used are shown below:

$$\log(q_e - q_t) = \log(q_e) - \frac{k_1}{2.303} t \quad (6.1)$$

$$\frac{t}{q_t} = \frac{1}{k_2 q_e^2} + \frac{t}{q_e} \quad (6.2)$$

The initial adsorption rate h (mg/g.min) can be defined as:

$$h = k_2 q_e^2 \quad (6.3)$$

where, q_t is the amount of adsorbed contaminant (mg/g) at time t , q_e is the maximum adsorption capacity (mg/g) for the pseudo first order adsorption and pseudo second order adsorption, k_1 is the pseudo first order rate constant for the adsorption process (1/min) and k_2 is the pseudo second order rate constant (g/mg.min). The sorption modeling parameters and the correlation coefficients (R^2) values were summarized in Table 6.2. R^2 values for pseudo-second order model were much higher than that of pseudo-first order model. Moreover, the experimental adsorption capacity (q_{exp}) values were particularly close to the calculated adsorption capacity (q_{cal}) values for pseudo-second order model, signifying that the pseudo-second order kinetic model well described the kinetics of As(III) adsorption. Good agreements with the pseudo-second-order model suggest that chemical adsorption was the rate-limiting step [189] and the adsorption rates were proportional to the square of the number of sites on the adsorbent surface. Additionally, the k_2 value calculated for 10-AC/TiO₂ was higher than that for 20-AC/TiO₂, 40-AC/TiO₂, and TiO₂, indicating faster As(III) adsorption rate of 10-AC/TiO₂ as can be seen in Table 6.2.

Table 6.2. The kinetic sorption modeling parameters for As(III) adsorption.

Model	Parameters	TiO ₂	10-AC/TiO ₂	20-AC/TiO ₂	40-AC/TiO ₂
Pseudo First Order	k_1 (1/min)	0.010	0.002	4.950	0.004
	q_{e1} (mg/g)	2.399	0.042	3.851	4.255
	R^2	0.990	0.775	0.995	0.973
Pseudo Second Order	k_2 (g/mg.min)	0.028	0.635	0.006	0.004
	q_{e2} (mg/g)	3.637	8.271	8.237	7.836
	R^2	0.994	0.999	0.998	0.999
	h (mg/g.min)	0.376	43.44	0.465	0.266

In order to obtain more information about the adsorption mechanism and rate controlling steps that affects the kinetics of adsorption, the intraparticle diffusion model (Equation 6.4)), which was proposed by Weber and Morris, was applied [127];

$$q_t = k_{int}t^{0.5} + A \quad (6.4)$$

where k_{int} ($\text{mg}/(\text{g min}^{0.5})$) is the internal diffusion rate constant and A , which is obtained from the intercept of the linear plot of q_t versus $t^{0.5}$, gives information about thickness of the boundary layer. As could be seen in Figure 6.7, two straight lines were obtained from the experimental data. The first portion was related external diffusion, which concerns the diffusion of adsorbate through the solution to the external surface of the adsorbent. The second portion corresponded with intraparticle diffusion, which is also entitled with the slow adsorption stage correlated with the diffusion of the adsorbate species inside the adsorbent [253]. The modeling results for the two portions of kinetic data are shown in Table 6.3. It is obvious that k_{p1} was higher than k_{p2} for all four adsorbents. This indicated that the rate of As(III) removal was higher in the beginning since more reactive sorption sites on the adsorbents were available at initial time for the adsorption. Besides, the larger value of A_2 was attributed to the greater boundary-layer effect at the second portion [254].

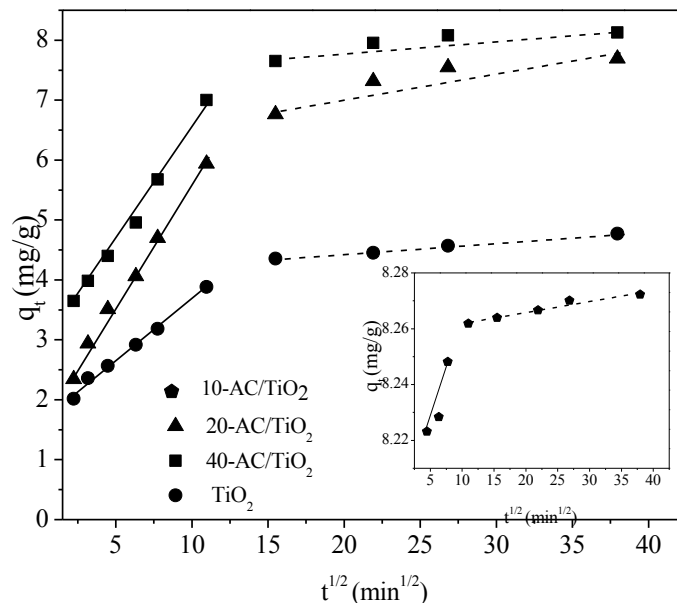


Figure 6.7. Intraparticle diffusion model for the As(III) adsorption onto the TiO₂ and AC/TiO₂ nanocomposites.

The intraparticle diffusion can be considered as the rate-determining step, if the linearized curve passes through the origin (0, 0). Although, the obtained R^2 values were comparably high with the pseudo-second-order model for all four adsorbents, the results of fitting did not pass through the origin (0, 0) interpreting that the adsorption mechanism of As(III) removal on to the adsorbents was complex. The intraparticle diffusion or ion exchange mechanism may also control the rate of adsorption apart from the surface adsorption [255].

Table 6.3. Parameters of intraparticle diffusion model for As(III) adsorption.

Adsorbent	k_{p1} (mg/g.min ^{1/2})	k_{p2} (mg/g.min ^{1/2})	A_1	A_2	R_1^2	R_2^2
TiO ₂	0.176	0.002	1.768	4.423	0.981	0.919
10-AC/TiO ₂	0.007	0.001	8.187	8.257	0.847	0.991
20-AC/TiO ₂	0.383	0.019	2.218	7.444	0.994	0.835
40-AC/TiO ₂	0.399	0.039	1.596	6.329	0.994	0.821

6.3.3. Adsorption Capacity

Adsorption isotherm models are commonly used to describe the adsorption and its mechanisms. To understand the adsorption patterns, Langmuir, Freundlich, Redlich-Peterson, and Temkin, isotherm models were investigated by using the adsorption equilibrium data of As(III) onto TiO₂ and AC/TiO₂ nanocomposites [130, 181, 226, 256].

Langmuir model [130] assumes that a single specie of the sorbate adsorbs on specific homogenous adsorption sites within the sorbent by forming monolayer coverage and can be represented by the following equation:

$$q_e = \frac{q_{mon} b C_e}{1 + b C_e} \quad (6.5)$$

where q_e is the solute amount adsorbed per unit weight of adsorbent (mg/g), C_e is liquid phase sorbate concentration in equilibrium, q_{mon} is the monolayer adsorption capacity (mg/g) and b is the adsorption equilibrium constant (L/mg) related to adsorption enthalpy ($b = \exp(-\Delta H/RT)$). From the adsorption equilibrium constant in Langmuir model, the dimensionless separation factor (R_L), which was the indicative of the isotherm shape, could be obtained by using the following equation:

$$R_L = \frac{1}{1 + b C_o} \quad (6.6)$$

where, C_o is the initial adsorbate concentration (mg/L). The value of R_L demonstrates the nature of adsorption as unfavorable ($R_L > 1$), linear ($R_L = 1$), favorable ($0 < R_L < 1$) and irreversible ($R_L = 0$) [187].

Freundlich model [181] is derived considering a theory of the heterogeneous adsorption sites and interactions by assuming a heterogeneous surface and it can be described as follows:

$$q_e = K_F C_e^{1/n} \quad (6.7)$$

where K_F indicates the adsorbent's relative adsorption capacity (mg/g), $1/n$ is the constant representing adsorption intensity. If the value of $1/n$ is lower than 1, it indicates a normal Langmuir isotherm; otherwise, it is indicative of cooperative adsorption.

The Redlich-Peterson isotherm model, [226] which includes features of both the Langmuir and Freundlich equations, can be described as follows:

$$q_e = \frac{K_{RP} C_e}{1 + a_{RP} C_e^{\beta_{RP}}} \quad (6.8)$$

where K_{RP} is Redlich-Peterson isotherm constant (L/g), a_{RP} is Redlich-Peterson isotherm constant (L/mg) $^{\beta_{RP}}$ and β_{RP} is the exponent which lies between 0 and 1. The β_{RP} parameter (dimensionless) represents the heterogeneity of the binding surface. If β_{RP}

tends to unity Redlich–Peterson model results in Langmuir model.

The Temkin isotherm model's [256] assumption that the heat of adsorption decreases linearly with adsorbate coverage ascribes to some indirect adsorbate–adsorbent interactions. The Temkin isotherm can be described in the following form:

$$q_e = B \ln(K_T C_e) \quad (6.9)$$

where, B ($B = RT/b$) is a constant related to heat of adsorption (J/mol), R is the universal gas constant (8.314 J/mol), and K_T is the Temkin isotherm constant (L/mg).

The nonlinear adsorption isotherms were illustrated in Figure 6.8. The maximum adsorption capacities were found as 9.79 mg/g for TiO₂, 14.12 mg/g for 40-AC/TiO₂, 18.45 mg/g for 20-AC/TiO₂ and 26.62 mg/g for 10-AC/TiO₂. The incorporation of TiO₂ with AC indicated higher As(III) uptakes at all initial sorbate concentrations than do bare TiO₂ nanoparticles. The optimum uptake of As(III) was achieved at 10-AC/TiO₂. AC probably enhanced the adsorption by creating additional adsorption sites on the nanocomposites [257].

The isotherm constants and correlation coefficients (R^2) were summarized in Table 6.4. The correlation coefficients for the Langmuir isotherm were the highest in comparison to the values obtained for the Freundlich, Temkin, and Redlich-Peterson isotherms. Therefore, the Langmuir isotherm was the best-fit isotherm for the adsorption of As(III) onto TiO₂ nanoparticles, and AC/TiO₂ nanocomposites indicating specific homogenous adsorption sites within the sorbent by forming monolayer coverage. Additionally, the suitability of Langmuir isotherm model to the As(III) sorption data were also supported by the obtained dimensionless parameter value in Redlich-Peterson, which was also close to unity for AC/TiO₂ nanocomposites. Moreover, from the calculated dimensionless separation factor (R_L) were found to be 0.96 to 0.39 for TiO₂, 0.29 to 0.01 for 10-AC/TiO₂, 0.64 to 0.05 for 20-AC/TiO₂, and 0.66 to 0.06 for 40-AC/TiO₂ respectively, indicating more irreversible As(III) adsorptions onto the nanocomposites with the increase of initial sorbate concentration.

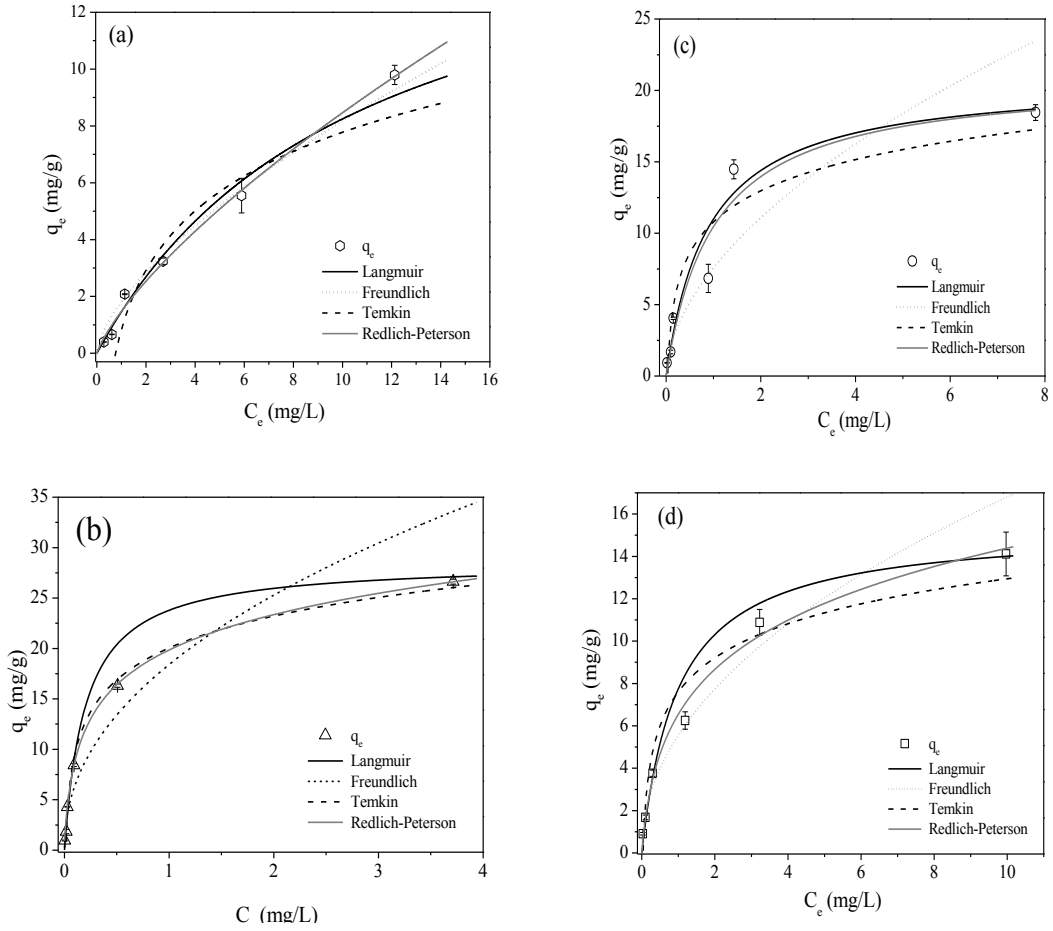


Figure 6.8. Adsorption isotherm of As(III) onto TiO_2 (a), $10\text{-AC}/\text{TiO}_2$ (b) $20\text{-AC}/\text{TiO}_2$ (c), $40\text{-AC}/\text{TiO}_2$ (d) [Initial concentration = 0.5–17 mg/L, Temperature = 25°C, pH = 7.0, S:L = 500 mg/L].

Table 6.4. Sorption isotherm parameters for As(III) removal onto TiO₂ and AC/TiO₂.

Isotherm Parameters	TiO ₂	10-AC/TiO ₂	20-AC/TiO ₂	40-AC/TiO ₂
q_{exp}(mg/g)	9.797	26.62	18.45	14.12
Langmuir				
q _{mon} (mg/g)	17.54	28.57	20.83	15.38
b (L/mg)	0.094	4.971	1.116	1.015
R ²	0.856	0.999	0.975	0.998
Freundlich				
K _F (mg/g)	1.809	18.41	7.568	5.551
1/n	0.658	0.458	0.551	0.481
R ²	0.991	0.907	0.877	0.982
Temkin				
K _T	<i>1.315</i>	<i>81.04</i>	<i>30.73</i>	<i>26.59</i>
B	3.188	4.562	3.15	2.318
R ²	0.909	0.996	0.875	0.938
Redlich-Peterson				
K _{RP} (L/g)	3.821	211.7	20.83	23.53
a _{RP} (L/mg) ^{β_{RP}}	1.586	8.928	0.992	2.593
β _{RP}	0.346	0.886	0.987	0.772
R ²	0.966	0.998	0.974	0.996

6.3.4. Effect of pH on Adsorption

The pH is a significant parameter for determining the adsorption between the adsorbent and aqueous interface. The relationship between the removal of As(III) in the variation of initial pH 3.0–10.0 was presented for TiO₂ nanoparticles, AC, and the nanocomposites of AC/TiO₂ in Figure 6.9a. 98.2% of As(III) removal was obtained with the 10-AC/TiO₂ nanocomposite at pH 7.0. Combining AC with TiO₂ may increase the oxidation of As(III) to As(V) under visible light [8] and higher amounts of arsenic species were removed from water. However the increase in the AC weight percent in

the nanocomposite led to a decrease in adsorption performance due to lack of sufficient TiO_2 active sites.

The ionic character of the arsenic species varies with pH as the predominant As(III) species available are the H_3AsO_3 and H_2AsO_3^- in the pH range of 4.0-9.5 [207]. The AC/ TiO_2 nanocomposites were most effectively adsorbed As(III) at pH 7.0. One likely reason for the observed result is that at pH 7.0 H_3AsO_4 was mostly found in the aqueous solution and those neutral As(III) species formed complex with surface groups especially at pH in the range of 6.15-8.0 [112]. Apart from that, with the increase in pH value, H_3AsO_4 species is drastically reduced and anionic As(III) species such as H_3AsO_3^- and $\text{H}_3\text{AsO}_3^{2-}$ are dominant at pH 9.0 [207]. This observation explained the decrease in the adsorption of As(III) on to the adsorbents.

Variations of pH_{Final} against $\text{pH}_{\text{Initial}}$ of batch experiments for As(III) sorption are illustrated Figure 6.9b. During the adsorption process of As(III), it has been seen that the solution pH_{Final} was greater than the $\text{pH}_{\text{Initial}}$ in the range of 3.0–8.0. This was likely due to the uptake of H^+ ions by the adsorbent surface at $\text{pH}_{\text{Initial}}$ ranging from 3.0 to 8.0. However, after that, the pH_{Final} of the solution was decreased during sorption of As(III).

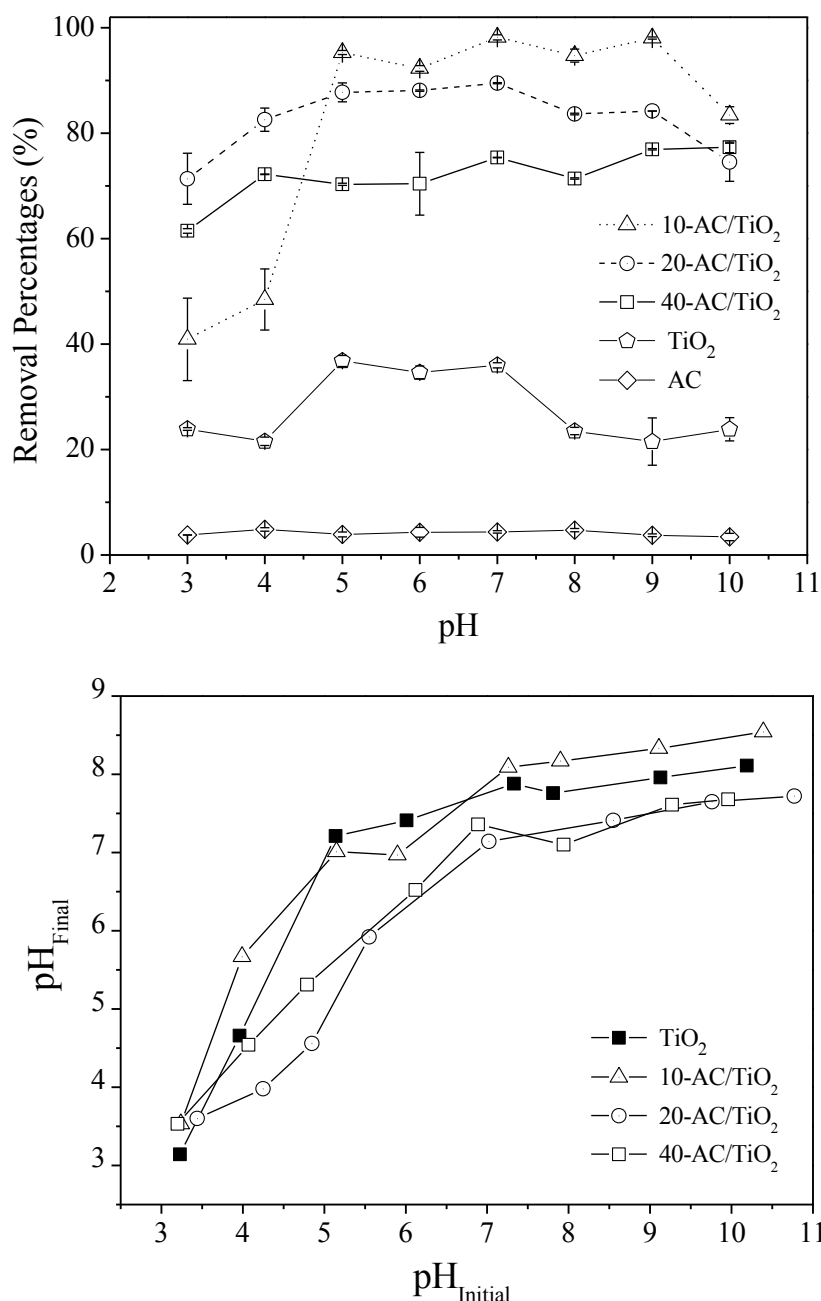


Figure 6.9. Adsorption of 5 mg/L As(III) as a function of pH by 500 mg/L adsorbent materials 25 °C **(a)** and pH_{final} versus pH_{initial} during the adsorption **(b)**.

6.3.5. Regeneration of AC/TiO₂

In order to evaluate the reusability of the fabricated 10-AC/TiO₂, regeneration adsorption capacity of the nanocomposite for As(III) was studied. To select the optimal desorption solution, three different eluents were studied: distilled water, HCl, HNO₃,

and NaOH solutions. Experimental results are depicted in Figure 6.10 in terms of the desorption efficiency achieved with the different eluting solutions, and indicate that the optimal solutions for arsenic desorption were those containing HNO₃ or HCl.

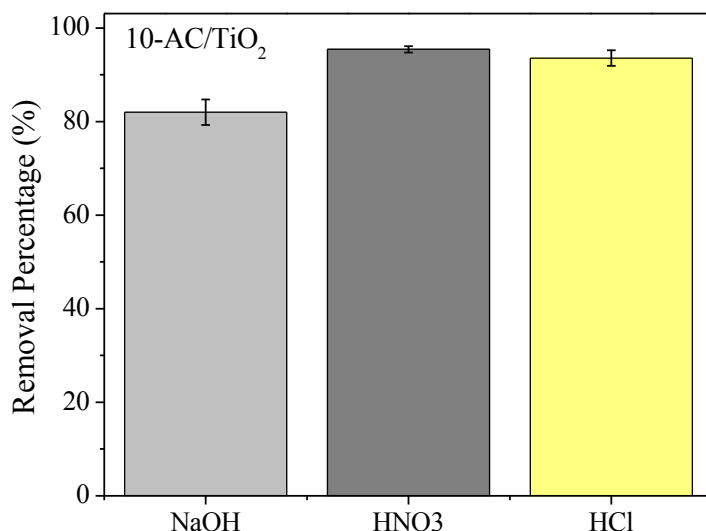


Figure 6.10. Desorption capacity of 10-AC/TiO₂ nanocomposite for As(III) with the different eluting solutions

The adsorption–regeneration cycles were carried out up to five times by using HNO₃ which provided better desorption media for As(III). The results obtained are shown in Figure 6.11. It was observed that the removal efficiency gradually decreased with the increase of in cycle number. However, the removal efficiency after five cycles was of 82%, demonstrates that it could be used as an effective material for many cycles by regeneration.

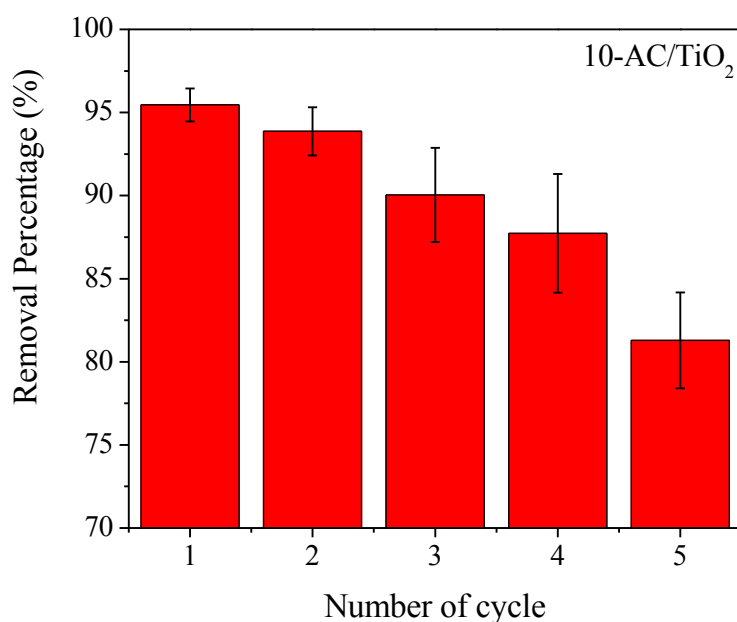


Figure 6.11. Regeneration of 10-AC/TiO₂ nanocomposite for As(III) with the increase of cycle number

6.4. Concluding Remarks

In the present chapter, AC/TiO₂ nanocomposites were fabricated by introducing different amounts of AC in the system. According to the results obtained from SEM and BET, TiO₂ nanoparticles were inserted into the external surface and inside the pores of AC and the surface area of the nanocomposites increased with the higher amount of AC. TGA results show that AC was stable up to 400°C, however, presence of TiO₂ nanoparticles in the system led to weight loss at an earlier stage approximately at 100°C. Moreover, the better adsorption capacity for As(III) which the AC/TiO₂ composites exhibited is 2.7 times greater than that of bare TiO₂. The maximum As(III) removal was found at 26.62 mg/L for the 10-AC/TiO₂ nanocomposite at pH 7.0. However, increasing the amount of AC in the composite system led to decline in the adsorption. The 10-AC/TiO₂ nanocomposite has a potential application for arsenic removal in water treatment due to its high As(III) adsorption –desorption capabilities.

CHAPTER 7.

ARSENIC REMOVAL FROM WATER BY TiO₂ NANOPARTICLES THROUGH SIMULTANEOUS PHOTOCATALYTIC OXIDATION AND ADSORPTION

7.1. Background

Arsenic commonly presented in natural water as As(III) and As(V) oxyanions, arsenite (AsO_2^-) and arsenate (AsO_4^{3-}) [258] cause to severe health problems. Specifically As(III) has higher toxicity and mobility in natural waters compare to As(V). Recent reports also indicate that up to 67–99% of total arsenic in groundwater includes As(III) species [259, 260]. In order to achieve higher total arsenic removal, arsenic treatment techniques including coagulation/precipitation, ion exchange, membrane/reverse osmosis, biological treatment and adsorption, require a preoxidation step in order to convert arsenite to arsenate. Some of the widely studied oxidation technologies are the injection of oxygen and/or ozone [68], photocatalytic oxidation [261], biological oxidation [262], and electro-oxidation [263]. Kim and Nriagu [68] demonstrated that arsenic in groundwater samples were converted to As(III) in the presence of ozone, air and pure oxygen. In an another study, it was shown that the oxidation of As(III) is also possible in the presence of hypochlorite and potassium permanganate [264]. Although conversion can be achieved by oxidants such as hydrogen peroxide, oxygen, ozone, manganese oxides and chlorine [70], the rate of As(III) oxidation was slow and larger

amount of those chemical oxidants were needed to treat water contaminated with high concentration of arsenite [265].

Titanium dioxide is a very well studied material with a wide range of applications [87]. One reason that makes this material so important is its ability to act as a photocatalyst. Anatase form has band gap energy (E_g) of 3.2 eV. An efficient promotion of an electron from the valence band to the conduction band is observed upon irradiation with UV radiation. This results in the formation of an electron-hole pair [266]. These reactive species then participate in oxidation and reduction processes, either within the TiO_2 itself (electron and hole recombination), or with adsorbates at the surface. The major reactive intermediate species in this reaction is the hydroxyl radical, produced by redox reactions between photo-excited TiO_2 and adsorbed water molecules [267]. According to the study conducted by Zhang, a concentration of 100 mg/L arsenite could be entirely oxidized to arsenate within 3 h in the presence of slag-iron oxide- TiO_2 with UV-light irradiation [265]. Yu reported that Fe-Ti binary oxide magnetic nanoparticles which combined the photocatalytic oxidation property of TiO_2 , can be efficiently oxidized As(III) to As(V) by dissolved O_2 in $\alpha\text{-Fe}_2\text{O}_3\text{-TiO}_2$ nanoparticle suspensions under UV light [261].

In this chapter, the TiO_2 nanoparticles, which were fabricated through a facile sol-gel route, were used for photocatalytic removal of arsenic from aqueous solution. The experimental study evaluated the efficiencies of both As(III) and As(V) removal from water by adsorption process under visible light. The removal capacities of TiO_2 nanoparticles were also compared with the presence of UV-light illumination. Adsorption behavior considering contact time, pH and sorption capacity was investigated in detail for As(III) and As(V).

7.2. Experimental

7.2.1. Synthesis of TiO₂ Nanoparticles

Sol gel method was used in order to prepare TiO₂ nanoparticles. 25 mL of titanium tetraisopropoxide (TTIP) (C₁₂H₂₈O₄Ti, Aldrich, 97%) metal organic precursor solution was mixed with 2-propanol (C₃H₈O, Merck, 99%) and distilled water. The pH of solution was adjusted to ~ 2 by the addition of 1 M HCl under continuous stirring at room temperature. The blue-yellowish gel was achieved after 30 minutes of mixing. The obtained gel was washed with anhydrous ethyl alcohol (C₂H₅O, Aldrich, 99.5%) and dried for several hours at 100 °C. The sample was smashed into fine powder and calcinated for 2 h at 400 °C to achieve the desired nanoparticles.

7.2.2. Adsorption and photocatalytic oxidation experiments

A standard As(III) solution containing (100 mg/L) was prepared by dissolving 0.1332 g As₂O₃ in 10 mL 1% (w/v) NaOH and making up to 1 L with deionized water. A stock solution of As(V) (100 mg/L) was obtained by dissolving 0.4164 g Na₂HAsO₄·7H₂O in 1 L of deionized water. The effect of pH on the adsorptions were studied by using prepared 4.5 mg/L of As(III) and As(V) solutions in a pH range of 2.0-10.0 at 25°C for 24 h. Adsorption kinetics was studied with addition 0.025 g of adsorbent to 50 mL of arsenic solution with an initial adsorbate concentration of 4 mg/L in a flask, the pH value was adjusted to 7.0 for As(III) and 3.0 for As(V) by adding HCl and NaOH solution, measurements of adsorbate concentrations were investigated different time intervals (5 minutes to 24 hours). The initial arsenic concentrations ranging from 1 to 25 mg/L were used for equilibrium studies at fixed pH 7.0 for As(III) and 3.0 for As(V). At the end of each experiment the solution was separated from the solid adsorbent by using 0.45 µm PVDF membrane filter.

The As(III) photocatalytic oxidation experiments were carried out inside a 60 cm x 60 cm x 45 cm stainless black box with a door in one side for sampling. A UV- A lamp

($300 < \lambda < 400$ nm) was used as the UV irradiation source. The photocatalytic oxidation experiments were conducted using a glass vessel, which was filled with 120 mL of As(III) solution (4 mg/L) and 0.5 g/L TiO₂ nanoparticles. Inside the stainless black box, the UV irradiation source was positioned at the center within a glass vessel. The distance between UV-A lamp and glass solution surface was 1.25 cm. The entire system was kept open to the atmosphere in all photocatalytic oxidation experiments. A magnetic stirrer was used to ensure that the solution was continuously stirred at a constant speed. At regular intervals, around 10 mL of the sample was taken out of the reactor, filtered using 0.45 μ m disposable PVDF membrane filter.

7.2.3. Characterization

Leo Supra 35VP field emission scanning electron microscope, Leo 32 and electron dispersive spectrometer software was used for images and analysis. Imaging was mostly performed at 2-5 keV accelerating voltage, using the secondary electron imaging technique. X-ray diffraction (XRD) measurement was done with a Brukeraxs advance powder diffractometer fitted with a Siemens X-ray gun and equipped with Brukeraxs Diffrac PLUS software. The sample was swept from $2\theta = 10^\circ$ through to 70° . The X-ray generator was set to 40kV at 40 mA. Arsenic concentrations of the solutions were measured with a Varian, Vista-Pro CCD simultaneous inductively coupled plasma ICP-OES spectrophotometer. Samples before and after adsorption experiments were analyzed to obtain residual arsenic concentration. In order to test the reproducibility, the experiments were carried in triplicate and average results were reported.

7.3. Results and Discussion

7.3.1. Crystal structure and morphology of TiO₂ Nanoparticles

XRD spectra of synthesized TiO₂ nanoparticles (Figure 7.1a) demonstrated the presence of the main peaks at 2θ values of 25.4° (101), 37.8° and 48.1° that are matched with the commercial anatase particles. The characteristic peaks corresponding to the rutile phase of TiO₂ at 2θ values of 27.5° (110), 30.8° and 36.4° were absent in the XRD spectra [268]. The average size of the anatase crystallite was calculated by applying the Debye-Scherrer formula (Equation 7.1) [269] to the main anatase (101) peak in XRD spectrum and the average crystallite size was found to be 9.02 nm.

$$D_{XRD} = \frac{0.9\lambda}{\beta \cos \theta_B} \quad (7.1)$$

where λ is the average wavelength of the X-ray radiation, β is the full width at half-maximum peak position, and θ is the diffracting angle.

SEM image of synthesized TiO₂ nanoparticles was shown in Figure 7.1b and Figure 7.1c. At lower magnification, the bigger TiO₂ particles were observed due to the agglomeration, which is a general phenomenon observed in nanoparticle synthesis [270]. At higher magnification, it was observed that the nanoparticles interpreted a well-ordered texture with heterogeneous particle size in the range of 10 to 150 nm starting from the interfaces of the contacting anatase grains.

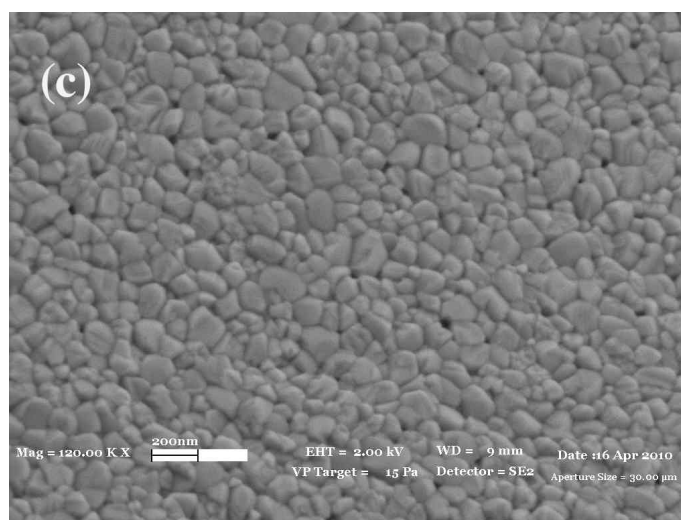
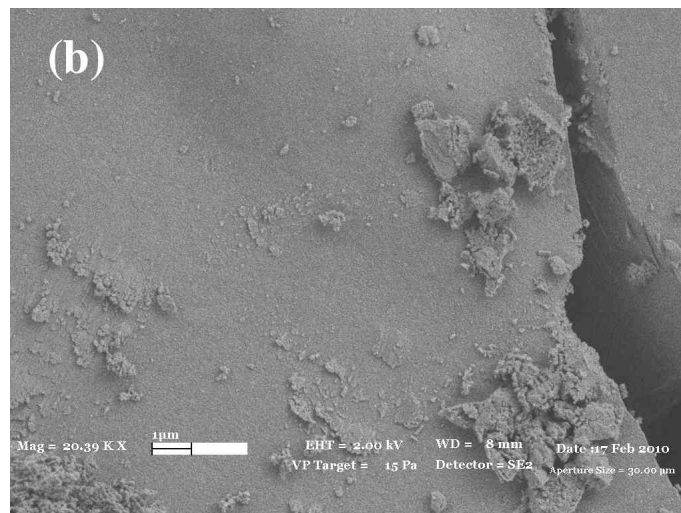
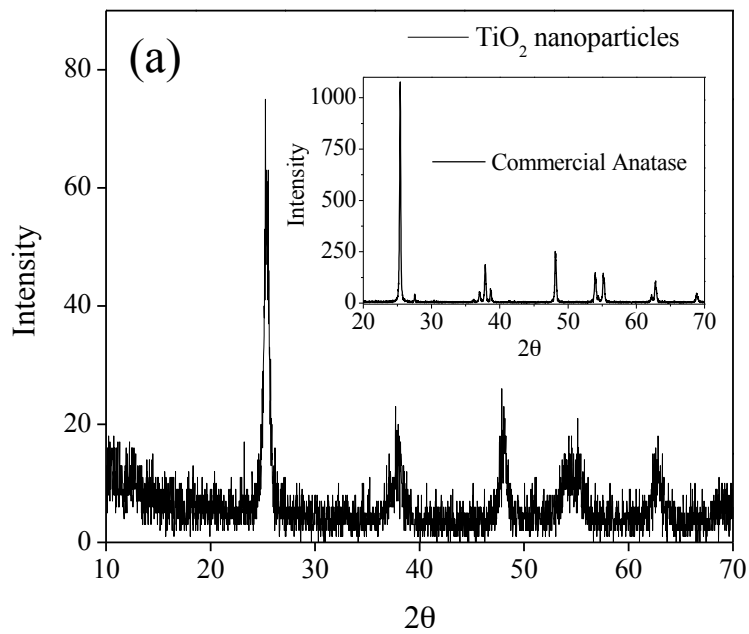


Figure 7.1. XRD spectra of the TiO₂ nanoparticles and commercial anatase powder (a), SEM images of the TiO₂ nanoparticles at 20 kX (b) and 120 kX (c).

7.3.2. Effect of pH

The pH is a significant parameter for determining the adsorption between the adsorbent and aqueous interface. The uptakes of As(III) and As(V) onto anatase nanoparticles for an initial concentrations of 4.5 mg/L within a pH range of 2.0-10.0 were shown in Figure 7.2. The maximum arsenic removal percentages were found 43% for As(III) at pH 7 and 91% for As(V) at pH 3, respectively. The ionic character of the arsenic species varies with pH as the predominant As(III) species available are H_3AsO_3 and $H_2AsO_3^-$ in the pH range of 4.0-9.5, while the predominant As(V) species show variation with pH values: H_3AsO_4 (pH 0.0-2.0), $H_2AsO_4^-$ (pH 3.0-6.0), $HAsO_4^{2-}$ (pH 7.0-11.0) [270]. In literature, the point of zero charge (pzc) for the anatase nanoparticles was approximately found in between 5.9-6.9 [230].

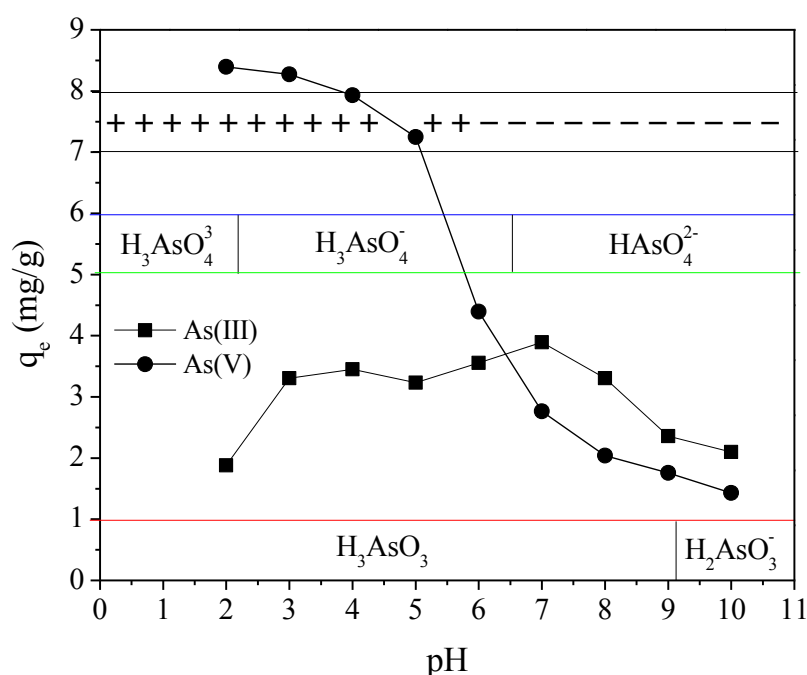


Figure 7.2. Effect of pH on the adsorptions of As(III) and As(V) [Adsorbent amount: 0.5 g/L, initial arsenic concentration: 4.5 mg/L reaction temperature: 25°C]

The anatase nanoparticles are composed of the mixture of positively charged $TiOH_2^+$ and neutral species of $TiOH^0$ when pH is below. However, the primary species of the nanoparticles include the neutral species of $TiOH^0$ and the negatively charged TiO^-

when pH is above pH_{pzc} [213]. The surface of nanoparticles mostly covered with the neutral $TiOH^0$ and negatively charged TiO^- at pH 7.0. This explained the higher adsorption of As(III) on to TiO_2 nanoparticles. On the other hand, positively charged $TiOH_2^+$ and neutral species of $TiOH^0$ were dominant at pH 3 on the surface of nanoparticles. Thus, at acidic pH conditions surface of adsorbent was covered with positively charged surface groups that boost the adsorption of the negatively charged As(V) anions. Similar increase in As(V) uptakes through the acidic pH values was also observed for mesoporous alumina [271] and mesoporous Ce–Fe bimetal oxide [272].

7.3.3. Effect of contact time on arsenic removal and kinetic modeling

The effect of contact time on the adsorptions of As(III) and As(V) were illustrated in Figure 7.3. The synthesized TiO_2 nanoparticles revealed better results for As(V) adsorption capability as compared to As(III). In contrast, both arsenic species required at least 180 minutes to reach steady state. At initial stage of adsorption, most of the reactive sites on the TiO_2 were available for the adsorption, therefore rapid increase in uptakes of arsenic species were achieved. However, the slower uptake of arsenic species at later stage was observed and it could be attributed to diffusion of arsenic into adsorbent in order to find available sorption sites or surface reactions of arsenic [222].

The kinetic data obtained from this study were first analyzed by employing the pseudo first order [122] (Equation 7.2) and the pseudo second order [189] (Equation 7.3) equations:

$$\log(q_e - q_t) = \log(q_e) - \frac{k_1 t}{2.303} \quad (7.2)$$

$$\frac{t}{q_t} = \frac{1}{k_2 q_e^2} + \frac{t}{q_e} \quad (7.3)$$

where, q_t is the amount of arsenic adsorbed (mg/g) at time t , q_e is the maximum adsorption capacity (mg/g) for the pseudo first order adsorption and pseudo second

order adsorption, k_1 is the pseudo first order rate constant for the arsenic adsorption process (min^{-1}), k_2 is the pseudo second order rate constant (g/mg min).

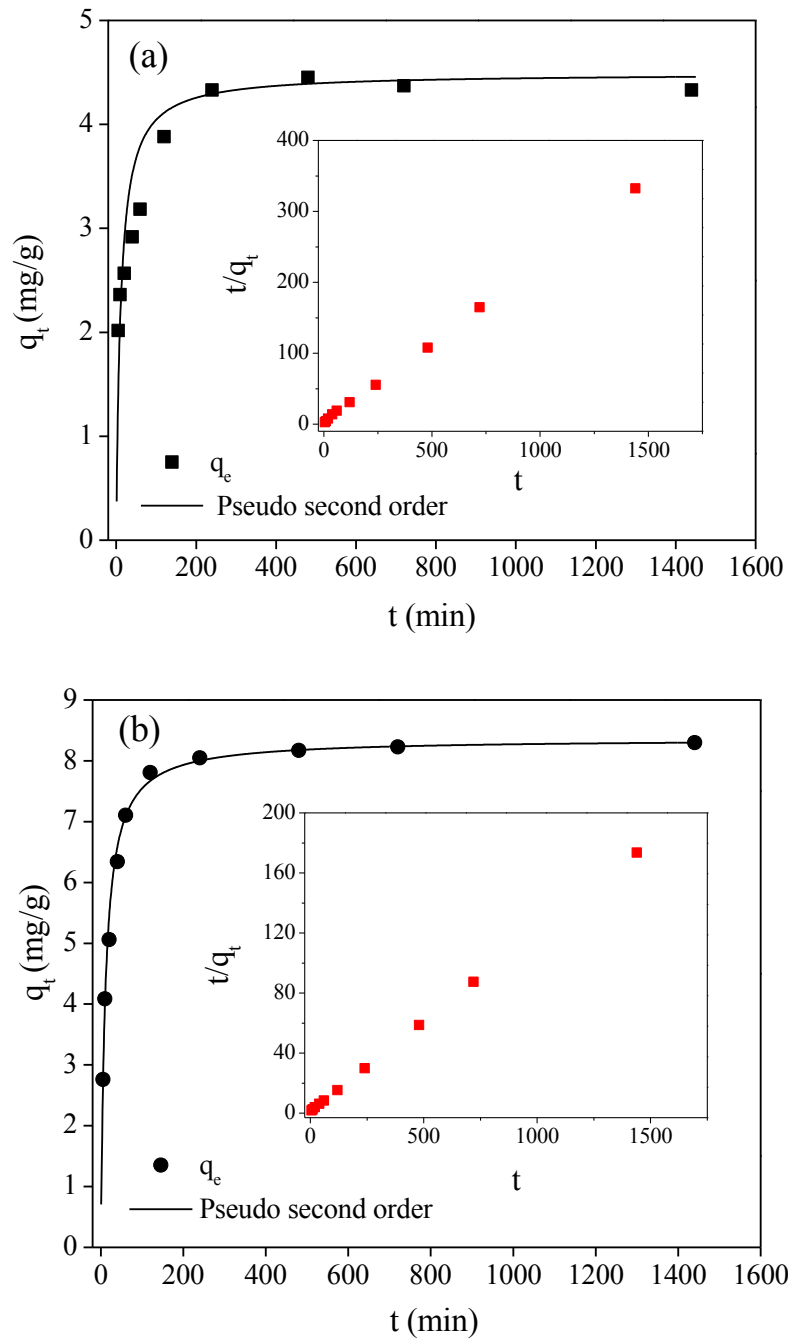


Figure 7.3. Time dependence of As(III) (a) and As(V) (b) adsorbent amount, 0.5 g/L; initial arsenic concentration: 4 mg/L, pH, ~ 6 for As(III) and ~ 4 for As(V). The inset of figure represents pseudo second order curve for adsorption of As(III) and As(V) on TiO_2 nanoparticles.

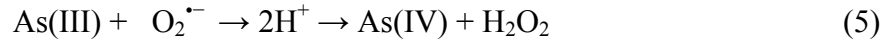
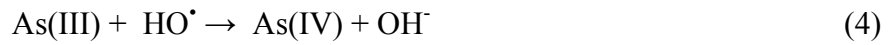
The sorption modeling parameters were summarized in Table 7.1. The pseudo second order model seemed to be the better-fitting model for the removal of As(III) and As(V). It is obvious from the obtained correlation coefficient (R^2) that the data were explained well by pseudo-second order model, indicating the predominant mechanism of the adsorption process was chemisorption that involved chemical bonding via valence forces by sharing or exchanging the electrons between adsorbate and adsorbent [273]. The calculated k_2 value for As(III) was higher than that for As(V), suggesting the adsorption rate of As(III) by TiO₂ nanoparticles was fast in some extent as compared to the adsorption rate of As(V).

Table 7.1. The kinetic sorption modeling parameters for As(III) and As(V) adsorption on to TiO₂ nanoparticles

Model	Parameters	As(III)	As(V)
Pseudo First Order	k_1 (1/min)	0.017	0.005
	q_{e1} (mg/g)	3.139	2.471
	R^2	0.982	0.8245
Pseudo Second Order	k_2 (g/mg.min)	0.021	0.011
	q_{e2} (mg/g)	4.392	8.361
	R^2	0.999	0.999
	h (mg/g.min)	0.406	0.774

7.3.4. Role of UV-A Illumination

As TiO₂ is illuminated, electrons and holes are generated and various chemical redox reactions are initiated due to the migration of those pairs to the TiO₂ surface [214]. When the electrons and holes do not recombine, they can reduce and oxidize other molecules at the TiO₂ surface. The potential mechanisms of As(III) oxidation to As(V) by using the TiO₂ as an adsorbent were shown in below.



Because of the short life times of both excited electron-hole pairs, the produced radicals such as hydroxyl radicals ($\cdot\text{OH}$ and $\text{HO}_2\cdot$) and superoxide radicals ($\text{O}_2^{\bullet -}$) [274] from the photocatalytic reactions occur only close to the photocatalyst surface [275]. Therefore it is important that photocatalysts have good interactions with arsenic species. In Figure 7.4, the effect of illumination time on As(III) oxidation was tested at an initial adsorbate concentration of 4 mg/L and adsorbent amount 0.5 g/L. A period of 120 min UV-A light irradiation was sufficient to reach steady state condition in the presence of TiO_2 nanoparticles. The maximum uptake of As(III) was 8.47 mg/g at 360 min interaction time.

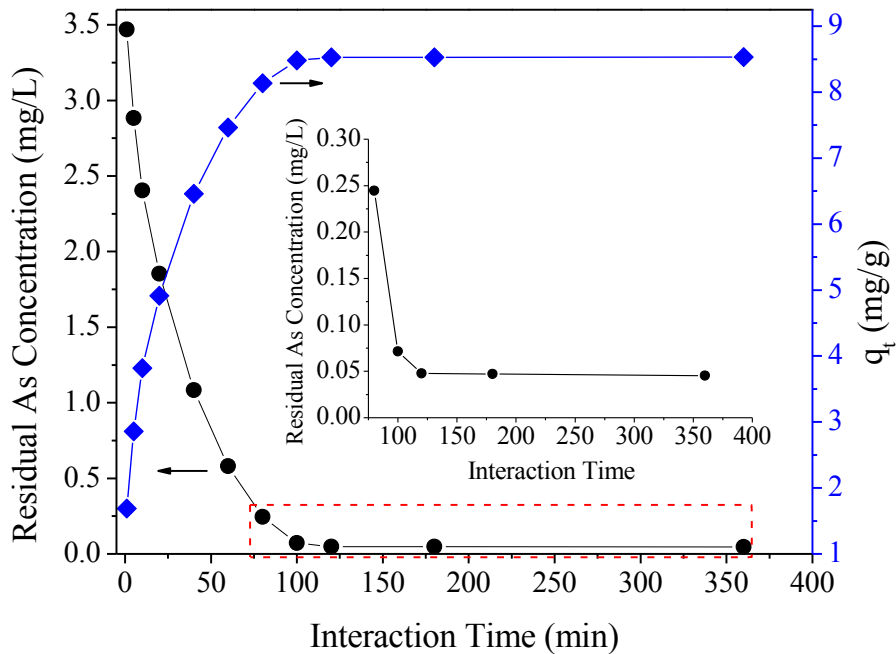


Figure 7.4. Effect of UV-A light interaction time on As(III) adsorption from water by TiO_2 nanoparticles.

In Figure 7.5, the residual arsenic concentrations were shown with and without UV-A illumination by using TiO₂ nanoparticles. It was observed that the UV-A irradiation significantly enhanced the adsorption of As(III) species from water. In the absence of UV light, As (III) removal was less than As(V) removal which was consistent with literature that report the sorption capacity of TiO₂ for As(III) to be less than that of As(V) [86, 143]. In the presence of UV-A light, residual As(III) concentration was approximately equal to As(V) suggesting that TiO₂ oxidized As(III) to As(V) and removed arsenic as As(V). As shown in Figure 7.5, the lower pH values contributed to greater arsenic removal efficiencies for As(III) species with UV-A illumination and for As(V) species without UV-A illumination. The data in Figure 7.5 supported previously reported results that in the presence of UV light and nano-TiO₂, As(III) is readily oxidized to As(V) [209, 276].

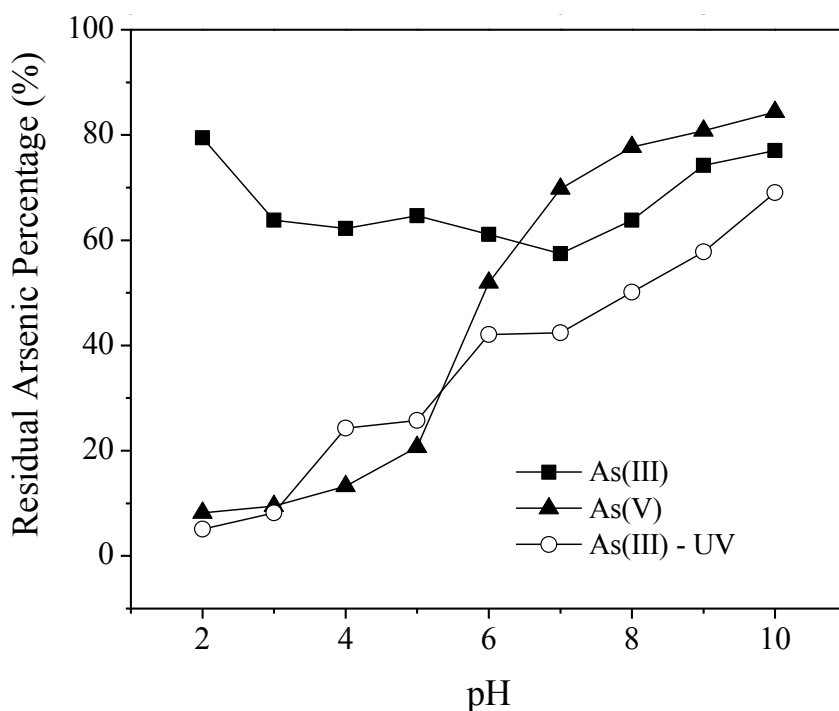


Figure 7.5. Residual arsenic concentrations versus pH considering with and without UV-A illumination by using TiO₂ nanoparticles.

7.3.5. Adsorption isotherm

The As(III) and As(V) adsorption studies onto the nanoparticles were investigated by varying the initial sorbate concentrations ranging from 1 to 25 mg/L. The nonlinear

adsorption isotherms for As(III) with/without UV-A illumination and As(V) were given for the nanoparticles in Figure 7.6. The maximum adsorption capacities were found 12.13 mg/g for As(III) in the absence of UV-A illumination, 41.38 mg/g for As(V), and 36.55 mg/g for As(III) in the presence of UV-A illumination. The results were higher than or compatible with the previously results reported. A comparable result in terms of the initial arsenic concentration could be found in the recent work of Xu and Meng [277] synthesized TiO₂ particles ranging from 6.6 to 30.1 nm after calcining nanocrystalline TiO₂ at different temperatures. They evaluated the effect of the crystalline size on the adsorption by using initial arsenic concentration of 50 mg /L in a suspension containing 1 g/L TiO₂. The maximum arsenic adsorption capacity of 6.6 nm TiO₂ for As(V) was calculated by the Langmuir model to be 30.5 mg g⁻¹ and the adsorption capacities of the TiO₂ for As(III) were slightly less than that for As(V).

The theoretical adsorption capacity of an adsorbent can be obtained through the adsorption isotherm. Langmuir and Freundlich isotherm models were investigated to evaluate adsorption patterns of arsenic on to TiO₂ nanoparticles with respect to its concentration of equilibrium in solutions. Langmuir [130] (Equation 7.4) and Freundlich [181] (Equation 7.5) isotherms can be expressed by the following equations:

$$q_e = \frac{q_{mon} b C_e}{1 + b C_e} \quad (7.4)$$

$$q_e = K_F C_e^{1/n} \quad (7.5)$$

where q_e is the solute amount adsorbed per unit weight of adsorbent (mg/g), C_e is liquid phase sorbate concentration in equilibrium, q_{mon} is the monolayer adsorption capacity (mg/g), b is the adsorption equilibrium constant (L/mg) related to adsorption enthalpy ($b \propto \exp^{-\Delta H/RT}$), K_F indicates the adsorbent's relative adsorption capacity (mg/g), $1/n$ is the constant representing adsorption intensity. If the value of $1/n$ is lower than 1, it indicates a normal Langmuir isotherm; otherwise, it is indicative of cooperative adsorption [211].

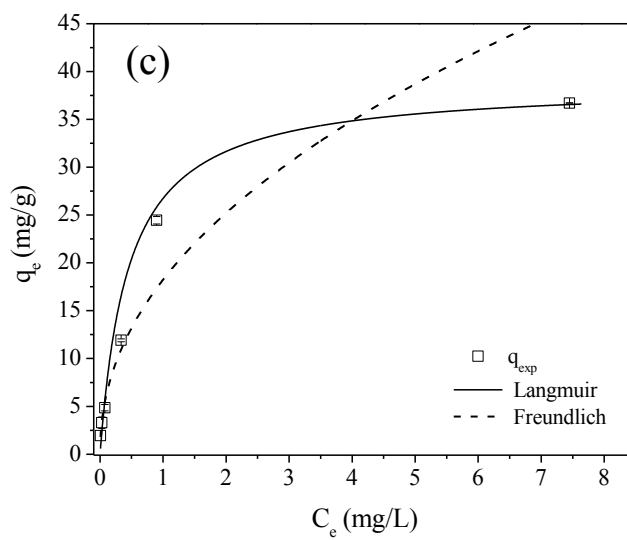
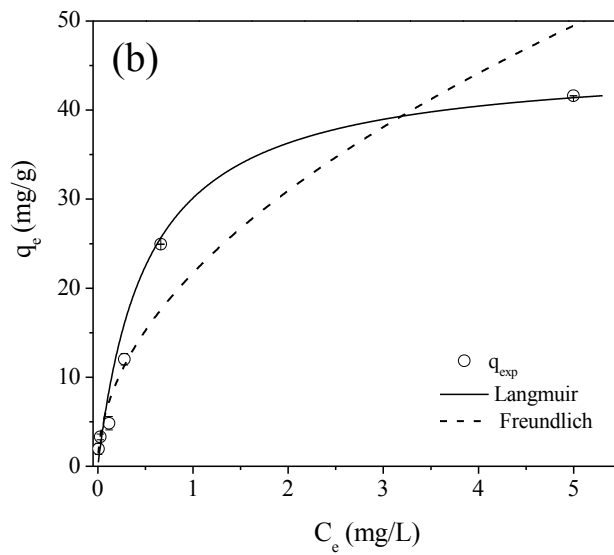
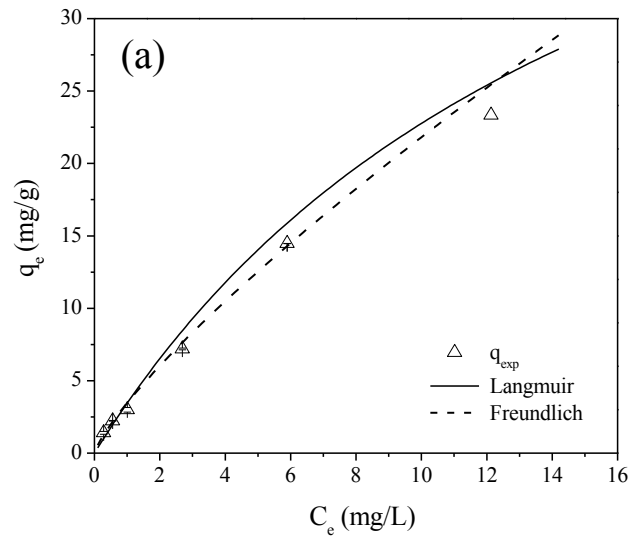


Figure 7.6. Adsorption isotherm of As(III) (a), As(V) (b) and UV-light illuminated As(III) (c) onto TiO_2 nanoparticles.

Figure 7.7 depicted the linearized Langmuir and Freundlich models of As(III), As(V), and UV-A illuminated As(III). The adsorption isotherm parameters were summarized in Table 7.2. Considering obtained R^2 values, the adsorption isotherm behavior of As(III) in the absence of UV illumination was better fitted to Freundlich isotherm. On the other hand, the Langmuir model successfully explained the adsorption of As(V) and UV-A illuminated As(III) ions onto the nanoparticles. The respective $1/n$ values were within the range between 0 and 1 showing beneficial adsorptions for As(III) with/without UV illumination and As(V) by using TiO_2 nanoparticles.

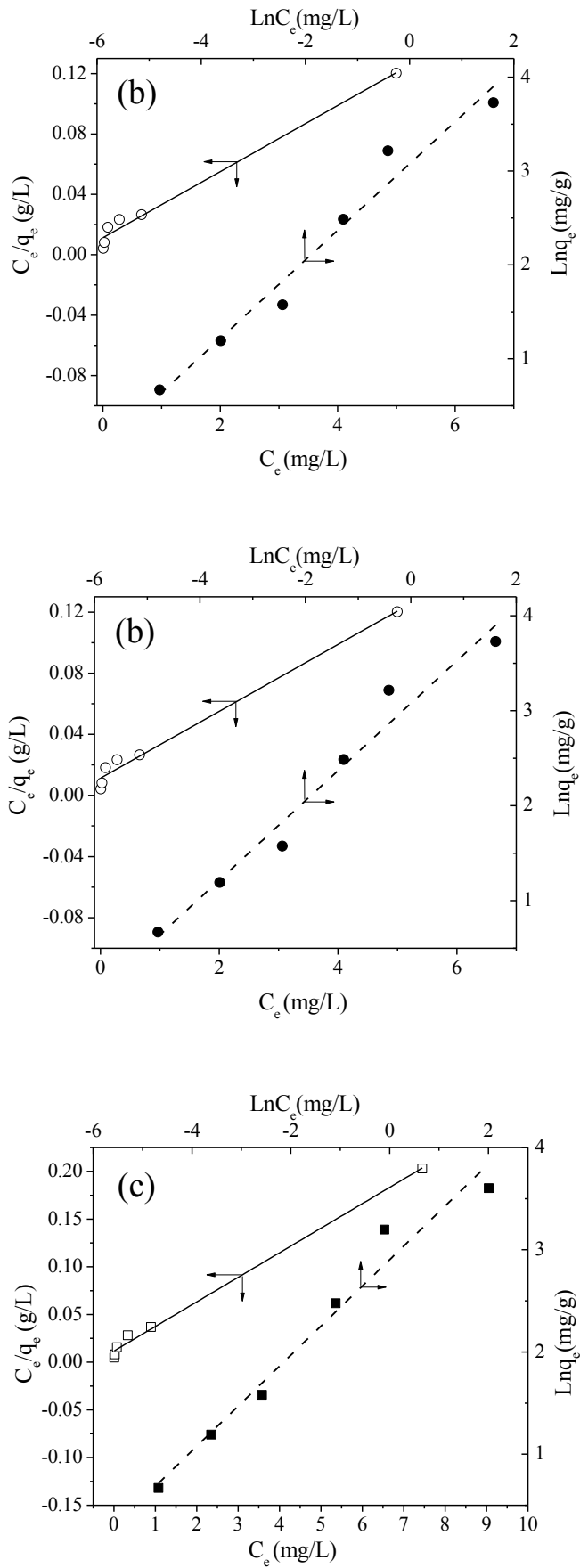


Figure 7.7. Langmuir and Freundlich plots of the adsorption data of As(III) (a), As(V) (b) and UV-light illuminated As(III) (c) in the concentration range from 1 to 25 mg/L.

Table 7.2. Adsorption isotherm parameters for As(III) with/without UV illumination and As(V) by using TiO₂ nanoparticles.

Isotherm Parameters	As(III)	As(V)	As(III)-UV
q _{exp} (mg/g)	12.13	41.38	36.55
Langmuir			
q _{mon} (mg/g)	60.25	45.66	38.76
b (L/mg)	0.061	1.938	2.224
R ²	0.771	0.986	0.995
Freundlich			
K _F (mg/g)	3.464	21.70	18.23
1/n	0.799	0.512	0.467
R ²	0.991	0.969	0.971

7.3.6. Adsorption Energy

Dubinin-Kaganer-Radushkevich (DKR) isotherm model was investigated to determine the physical and chemical adsorption of arsenic. DKR isotherm equation [136] is:

$$\ln q_e = \ln X_m - k \varepsilon^2 \quad (7.6)$$

where ε is Polanyi potential, equal to $RT \ln (1+1/C_e)$, X_m is the adsorption capacity (mol/g), k is a constant related to adsorption energy (mol²/kJ²). X_m and k values were obtained by plotting $\ln q_e$ versus ε^2 at 25 °C as illustrated in Figure 7.8, the slope of line yields k (mol²/kJ²) and the intercept is equal to $\ln X_m$. In order to evaluate the interaction between arsenic and binding sites of TiO₂, the mean free energy of adsorption (E) (the free energy change one mol adsorbate in transferred from infinity in solution to the surface of the adsorbent) was calculated from the following relationship [133].

$$E = - (2k)^{-0.5} \quad (7.7)$$

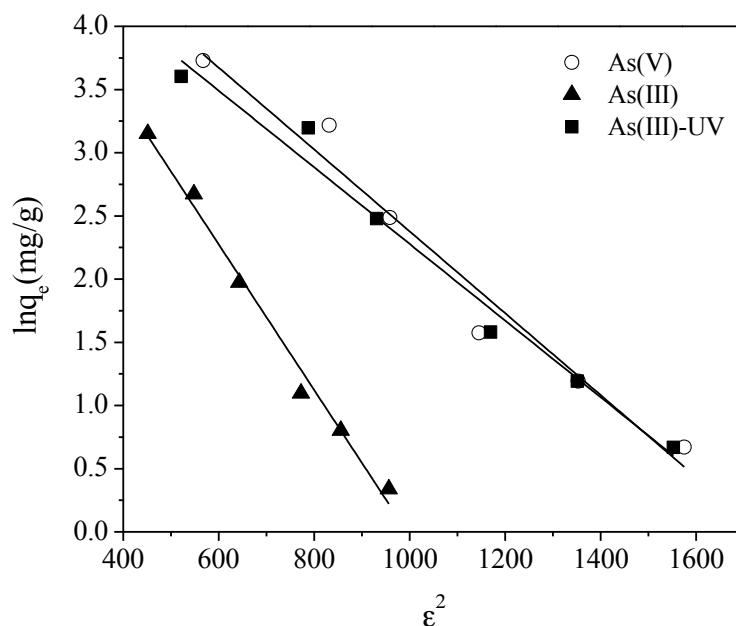


Figure 7.8. The linearized graph of DKR isotherm for As(III), As(V), and UV-illuminated As(III).

The calculated E values were -17.68 kJ/mol for As(V) at pH 7.0, -12.80 kJ/mol for As(III) at pH 3, and -18.26 kJ/mol for As(III) with UV treatment at pH 3.0, respectively. It has been stated that the value of ΔG found below 8 kJ/mol is consistent with a physical adsorption involving electrostatic interaction between adsorption sites and the adsorbate ion. Moreover, it has been noted that if the value of ΔG is in between 8 and 16 kJ/mol, the adsorption proceeds via a chemical ion exchange mechanism. The more negative ΔG values imply chemisorption mechanism by forming stable complexes on the adsorbent surface [227]. The obtained E values for As(III) and As(V) suggested ion-exchange as major mechanism responsible for the adsorption process. In the case of removal of As(III) in the presence of UV illumination, the most probable type of reaction would be chemisorption according to the value of E .

7.4. Concluding Remarks

By using sol-gel method, TiO₂ nanoparticles were fabricated with particle size ranging 10 to 150 nm. Adsorption experiments were performed for anatase to obtain optimum pH and contact time. The obtained TiO₂ nanoparticles revealed better results for As(V) adsorption capability as compared to As(III). Based on the R^2 values, the pseudo-second-order model described the adsorption kinetics. It was observed that the low As(III) adsorption capacity of TiO₂ nanoparticles from water limits its application in contaminated water treatment and adsorption of As(III) was enhanced by UV irradiation. The removal capacity of total arsenic from water was improved by UV irradiation about approximately third times as compared to purely adsorption process of TiO₂ nanoparticles.

CHAPTER 8

CONCLUSION

4.1. Concluding Remarks

In this thesis, FRM, iron oxide, TiO₂ nanoparticles and composites based on activated carbon were successfully fabricated. Numerous adsorption and photocatalytic oxidation experiments were performed to utilize these adsorbents in order to remove arsenic, copper, lead from water. The important outputs of the each chapter were summarized in below.

Chapter 3 evaluated the arsenic removal efficiency of FRM considering effect of pH, initial arsenic concentration, and contact time. It is suggested that FRM is very effective adsorbent that reduce both As(III) and As(V) concentrations below the MCL requirements for drinking water. Moreover, it is important to note that using of 1 g/L FRM dosage for an initial arsenic concentration of 1 mg/L, the maximum arsenic uptakes were found 0.57 mg/L for As(III) at pH 7.6 and 0.98 mg/L for As(V) at pH 3.3, respectively. Kinetic sorption experiments indicated higher regression coefficients (R^2) after the application of pseudo-second order to the experimental data of As(III) and As(V) initial concentrations. In terms of adsorption mechanisms of As(III) and As(V) onto FRM, external diffusion mechanism governed the initial stage of adsorptions and while the intraparticle diffusion mechanism was rate-determining step for the later stages of adsorption. The most important observation was that the higher adsorption capacities achieved from Langmuir isotherm model was found for As(V) at pH 2.0 as compared to As(III) at pH 7.0 and the calculated maximum adsorption capacity values were 11.640 mg/g for As(V) pH 7.0 and 5.254 mg/g for As(III). Essentially, present

results are promising for the usage of FRM in drinking water contaminated with low concentration of arsenic species.

Chapter 4 presented the deposition of iron oxide nanoparticles on to activated carbon with a new technique indicating very promising results. Iron oxide nanoparticles were deposited uniformly on activated carbon support rapidly with high loadings with microwave hydrothermal treatment. XRD analyses revealed that not only α - Fe_2O_3 , but also β - FeOOH particles could be generated with the adjustment of heating duration. With this method, about 20% of iron loading was obtained in less than 9 minutes. Uniformity and amount of iron oxide could be adjusted with surface oxidation and duration of microwave heating. However, adsorption isotherms and porous texture studies indicated that, available sites started to disappear at extended times of heating due to agglomeration of iron oxide particles on the surface. For ACO, high As(V) uptake value like 27.78 mg/g was obtained and 99.90% of uptake was reached within 5 minutes of batch adsorption process. With adsorption isotherm and kinetic studies, it was understood that As(V) adsorption onto iron oxide deposited AC and ACO fits Langmuir and pseudo-second order models. High As(V) uptakes were obtained in the range of pH 6.0-8.0. The high As(V) adsorption performance, especially at pH 7.0, makes the material a good candidate for water treatment processes.

Chapter 5 indicated greater Pb(II) and Cu(II) removal potential of synthesized anatase nanoparticles from drinking water. Additionally, the nanoparticles were able to reduce As(III) concentrations below the MCL requirements for drinking water up to moderate initial concentrations. The amount of Pb(II) and Cu(II) ions removed from water was strongly influenced by the pH and the type of reactive adsorbate species and active sites on the surface of adsorbent. Based on the R^2 and APE values, the pseudo second order model described the Pb(II), Cu(II), and As(III) adsorption kinetics. Langmuir model fitted well for Pb(II) uptake supported with lower APE and higher R^2 value, on the other hand the higher relationship between experimental and calculated adsorption data for Cu(II) and As(III) were observed in Freundlich isotherm model. Based on experimental data, the maximum adsorption capacity for Cu(II), Pb(II), and As(III) ions were 31.25 mg/g, 23.74 mg/g, and 16.95 mg/g respectively. Thermodynamic parameters indicated that the calculated ΔS values were positive and the favorable Gibbs energies were entropically controlled in the adsorptions of Pb(II) and Cu(II), while the As(III)

adsorption was thermodynamically favorable without any limitations. XPS analyses revealed that the surface oxygen-containing functional groups including hydroxyl groups were involved in the adsorption process. Thus, the whole Pb(II), Cu(II), and As(III) sorption studies on the nanoparticles indicated that the synthesized nanoparticles can be effectively used in the treatment of water polluted with the arsenic and heavy metal ions.

Chapter 6 presented the fabrication of AC/TiO₂ nanocomposites by varying the content of AC in the system. According to the results obtained from SEM and BET, TiO₂ nanoparticles were inserted into the external surface and inside the pores of AC and the surface area of the nanocomposites increased with the higher amount of AC. TGA results showed that AC was stable up to 400°C, however, presence of TiO₂ nanoparticles in the system led to weight loss at earlier stage approximately at 100°C. Moreover, it was found that AC/TiO₂ composites exhibited a better adsorption capacity for As(III) which is 2.7 times greater than that of bare TiO₂. The maximum As(III) removal was found 26.62 mg/L for the 10-AC/TiO₂ nanocomposite at pH 7.0. However, increasing the amount of AC in the composite system led to decline in the adsorption. The 10-AC/TiO₂ nanocomposite have a potential application for arsenic removal in water treatment due to its high As(III) adsorption –desorption capabilities. The removal efficiency after five cycles was 82%, demonstrating that it could be used as an effective material for many cycles by regeneration. Embedding the nanoparticles onto AC provided the prevention of release of the nanoparticles to the environment and at the same time, the reactivity of them improved as compared to bare TiO₂.

Chapter 7 highlighted the improvement of As(III) removal from water by using synthesized TiO₂ nanoparticles under UV-A light irradiation. Sol-gel method was preferred to synthesize TiO₂ nanoparticles ranging 10 to 150 nm. Adsorption experiments were performed in order to obtain optimum pH and contact time. The obtained TiO₂ nanoparticles revealed better results for As(V) adsorption capability as compared to As(III). Based on the R^2 values, the pseudo second order model described the adsorption kinetics. It was observed that the low As(III) adsorption capacity of TiO₂ nanoparticles from water limits its application in contaminated water treatment and adsorption of As(III) was enhanced by UV-A light irradiation. The maximum adsorption capacities were found 12.13 mg/g for As(III) in the absence of UV-A

illumination, 41.38 mg/g for As(V), and 36.55 mg/g for As(III) in the presence of UV-A illumination. The removal capacity of total arsenic from water was improved by UV-A light irradiation about approximately third times as compared to purely adsorption process of TiO₂ nanoparticles.

8.2. Future Works

The adsorption experiments for Pb(II) and Cu(II) by using synthesized 10-AC/TiO₂ nanocomposite which indicated better adsorption capability for As(III) is recommended. In addition to that, the As(III) adsorption behavior of the nanocomposite would be analyzed under UV-A light illumination. The As(III), Pb(II), and Cu(II) adsorption abilities of other carbonaceous material such as carbon nanotubes, carbon nanofibers, and graphene might be further tested.

REFERENCES

1. Min Jang, W.C., Jiying Zou, Fred S. Cannon, and Brian A. Dempsey, *Arsenic Removal by Iron-Modified Activated Carbon*, 2010, Arsenic Water Technology Partnership. p. 3.
2. Bonato, M., K.V. Ragnarsdottir, and G.C. Allen, *Removal of Uranium(VI), Lead(II) at the Surface of TiO₂ Nanotubes Studied by X-Ray Photoelectron Spectroscopy*. Water Air and Soil Pollution, 2012. **223**(7): p. 3845-3857.
3. Weng, C.H., et al., *Adsorption characteristics of copper(II) onto spent activated clay*. Separation and Purification Technology, 2007. **54**(2): p. 187-197.
4. Choong, T.S.Y., et al., *Arsenic toxicity, health hazards and removal techniques from water: an overview*. Desalination, 2007. **217**(1-3): p. 139-166.
5. Westerhoff, G.a.Z.K.C., *Water Treatment Systems,* " Chapter in *Water Resources Handbook*, L.M.M. ed., Editor 1996, McGraw Hill: New York.
6. Chwirka, J.D., et al., *Arsenic removal from drinking water using the coagulation/microfiltration process*. Journal American Water Works Association, 2004. **96**(3): p. 106-114.
7. Savage, N. and M.S. Diallo, *Nanomaterials and water purification: Opportunities and challenges*. Journal of Nanoparticle Research, 2005. **7**(4-5): p. 331-342.
8. Pelaez, M., et al., *A review on the visible light active titanium dioxide photocatalysts for environmental applications*. Applied Catalysis B-Environmental, 2012. **125**: p. 331-349.
9. Naranjo-Pulido, A., et al., *Soil arsenic contamination in the Cape Region, BCS, Mexico*. Journal of Environmental Biology, 2002. **23**(4): p. 347-352.
10. Martell, A.E.e., al., *NIST critically selected stability constants of metals complexes*, , ed. E. NIST2001: U.d.o.C.N.I.o.S.a.T.S.r.d. program.
11. Aklil, A., M. Mouflih, and S. Sebti, *Removal of heavy metal ions from water by using calcined phosphate as a new adsorbent*. Journal of Hazardous Materials, 2004. **112**(3): p. 183-190.
12. Ng, J.C., J.P. Wang, and A. Shraim, *A global health problem caused by arsenic from natural sources*. Chemosphere, 2003. **52**(9): p. 1353-1359.
13. Meyer, P.A., M.J. Brown, and H. Falk, *Global approach to reducing lead exposure and poisoning*. Mutation Research-Reviews in Mutation Research, 2008. **659**(1-2): p. 166-175.
14. Ala, A., et al., *Wilson's disease*. Lancet, 2007. **369**(9559): p. 397-408.
15. Regulations, N.P.D.W., *EPA Report No. EPA 816-F-09-0004; Environmental Protection Agency* May 2009, Washington, DC.
16. Maiti, A., et al., *Batch and column study: Adsorption of arsenate using untreated laterite as adsorbent*. Industrial & Engineering Chemistry Research, 2008. **47**(5): p. 1620-1629.
17. Mohora, E., et al., *Removal of natural organic matter and arsenic from water by electrocoagulation/flotation continuous flow reactor*. Journal of Hazardous Materials, 2012. **235**: p. 257-264.
18. Ghurye, G. and D. Clifford, *As(III) oxidation using chemical and solid-phase oxidants*. Journal American Water Works Association, 2004. **96**(1): p. 84-96.
19. Qu, D., et al., *Experimental study of arsenic removal by direct contact membrane distillation*. Journal of Hazardous Materials, 2009. **163**(2-3): p. 874-879.

20. Ma, J., et al., *One-pot, large-scale synthesis of magnetic activated carbon nanotubes and their applications for arsenic removal*. Journal of Materials Chemistry A, 2013. **1**(15): p. 4662-4666.
21. An, H.K., B.Y. Park, and D.S. Kim, *Crab shell for the removal of heavy metals from aqueous solution*. Water Research, 2001. **35**(15): p. 3551-3556.
22. Faur-Brasquet, C., K. Kadirvelu, and P. Le Cloirec, *Removal of metal ions from aqueous solution by adsorption onto activated carbon cloths: adsorption competition with organic matter*. Carbon, 2002. **40**(13): p. 2387-2392.
23. Gulbas, G., et al., *Arsenic removal from aqueous system using natural and modified (Kula ebonite and zeolite) adsorbents*. Environmental Progress & Sustainable Energy, 2012. **31**(3): p. 443-448.
24. Biswas, P. and C.Y. Wu, *2005 Critical Review: Nanoparticles and the environment*. Journal of the Air & Waste Management Association, 2005. **55**(6): p. 708-746.
25. Roco, M.C., *The emergence and policy implications of converging new technologies integrated from the nanoscale*. Journal of Nanoparticle Research, 2005. **7**(2-3): p. 129-143.
26. Simon, J., *Micro- and nanotechnologies: dulleish electrons and smart molecules*. Comptes Rendus Chimie, 2005. **8**(5): p. 893-902.
27. Yuan, Z.Y. and B.L. Su, *Titanium oxide nanotubes, nanofibers and nanowires*. Colloids and Surfaces a-Physicochemical and Engineering Aspects, 2004. **241**(1-3): p. 173-183.
28. Cornel RM, S.U., *The Iron Oxides: Structure, Properties, Reactions, Occurrences and Uses* 1996, New York: Weinheim.
29. Dias, A.M.G.C., et al., *A biotechnological perspective on the application of iron oxide magnetic colloids modified with polysaccharides*. Biotechnology Advances, 2011. **29**(1): p. 142-155.
30. Gupta, A.K. and M. Gupta, *Synthesis and surface engineering of iron oxide nanoparticles for biomedical applications*. Biomaterials, 2005. **26**(18): p. 3995-4021.
31. Carp, O., C.L. Huisman, and A. Reller, *Photoinduced reactivity of titanium dioxide*. Progress in Solid State Chemistry, 2004. **32**(1-2): p. 33-177.
32. Duruibe, J.O., M.O.C. Ogwuegbu, and J.N. Egwurugwu, *Heavy metal pollution and human biotoxic effects*. International Journal of Physical Sciences, 2007. **2**(5): p. 112-118.
33. Rivera-Reyna, N., et al., *Photocatalytical removal of inorganic and organic arsenic species from aqueous solution using zinc oxide semiconductor*. Photochemical & Photobiological Sciences, 2013. **12**(4): p. 653-659.
34. Colvin, V.L., *The potential environmental impact of engineered nanomaterials (vol 21, pg 1166, 2003)*. Nature Biotechnology, 2004. **22**(6): p. 760-760.
35. Mohan, D. and C.U. Pittman, *Arsenic removal from water/wastewater using adsorbents - A critical review*. Journal of Hazardous Materials, 2007. **142**(1-2): p. 1-53.
36. Pfeifer, H.R., et al., *Dispersion of natural arsenic in the Malcantone watershed, Southern Switzerland: field evidence for repeated sorption-desorption and oxidation-reduction processes*. Geoderma, 2004. **122**(2-4): p. 205-234.
37. Das, D., et al., *Arsenic in Ground-Water in 6 Districts of West-Bengal, India - the Biggest Arsenic Calamity in the World .2. Arsenic Concentration in Drinking-Water, Hair, Nails, Urine, Skin-Scale and Liver-Tissue (Biopsy) of the Affected People*. Analyst, 1995. **120**(3): p. 917-924.

38. Jain, C.K. and I. Ali, *Arsenic: Occurrence, toxicity and speciation techniques*. Water Research, 2000. **34**(17): p. 4304-4312.
39. Hering, J.G., et al., *Arsenic removal by ferric chloride*. Journal American Water Works Association, 1996. **88**(4): p. 155-167.
40. USEPA, F.R., 2001. **66**(14): p. 6976-7066.
41. Kartinen, E.O. and C.J. Martin, *An overview of arsenic removal processes*. Desalination, 1995. **103**(1-2): p. 79-88.
42. Pontius, F.W., K.G. Brown, and C.J. Chen, *Health Implications of Arsenic in Drinking-Water*. Journal American Water Works Association, 1994. **86**(9): p. 52-63.
43. Mondal, P., C.B. Majumder, and B. Mohanty, *Laboratory based approaches for arsenic remediation from contaminated water: Recent developments*. Journal of Hazardous Materials, 2006. **137**(1): p. 464-479.
44. Brandhuber, P. and G. Amy, *Alternative methods for membrane filtration of arsenic from drinking water*. Desalination, 1998. **117**(1-3): p. 1-10.
45. Gerente, C., et al., *Interactions of natural aminated polymers with different species of arsenic at low concentrations: Application in water treatment*. Adsorption-Journal of the International Adsorption Society, 2005. **11**: p. 859-863.
46. Anderson, L.C.D. and K.W. Bruland, *Biogeochemistry of Arsenic in Natural-Waters - the Importance of Methylated Species*. Environmental Science & Technology, 1991. **25**(3): p. 420-427.
47. Edwards, M., *Chemistry of Arsenic Removal during Coagulation and Fe-Mn Oxidation*. Journal American Water Works Association, 1994. **86**(9): p. 64-78.
48. Saha, J.C., et al., *A review of arsenic poisoning and its effects on human health*. Critical Reviews in Environmental Science and Technology, 1999. **29**(3): p. 281-313.
49. Korte, N.E. and Q. Fernando, *A Review of Arsenic(Iii) in Groundwater*. Critical Reviews in Environmental Control, 1991. **21**(1): p. 1-39.
50. Pichler, T., J. Veizer, and G.E.M. Hall, *Natural input of arsenic into a coral reef ecosystem by hydrothermal fluids and its removal by Fe(III) oxyhydroxides*. Environmental Science & Technology, 1999. **33**(9): p. 1373-1378.
51. Wang, S. and C.N. Mulligan, *Occurrence of arsenic contamination in Canada: Sources, behavior and distribution*. Science of the Total Environment, 2006. **366**(2-3): p. 701-721.
52. Jiang, J.Q., *Removing arsenic from groundwater for the developing world - a review*. Water Science and Technology, 2001. **44**(6): p. 89-98.
53. Registry, A.f.T.S.a.D. *Priority List of Hazardous Substance*. 2011; Available from: <http://www.atsdr.cdc.gov/SPL/index.html>.
54. Gupta, V.K., M. Gupta, and S. Sharma, *Process development for the removal of lead and chromium from aqueous solutions using red mud - an aluminium industry waste*. Water Research, 2001. **35**(5): p. 1125-1134.
55. Papanikolaou, N.C., et al., *Lead toxicity update. A brief review*. Medical Science Monitor, 2005. **11**(10): p. Ra329-Ra336.
56. Groffman, A., Peterson, S., Brookins, D., *Removing lead from wastewater using zeolites*. Water Environ. Technol., 1992. **5**: p. 54-59.
57. Meggers, E., et al., *A novel copper-mediated DNA base pair*. Journal of the American Chemical Society, 2000. **122**(43): p. 10714-10715.

58. Paulino, A.T., et al., *Novel adsorbent based on silkworm chrysalides for removal of heavy metals from wastewaters*. Journal of Colloid and Interface Science, 2006. **301**(2): p. 479-487.
59. Agency, U.E.P., *Drinking water regulations: maximum contaminant level goals and national primary drinking water regulations for lead and copper*, F. Regist, Editor 1988. p. 31516-78.
60. Barceloux, D.G., *Copper*. Journal of Toxicology-Clinical Toxicology, 1999. **37**(2): p. 217-230.
61. Cuppett, J.D., S.E. Duncan, and A.M. Dietrich, *Evaluation of copper speciation and water quality factors that affect aqueous copper tasting response*. Chemical Senses, 2006. **31**(7): p. 689-697.
62. Clifford, D., S. Subramonian, and T.J. Sorg, *Water-Treatment Processes .3. Removing Dissolved Inorganic Contaminants from Water*. Environmental Science & Technology, 1986. **20**(11): p. 1072-1080.
63. Jackson, B.P. and W.P. Miller, *Arsenic and selenium speciation in coal fly ash extracts by ion chromatography-inductively coupled plasma mass spectrometry*. Journal of Analytical Atomic Spectrometry, 1998. **13**(10): p. 1107-1112.
64. EPA, U., *Arsenic Removal from Drinking Water by Ion Exchange and Activated Alumina Plants.*, 2000, Prepared by Battelle under contract 68-C7-0008 for EPA ORD.
65. Choo, K.H., H. Lee, and S.J. Choi, *Iron and manganese removal and membrane fouling during UF in conjunction with prechlorination for drinking water treatment*. Journal of Membrane Science, 2005. **267**(1-2): p. 18-26.
66. Barakat, M.A. and N. Sahiner, *Cationic hydrogels for toxic arsenate removal from aqueous environment*. Journal of Environmental Management, 2008. **88**(4): p. 955-961.
67. Pettine, M., L. Campanella, and F.J. Millero, *Arsenite oxidation by H₂O₂ in aqueous solutions*. Geochimica Et Cosmochimica Acta, 1999. **63**(18): p. 2727-2735.
68. Kim, M.J. and J. Nriagu, *Oxidation of arsenite in groundwater using ozone and oxygen*. Science of the Total Environment, 2000. **247**(1): p. 71-79.
69. Pettine, M. and F.J. Millero, *Effect of metals on the oxidation of As(III) with H₂O₂*. Marine Chemistry, 2000. **70**(1-3): p. 223-234.
70. Hug, S.J. and O. Leupin, *Iron-catalyzed oxidation of arsenic(III) by oxygen and by hydrogen peroxide: pH-dependent formation of oxidants in the Fenton reaction*. Environmental Science & Technology, 2003. **37**(12): p. 2734-2742.
71. Nieminski, E. and D. Evans, *Pilot Testing of Trace-Metals Removal with Ozone at Snowbird-Ski-Resort*. Ozone-Science & Engineering, 1995. **17**(3): p. 297-309.
72. Bradl, H.B., *Adsorption of heavy metal ions on soils and soils constituents*. Journal of Colloid and Interface Science, 2004. **277**(1): p. 1-18.
73. Reed, B.E. and S.R. Cline, *Retention and Release of Lead by a Very Fine Sandy Loam .1. Isotherm Modeling*. Separation Science and Technology, 1994. **29**(12): p. 1529-1551.
74. Habuda-Stanic, M., et al., *Arsenite and arsenate sorption by hydrous ferric oxide/polymeric material*. Desalination, 2008. **229**(1-3): p. 1-9.
75. Pollard, S.J.T., et al., *Low-Cost Adsorbents for Waste and Waste-Water Treatment - a Review*. Science of the Total Environment, 1992. **116**(1-2): p. 31-52.

76. Mohan, D. and C.U. Pittman, *Activated carbons and low cost adsorbents for remediation of tri- and hexavalent chromium from water*. Journal of Hazardous Materials, 2006. **137**(2): p. 762-811.
77. Babel, S. and T.A. Kurniawan, *Low-cost adsorbents for heavy metals uptake from contaminated water: a review*. Journal of Hazardous Materials, 2003. **97**(1-3): p. 219-243.
78. CSIRO. *Activated Carbon*. 2002; Available from: <ftp://enecon.com.au/activated.html>.
79. Altundogan, H.S., et al., *Arsenic removal from aqueous solutions by adsorption on red mud*. Waste Management, 2000. **20**(8): p. 761-767.
80. Genc-Fuhrman, H., J.C. Tjell, and D. McConchie, *Increasing the arsenate adsorption capacity of neutralized red mud (Bauxsol)*. Journal of Colloid and Interface Science, 2004. **271**(2): p. 313-320.
81. Reed, B.E., R. Vaughan, and L.Q. Jiang, *As(III), As(V), Hg, and Pb removal by Fe-oxide impregnated activated carbon*. Journal of Environmental Engineering-Asce, 2000. **126**(9): p. 869-873.
82. Chen, W.F., et al., *Arsenic removal by iron-modified activated carbon*. Water Research, 2007. **41**(9): p. 1851-1858.
83. Vaughan, R.L. and B.E. Reed, *Modeling As(V) removal by a iron oxide impregnated activated carbon using the surface complexation approach*. Water Research, 2005. **39**(6): p. 1005-1014.
84. Li, Y.H., et al., *Competitive adsorption of Pb²⁺, Cu²⁺ and Cd²⁺ ions from aqueous solutions by multiwalled carbon nanotubes*. Carbon, 2003. **41**(14): p. 2787-2792.
85. Qi, L.F. and Z.R. Xu, *Lead sorption from aqueous solutions on chitosan nanoparticles*. Colloids and Surfaces a-Physicochemical and Engineering Aspects, 2004. **251**(1-3): p. 183-190.
86. Bang, S., et al., *Removal of arsenic from groundwater by granular titanium dioxide adsorbent*. Chemosphere, 2005. **60**(3): p. 389-397.
87. Diebold, U., *The surface science of titanium dioxide*. Surface Science Reports, 2003. **48**(5-8): p. 53-229.
88. Martra, G., *Lewis acid and base sites at the surface of microcrystalline TiO₂ anatase: relationships between surface morphology and chemical behaviour*. Applied Catalysis a-General, 2000. **200**(1-2): p. 275-285.
89. Engates, K.E. and H.J. Shipley, *Adsorption of Pb, Cd, Cu, Zn, and Ni to titanium dioxide nanoparticles: effect of particle size, solid concentration, and exhaustion*. Environmental Science and Pollution Research, 2011. **18**(3): p. 386-395.
90. Liang, P., T.Q. Shi, and J. Li, *Nanometer-size titanium dioxide separation/preconcentration and FAAS determination of trace Zn and Cd in water sample*. International Journal of Environmental Analytical Chemistry, 2004. **84**(4): p. 315-321.
91. Bissen, M., et al., *TiO₂-catalyzed photooxidation of arsenite to arsenate in aqueous samples*. Chemosphere, 2001. **44**(4): p. 751-757.
92. Pena, M.E., et al., *Adsorption of As(V) and As(III) by nanocrystalline titanium dioxide*. Water Research, 2005. **39**(11): p. 2327-2337.
93. Puma, G.L., et al., *Preparation of titanium dioxide photocatalyst loaded onto activated carbon support using chemical vapor deposition: A review paper*. Journal of Hazardous Materials, 2008. **157**(2-3): p. 209-219.

94. Berg, M., et al., *Arsenic contamination of groundwater and drinking water in Vietnam: A human health threat*. Environmental Science & Technology, 2001. **35**(13): p. 2621-2626.
95. Chiou, H.Y., et al., *Incidence of Internal Cancers and Ingested Inorganic Arsenic - a 7-Year Follow-up-Study in Taiwan*. Cancer Research, 1995. **55**(6): p. 1296-1300.
96. Agency, U.E.P., *Office of Ground Water and Drinking Water.*, 2002.
97. Kumar, P.R., et al., *Removal of arsenic from water by electrocoagulation*. Chemosphere, 2004. **55**(9): p. 1245-1252.
98. Amin, M.N., et al., *Removal of arsenic in aqueous solutions by adsorption onto waste rice husk*. Industrial & Engineering Chemistry Research, 2006. **45**(24): p. 8105-8110.
99. Allen, S.J., et al., *The adsorption of pollutants by peat, lignite and activated chars*. Journal of Chemical Technology and Biotechnology, 1997. **68**(4): p. 442-452.
100. Wu, Y.H., et al., *Behavior of chromium and arsenic on activated carbon*. Journal of Hazardous Materials, 2008. **159**(2-3): p. 380-384.
101. Diamadopoulos, E., S. Ioannidis, and G.P. Sakellaropoulos, *As(V) Removal from Aqueous-Solutions by Fly-Ash*. Water Research, 1993. **27**(12): p. 1773-1777.
102. Zhang, H. and H.M. Selim, *Kinetics of arsenate adsorption-desorption in soils*. Environmental Science & Technology, 2005. **39**(16): p. 6101-6108.
103. Manning, B.A. and S. Goldberg, *Adsorption and stability of arsenic(III) at the clay mineral-water interface*. Environmental Science & Technology, 1997. **31**(7): p. 2005-2011.
104. Altundogan, H.S., et al., *Arsenic adsorption from aqueous solutions by activated red mud*. Waste Management, 2002. **22**(3): p. 357-363.
105. Wang, S.B., H.M. Ang, and M.O. Tade, *Novel applications of red mud as coagulant, adsorbent and catalyst for environmentally benign processes*. Chemosphere, 2008. **72**(11): p. 1621-1635.
106. Poulin, E., J.F. Blais, and G. Mercier, *Transformation of red mud from aluminium industry into a coagulant for wastewater treatment*. Hydrometallurgy, 2008. **92**(1-2): p. 16-25.
107. Cengeloglu, Y., et al., *Recovery and concentration of metals from red mud by Donnan dialysis*. Colloids and Surfaces a-Physicochemical and Engineering Aspects, 2003. **223**(1-3): p. 95-101.
108. Li, Y.R., et al., *Arsenic removal from aqueous solution using ferrous based red mud sludge*. Journal of Hazardous Materials, 2010. **177**(1-3): p. 131-137.
109. Zhang, S.W., et al., *Arsenate removal from aqueous solutions using modified red mud*. Journal of Hazardous Materials, 2008. **152**(2): p. 486-492.
110. Deliyanni, E.A., et al., *Sorption of As(V) ions by akaganeite-type nanocrystals*. Chemosphere, 2003. **50**(1): p. 155-163.
111. Alp, A. and M.S. Goral, *The influence of soda additive on the thermal properties of red mud*. Journal of Thermal Analysis and Calorimetry, 2003. **73**(1): p. 201-207.
112. Elizalde-Gonzalez, M.P., et al., *Sorption on natural solids for arsenic removal*. Chemical Engineering Journal, 2001. **81**(1-3): p. 187-195.
113. Cheng, R.C., H.C. Wang, and M.D. Beuhler, *Enhanced Coagulation for Arsenic Removal*. Journal American Water Works Association, 1994. **86**(9): p. 79-90.

114. Wilkie, J.A. and J.G. Hering, *Adsorption of arsenic onto hydrous ferric oxide: Effects of adsorbate/adsorbent ratios and co-occurring solutes*. Colloids and Surfaces a-Physicochemical and Engineering Aspects, 1996. **107**: p. 97-110.
115. Pierce, M.L. and C.B. Moore, *Adsorption of Arsenite on Amorphous Iron Hydroxide from Dilute Aqueous-Solution*. Environmental Science & Technology, 1980. **14**(2): p. 214-216.
116. Ayoob, S., A.K. Gupta, and P.B. Bhakat, *Performance evaluation of modified calcined bauxite in the sorptive removal of arsenic(III) from aqueous environment*. Colloids and Surfaces a-Physicochemical and Engineering Aspects, 2007. **293**(1-3): p. 247-254.
117. Thirunavukkarasu, O.S., T. Viraraghavan, and K.S. Subramanian, *Arsenic removal from drinking water using granular ferric hydroxide*. Water Sa, 2003. **29**(2): p. 161-170.
118. Grossl, P.R., et al., *Arsenate and chromate retention mechanisms on goethite .2. Kinetic evaluation using a pressure-jump relaxation technique*. Environmental Science & Technology, 1997. **31**(2): p. 321-326.
119. Pierce, M.L. and C.B. Moore, *Adsorption of Arsenite and Arsenate on Amorphous Iron Hydroxide*. Water Research, 1982. **16**(7): p. 1247-1253.
120. Pedersen, H.D., D. Postma, and R. Jakobsen, *Release of arsenic associated with the reduction and transformation of iron oxides*. Geochimica Et Cosmochimica Acta, 2006. **70**(16): p. 4116-4129.
121. Xu, Y.H., T. Nakajima, and A. Ohki, *Adsorption and removal of arsenic(V) from drinking water by aluminum-loaded Shirasu-zeolite*. Journal of Hazardous Materials, 2002. **92**(3): p. 275-287.
122. Lagergren, S., *Zur theorie der sogenannten adsorption geloster stoffe kungliga svenska vetenskapsakademiens*. Handlingar 1898. **24**: p. 1–39.
123. Kannan, N. and M.M. Sundaram, *Kinetics and mechanism of removal of methylene blue by adsorption on various carbons - a comparative study*. Dyes and Pigments, 2001. **51**(1): p. 25-40.
124. Low, K.S., C.K. Lee, and S.C. Liew, *Sorption of cadmium and lead from aqueous solutions by spent grain*. Process Biochemistry, 2000. **36**(1-2): p. 59-64.
125. Wu, F.C., R.L. Tseng, and R.S. Juang, *Enhanced abilities of highly swollen chitosan beads for color removal and tyrosinase immobilization*. Journal of Hazardous Materials, 2001. **81**(1-2): p. 167-177.
126. Wang, X.S., et al., *The removal of basic dyes from aqueous solutions using agricultural by-products*. Journal of Hazardous Materials, 2008. **157**(2-3): p. 374-385.
127. Weber J.R., W.J. and J.C. Morris, *Kinetics of adsorption on carbon from solution*. J. Sani. Eng. Div., 1963. **89**: p. 31-39.
128. Findon, A., G. Mckay, and H.S. Blair, *Transport Studies for the Sorption of Copper Ions by Chitosan*. Journal of Environmental Science and Health Part a-Environmental Science and Engineering & Toxic and Hazardous Substance Control, 1993. **A28**(1): p. 173-185.
129. Tchobanoglous, G. and F.L. Burton, *Wastewater Engineering: Treatment, Disposal and Reuse* 1991, New York.: McGraw-Hill.
130. Langmuir, I., *The adsorption of gases on plane surfaces of glass, mica and platinum*. J. Am. Chem. Soc, 1918. **40**: p. 1361–1403.
131. Hasany, S.M., M.M. Saeed, and M. Ahmed, *Sorption and thermodynamic behavior of zinc(II)-thiocyanate complexes onto polyurethane foam from acidic*

- solutions*. Journal of Radioanalytical and Nuclear Chemistry, 2002. **252**(3): p. 477-484.
132. Yurdakoc, M., et al., *Kinetic and thermodynamic studies of boron removal by Siral 5, Siral 40, and Siral 80*. Journal of Colloid and Interface Science, 2005. **286**(2): p. 440-446.
 133. Hobson, J.P., *Calculated physical adsorption isotherms of neon and radon on a heterogeneous surface*. Journal of Vacuum Science & Technology a-Vacuum Surfaces and Films, 1997. **15**(3): p. 728-730.
 134. Ramesh, A., et al., *Adsorption of inorganic and organic arsenic from aqueous solutions by polymeric Al/Fe modified montmorillonite*. Separation and Purification Technology, 2007. **56**(1): p. 90-100.
 135. Benhammou, A., et al., *Adsorption of metal ions onto Moroccan stevensite: kinetic and isotherm studies*. Journal of Colloid and Interface Science, 2005. **282**(2): p. 320-326.
 136. Ustinov, E.A., N.S. Polyakov, and G.A. Petukhova, *Statistical interpretation of the Dubinin-Radushkevich equation*. Russian Chemical Bulletin, 1999. **48**(2): p. 261-265.
 137. Mahramanlioglu, M., I. Kizilcikli, and I.O. Bicer, *Adsorption of fluoride from aqueous solution by acid treated spent bleaching earth*. Journal of Fluorine Chemistry, 2002. **115**(1): p. 41-47.
 138. Singh, T.S. and K.K. Pant, *Equilibrium, kinetics and thermodynamic studies for adsorption of As(III) on activated alumina*. Separation and Purification Technology, 2004. **36**(2): p. 139-147.
 139. Bektas, N., S. Aydin, and M.S. Oncel, *The Adsorption of Arsenic Ions Using Beidellite, Zeolite, and Sepiolite Clays: A Study of Kinetic, Equilibrium and Thermodynamics*. Separation Science and Technology, 2011. **46**(6): p. 1005-1016.
 140. Amiri, H., et al., *Application of LECA modified with Fenton in arsenite and arsenate removal as an adsorbent*. Desalination, 2011. **272**(1-3): p. 212-217.
 141. Li, Z.H., et al., *Removal of arsenic from water using Fe-exchanged natural zeolite*. Journal of Hazardous Materials, 2011. **187**(1-3): p. 318-323.
 142. Pillewan, P., et al., *Removal of As(III) and As(V) from water by copper oxide incorporated mesoporous alumina*. Journal of Hazardous Materials, 2011. **186**(1): p. 367-375.
 143. Dutta, P.K., et al., *Adsorption of arsenate and arsenite on titanium dioxide suspensions*. Journal of Colloid and Interface Science, 2004. **278**(2): p. 270-275.
 144. Gu, Z.M., B.L. Deng, and J. Yang, *Synthesis and evaluation of iron-containing ordered mesoporous carbon (FeOMC) for arsenic adsorption*. Microporous and Mesoporous Materials, 2007. **102**(1-3): p. 265-273.
 145. Namasivayam, C. and S. Senthilkumar, *Removal of arsenic(V) from aqueous solution using industrial solid waste: Adsorption rates and equilibrium studies*. Industrial & Engineering Chemistry Research, 1998. **37**(12): p. 4816-4822.
 146. Bluthardt, C., et al., *Aqueous synthesis of high surface area metal oxides*. Catalysis Today, 2008. **137**(1): p. 132-143.
 147. Khalil, K.M.S. and S.A. Makhlof, *High surface area thermally stabilized porous iron oxide/silica nanocomposites via a formamide modified sol-gel process*. Applied Surface Science, 2008. **254**(13): p. 3767-3773.
 148. Moodley, P., et al., *Iron oxide nanoparticles on flat oxidic surfaces-Introducing a new model catalyst for Fischer-Tropsch catalysis*. Catalysis Today, 2010. **154**(1-2): p. 142-148.

149. Kwon, S.C., et al., *Nano- and micro-iron oxide catalysts for controlling the emission of carbon monoxide and methane*. Separation and Purification Technology, 2007. **58**(1): p. 40-48.
150. Rostovshchikova, T., et al., *Acidic and catalytic properties of silica modified by iron oxide nanoparticles*. Catalysis Today, 2010. **152**(1-4): p. 48-53.
151. Hla, S.S., et al., *Kinetics of high-temperature water-gas shift reaction over two iron-based commercial catalysts using simulated coal-derived syngases*. Chemical Engineering Journal, 2009. **146**(1): p. 148-154.
152. Huang, C.P. and Y.H. Huang, *Comparison of catalytic decomposition of hydrogen peroxide and catalytic degradation of phenol by immobilized iron oxides*. Applied Catalysis a-General, 2008. **346**(1-2): p. 140-148.
153. Huang, C.P., et al., *Reductive dissolution and oxidative catalysis of an immobilized iron oxide in the presence of catechol and phenol*. Journal of Molecular Catalysis a-Chemical, 2009. **304**(1-2): p. 121-127.
154. Ahammed, M.M. and K. Davra, *Performance evaluation of biosand filter modified with iron oxide-coated sand for household treatment of drinking water*. Desalination, 2011. **276**(1-3): p. 287-293.
155. Yao, P., K.H. Choo, and M.H. Kim, *A hybridized photocatalysis-microfiltration system with iron oxide-coated membranes for the removal of natural organic matter in water treatment: Effects of iron oxide layers and colloids*. Water Research, 2009. **43**(17): p. 4238-4248.
156. Hanna, K., T. Kone, and G. Medjahdi, *Synthesis of the mixed oxides of iron and quartz and their catalytic activities for the Fenton-like oxidation*. Catalysis Communications, 2008. **9**(5): p. 955-959.
157. Du, W.P., et al., *Enhanced activity of iron oxide dispersed on bentonite for the catalytic degradation of organic dye under visible light*. Catalysis Communications, 2009. **10**(14): p. 1854-1858.
158. Zelmanov, G. and R. Semiat, *Iron(3) oxide-based nanoparticles as catalysts in advanced organic aqueous oxidation*. Water Research, 2008. **42**(1-2): p. 492-498.
159. Khin, M.M., et al., *A review on nanomaterials for environmental remediation*. Energy & Environmental Science, 2012. **5**(8): p. 8075-8109.
160. Khedr, M.H., K.S.A. Halim, and N.K. Soliman, *Synthesis and photocatalytic activity of nano-sized iron oxides*. Materials Letters, 2009. **63**(6-7): p. 598-601.
161. Maleki, H., et al., *Size-controlled synthesis of superparamagnetic iron oxide nanoparticles and their surface coating by gold for biomedical applications*. Journal of Magnetism and Magnetic Materials, 2012. **324**(23): p. 3997-4005.
162. Sun, S.H., et al., *Monodisperse MFe₂O₄ (M = Fe, Co, Mn) nanoparticles*. Journal of the American Chemical Society, 2004. **126**(1): p. 273-279.
163. Bourlinos, A.B., A. Simopoulos, and D. Petridis, *Synthesis of capped ultrafine gamma-Fe₂O₃ particles from iron(III) hydroxide caprylate: A novel starting material for readily attainable organosols*. Chemistry of Materials, 2002. **14**(2): p. 899-903.
164. Rockenberger, J., E.C. Scher, and A.P. Alivisatos, *A new nonhydrolytic single-precursor approach to surfactant-capped nanocrystals of transition metal oxides*. Journal of the American Chemical Society, 1999. **121**(49): p. 11595-11596.
165. Adschiri, T., Y. Hakuta, and K. Arai, *Hydrothermal synthesis of metal oxide fine particles at supercritical conditions*. Industrial & Engineering Chemistry Research, 2000. **39**(12): p. 4901-4907.

166. Otsu, J. and Y. Oshima, *New approaches to the preparation of metal or metal oxide particles on the surface of porous materials using supercritical water: Development of supercritical water impregnation method*. Journal of Supercritical Fluids, 2005. **33**(1): p. 61-67.
167. Erdural, B.K., et al., *Hydrothermal synthesis of nanostructured TiO₂ particles and characterization of their photocatalytic antimicrobial activity*. Journal of Nanoscience and Nanotechnology, 2008. **8**(2): p. 878-886.
168. Xu, C.B. and A.S. Teja, *Supercritical water synthesis and deposition of iron oxide (alpha-Fe₂O₃) nanoparticles in activated carbon*. Journal of Supercritical Fluids, 2006. **39**(1): p. 135-141.
169. Xu, C.B. and A.S. Teja, *Characteristics of iron oxide/activated carbon nanocomposites prepared using supercritical water*. Applied Catalysis a-General, 2008. **348**(2): p. 251-256.
170. Komarneni, S., R. Roy, and Q.H. Li, *Microwave-Hydrothermal Synthesis of Ceramic Powders*. Materials Research Bulletin, 1992. **27**(12): p. 1393-1405.
171. Laha, S.C., G. Kamalakar, and R. Glaser, *Microwave-assisted synthesis of [Cr]APO-5. Microporous and Mesoporous Materials*, 2006. **90**(1-3): p. 45-52.
172. Dhage, S.R., et al., *Effect of variation of molar ratio (pH) on the crystallization of iron oxide phases in microwave hydrothermal synthesis*. Materials Letters, 2002. **57**(2): p. 457-462.
173. Cao, S.W. and Y.J. Zhu, *Iron oxide hollow spheres: Micro wave-hydro thermal Ionic liquid preparation, formation mechanism, crystal phase and morphology control and properties*. Acta Materialia, 2009. **57**(7): p. 2154-2165.
174. Tompsett, G.A., W.C. Conner, and K.S. Yngvesson, *Microwave synthesis of nanoporous materials*. Chemphyschem, 2006. **7**(2): p. 296-319.
175. Carrillo, A.I., et al., *Microwave-assisted catalysis by iron oxide nanoparticles on MCM-41: Effect of the support morphology*. Applied Catalysis a-General, 2013. **453**: p. 383-390.
176. Zhao, S.Y., et al., *Synthesis of a sugar-organometallic compound 1,1'-difurfurylferrocene and its microwave preparation of carbon/iron oxide nanocomposite*. Applied Surface Science, 2013. **264**: p. 242-246.
177. Zic, M., M. Ristic, and S. Music, *Precipitation of alpha-Fe₂O₃ from dense beta-FeOOH suspensions with added ammonium amidosulfonate*. Journal of Molecular Structure, 2009. **924-26**: p. 235-242.
178. Zach-Maor, A., R. Semiat, and H. Shemer, *Synthesis, performance, and modeling of immobilized nano-sized magnetite layer for phosphate removal*. Journal of Colloid and Interface Science, 2011. **357**(2): p. 440-446.
179. Stuerge, D. and P. Gaillard, *Microwave heating as a new way to induce localized enhancements of reaction rate. Non-isothermal and heterogeneous kinetics*. Tetrahedron, 1996. **52**(15): p. 5505-5510.
180. Lowell, S., et al., *Characterization of Porous Solids and Powders: Surface Area Pore Size and Density* 2004, Amsterdam: Kluwer Academic Publishers.
181. McKay, G., *Use of Adsorbents for the Removal of Pollutants from Wastewaters* 1985, Boca Raton: CRC Press.
182. Sip, R., *Combined form of Langmuir and Freundlich equations*,. J. Chem. Phys., 1948. **16**: p. 490.
183. Vitela-Rodriguez, A.V. and J.R. Rangel-Mendez, *Arsenic removal by modified activated carbons with iron hydro(oxide) nanoparticles*. Journal of Environmental Management, 2013. **114**: p. 225-231.

184. Muniz, G., et al., *Synthesis, characterization and performance in arsenic removal of iron-doped activated carbons prepared by impregnation with Fe(III) and Fe(II)*. Journal of Hazardous Materials, 2009. **165**(1-3): p. 893-902.
185. Abedin, M.J., J. Cotter-Howells, and A.A. Meharg, *Arsenic uptake and accumulation in rice (Oryza sativa L.) irrigated with contaminated water*. Plant and Soil, 2002. **240**(2): p. 311-319.
186. Harisha, R.S., et al., *Arsenic removal from drinking water using thin film composite nanofiltration membrane*. Desalination, 2010. **252**(1-3): p. 75-80.
187. Kocabas-Atakli, Z.O. and Y. Yurum, *Synthesis and characterization of anatase nanoadsorbent and application in removal of lead, copper and arsenic from water*. Chemical Engineering Journal 2013. **225**: p. 625–635.
188. Shi, Q.Q., et al., *Adsorption of Basic Violet 14 in aqueous solutions using KMnO₄-modified activated carbon*. Journal of Colloid and Interface Science, 2010. **343**(1): p. 188-193.
189. Ho, Y.S. and G. McKay, *Pseudo-second order model for sorption processes*. Process Biochemistry, 1999. **34**(5): p. 451-465.
190. Chien, S.H. and W.R. Clayton, *Application of Elovich Equation to the Kinetics of Phosphate Release and Sorption in Soils*. Soil Science Society of America Journal, 1980. **44**(2): p. 265-268.
191. Han, C., et al., *The optimization of As(V) removal over mesoporous alumina by using response surface methodology and adsorption mechanism*. Journal of Hazardous Materials, 2013. **254– 255**: p. 301– 309.
192. Mondal, P., C. Balomajumder, and B. Mohanty, *A laboratory study for the treatment of arsenic, iron, and manganese bearing ground water using Fe³⁺ impregnated activated carbon: Effects of shaking time, pH and temperature*. Journal of Hazardous Materials, 2007. **144**(1-2): p. 420-426.
193. Parsons, J.G., et al., *Determination of arsenic(III) and arsenic(V) binding to microwave assisted hydrothermal synthetically prepared Fe₃O₄, Mn₃O₄, and MnFe₂O₄ nanoadsorbents*. Microchemical Journal, 2009. **91**(1): p. 100-106.
194. Gao, Y. and A. Mucci, *Acid base reactions, phosphate and arsenate complexation, and their competitive adsorption at the surface of goethite in 0.7 M NaCl solution*. Geochimica Et Cosmochimica Acta, 2001. **65**(14): p. 2361-2378.
195. Calderon, R.L., *The epidemiology of chemical contaminants of drinking water*. Food and Chemical Toxicology, 2000. **38**: p. S13-S20.
196. Isaac, R.A., et al., *Corrosion in drinking water distribution systems: A major contributor of copper and lead to wastewaters and effluents*. Environmental Science & Technology, 1997. **31**(11): p. 3198-3203.
197. Milu, V., J.L. Leroy, and C. Peiffert, *Water contamination downstream from a copper mine in the Apuseni Mountains, Romania*. Environmental Geology, 2002. **42**(7): p. 773-782.
198. Benham, B., et al., *Virginia Household Water Quality Program: Corrosive Household Water*, 2011., Blacksburg, Virginia, .
199. Chatterjee, A., et al., *Arsenic in Ground-Water in 6 Districts of West-Bengal, India - the Biggest Arsenic Calamity in the World .I. Arsenic Species in Drinking-Water and Urine of the Affected People*. Analyst, 1995. **120**(3): p. 643-650.
200. Goyer, R.A. and I.J. Chisolon, *Lead: In Metallic Contamination and Human Health*, 1972, New York/London: Academic Press.

201. Leggio, L., G. Gasbarrini, and G. Addolorato, *Wilson's disease*. *Lancet*, 2007. **369**(9565): p. 902-902.
202. National Primary Drinking Water Regulations, May, 2009, Environmental Protection Agency: Washington, DC.
203. Figoli, A., et al., *Influence of operating parameters on the arsenic removal by nanofiltration*. *Water Research*, 2010. **44**(1): p. 97-104.
204. Jusoh, A., et al., *A simulation study of the removal efficiency of granular activated carbon on cadmium and lead*. *Desalination*, 2007. **206**(1-3): p. 9-16.
205. Kim, Y.H., et al., *Response to comment on "Arsenic removal using mesoporous alumina prepared via a templating method"*. *Environmental Science & Technology*, 2004. **38**(11): p. 3216-3216.
206. Li, Y.H., et al., *Removal of copper from aqueous solution by carbon nanotube/calcium alginate composites*. *Journal of Hazardous Materials*, 2010. **177**(1-3): p. 876-880.
207. Kocabas, Z.O. and Y. Yurum, *Kinetic Modeling of Arsenic Removal from Water by Ferric Ion Loaded Red Mud*. *Separation Science and Technology*, 2011. **46**(15): p. 2380-2390.
208. Sawalha, M.F., et al., *Removal of copper, lead, and zinc from contaminated water by saltbush biomass: Analysis of the optimum binding, stripping, and binding mechanism*. *Bioresource Technology*, 2008. **99**(10): p. 4438-4444.
209. Yamani, J.S., et al., *Enhanced arsenic removal using mixed metal oxide impregnated chitosan beads*. *Water Research*, 2012. **46**(14): p. 4427-4434.
210. Jin, Y.J., et al., *Removal of arsenate by cetyltrimethylammonium bromide modified magnetic nanoparticles*. *Journal of Hazardous Materials*, 2012. **227**: p. 461-468.
211. Ge, F., et al., *Effective removal of heavy metal ions Cd²⁺, Zn²⁺, Pb²⁺, Cu²⁺ from aqueous solution by polymer-modified magnetic nanoparticles*. *Journal of Hazardous Materials*, 2012. **211**: p. 366-372.
212. Dalton, J.S., et al., *Photocatalytic oxidation of NO_x gases using TiO₂: a surface spectroscopic approach*. *Environmental Pollution*, 2002. **120**(2): p. 415-422.
213. Jegadeesan, G., et al., *Arsenic sorption on TiO₂ nanoparticles: Size and crystallinity effects*. *Water Research*, 2010. **44**(3): p. 965-973.
214. Lee, J.C., M.S. Kim, and B.W. Kim, *Removal of paraquat dissolved in a photoreactor with TiO₂ immobilized on the glass-tubes of UV lamps*. *Water Research*, 2002. **36**(7): p. 1776-1782.
215. Kim, M.S., K.M. Hong, and J.G. Chung, *Removal of Cu(II) from aqueous solutions by adsorption process with anatase-type titanium dioxide*. *Water Research*, 2003. **37**(14): p. 3524-3529.
216. Alberius, P.C.A., et al., *General predictive syntheses of cubic, hexagonal, and lamellar silica and titania mesostructured thin films*. *Chemistry of Materials*, 2002. **14**(8): p. 3284-3294.
217. Sajjad, A.K.L., et al., *One step activation of WO_x/TiO₂ nanocomposites with enhanced photocatalytic activity*. *Applied Catalysis B-Environmental*, 2009. **91**(1-2): p. 397-405.
218. Khanra, A.K., et al., *Effect of NaCl on the synthesis of TiB₂ powder by a self-propagating high-temperature synthesis technique*. *Materials Letters*, 2004. **58**(5): p. 733-738.
219. Hu, J.X. and H.J. Shipley, *Evaluation of desorption of Pb (II), Cu (II) and Zn (II) from titanium dioxide nanoparticles*. *Science of the Total Environment*, 2012. **431**: p. 209-220.

220. Erdem, B., et al., *XPS and FTIR surface characterization of TiO₂ particles used in polymer encapsulation*. Langmuir, 2001. **17**(9): p. 2664-2669.
221. Li, J.X., et al., *Effect of pH, ionic strength, foreign ions and temperature on the adsorption of Cu(II) from aqueous solution to GMZ bentonite*. Colloids and Surfaces a-Physicochemical and Engineering Aspects, 2009. **349**(1-3): p. 195-201.
222. Raven, K.P., A. Jain, and R.H. Loeppert, *Arsenite and arsenate adsorption on ferrihydrite: Kinetics, equilibrium, and adsorption envelopes*. Environmental Science & Technology, 1998. **32**(3): p. 344-349.
223. Perez-Marin, A.B., et al., *Removal of cadmium from aqueous solutions by adsorption onto orange waste*. Journal of Hazardous Materials, 2007. **139**(1): p. 122-131.
224. Abramian, L. and H. El-Rassy, *Adsorption kinetics and thermodynamics of azo-dye Orange II onto highly porous titania aerogel*. Chemical Engineering Journal, 2009. **150**(2-3): p. 403-410.
225. McKay, G., *Use of Adsorbents for the Removal of Pollutants from Wastewaters* 1995, Boca Raton: CRC Press.
226. Redlich, O. and D.L.J. Peterson, *A Useful Adsorption Isotherm*,. J. Phys. Chem., 1959. **63**: p. 1024.
227. Copello, G.J., L.E. Diaz, and V.C. Dall'Orto, *Adsorption of Cd(II) and Pb(II) onto a one step-synthesized polyampholyte: Kinetics and equilibrium studies*. Journal of Hazardous Materials, 2012. **217**: p. 374-381.
228. Dzombak, D.A. and F.M.M. Morel, *Surface Complexation Modeling, in: Hydrous Ferric Oxide* 1990, New York: Wiley.
229. Boddu, V.M., et al., *Removal of arsenic(III) and arsenic(V) from aqueous medium using chitosan-coated biosorbent*. Water Research, 2008. **42**(3): p. 633-642.
230. Vu, D., et al., *Adsorption of Cu(II) from aqueous solution by anatase mesoporous TiO₂ nanofibers prepared via electrospinning*. Journal of Colloid and Interface Science, 2012. **367**: p. 429-435.
231. Deng, S.B., R.B. Bai, and J.P. Chen, *Behaviors and mechanisms of copper adsorption on hydrolyzed polyacrylonitrile fibers*. Journal of Colloid and Interface Science, 2003. **260**(2): p. 265-272.
232. Ren, Y.M., et al., *Adsorption mechanism of copper and lead ions onto graphene nanosheet/delta-MnO₂*. Materials Chemistry and Physics, 2012. **136**(2-3): p. 538-544.
233. Yu, X.Y., et al., *Novel 3D Hierarchical Cotton-Candy-Like CuO: Surfactant-Free Solvothermal Synthesis and Application in As(III) Removal*. Acs Applied Materials & Interfaces, 2012. **4**(4): p. 1954-1962.
234. Zhang, S.J., X.Y. Li, and J.P. Chen, *Preparation and evaluation of a magnetite-doped activated carbon fiber for enhanced arsenic removal*. Carbon, 2010. **48**(1): p. 60-67.
235. Pattanayak, J., et al., *A parametric evaluation of the removal of As(V) and As(III) by carbon-based adsorbents*. Carbon, 2000. **38**(4): p. 589-596.
236. Pyrzyńska, K. and M. Bystrzejewski, *Comparative study of heavy metal ions sorption onto activated carbon, carbon nanotubes, and carbon-encapsulated magnetic nanoparticles*. Colloids and Surfaces a-Physicochemical and Engineering Aspects, 2010. **362**(1-3): p. 102-109.
237. Mishra, A.K. and S. Ramaprabhu, *Functionalized graphene sheets for arsenic removal and desalination of sea water*. Desalination, 2011. **282**: p. 39-45.

238. Ohe, K., et al., *Adsorption behavior of arsenic(III) and arsenic(V) using magnetite*. Journal of Chemical Engineering of Japan, 2005. **38**(8): p. 671-676.
239. Saleh, T.A. and V.K. Gupta, *Photo-catalyzed degradation of hazardous dye methyl orange by use of a composite catalyst consisting of multi-walled carbon nanotubes and titanium dioxide*. Journal of Colloid and Interface Science, 2012. **371**: p. 101-106.
240. Li, Y.J., et al., *Photodecolorization of Rhodamine B on tungsten-doped TiO₂/activated carbon under visible-light irradiation*. Journal of Hazardous Materials, 2012. **227**: p. 25-33.
241. Zhang, P., et al., *Synthesis of mesoporous magnetic Co-NPs/carbon nanocomposites and their adsorption property for methyl orange from aqueous solution*. Journal of Colloid and Interface Science, 2013. **389**: p. 10-15.
242. Lodeiro, P., et al., *Novel Fe loaded activated carbons with tailored properties for As(V) removal: Adsorption study correlated with carbon surface chemistry*. Chemical Engineering Journal, 2013. **215**: p. 105-112.
243. Zhang, Q.L., et al., *A method for preparing ferric activated carbon composites adsorbents to remove arsenic from drinking water*. Journal of Hazardous Materials, 2007. **148**(3): p. 671-678.
244. Mishra, A.K. and S. Ramaprabhu, *Magnetite Decorated Multiwalled Carbon Nanotube Based Supercapacitor for Arsenic Removal and Desalination of Seawater*. Journal of Physical Chemistry C, 2010. **114**(6): p. 2583-2590.
245. Leary, R. and A. Westwood, *Carbonaceous nanomaterials for the enhancement of TiO₂ photocatalysis*. Carbon, 2011. **49**(3): p. 741-772.
246. Daghfir, R., P. Drogui, and D. Robert, *Modified TiO₂ For Environmental Photocatalytic Applications: A Review*. Industrial & Engineering Chemistry Research, 2013. **52**(10): p. 3581-3599.
247. Wang, X.J., et al., *A novel approach towards high-performance composite photocatalyst of TiO₂ deposited on activated carbon*. Applied Surface Science, 2009. **255**(7): p. 3953-3958.
248. Chen, C., et al., *Preparation, characterization and visible-light activity of carbon modified TiO₂ with two kinds of carbonaceous species*. Journal of Molecular Catalysis a-Chemical, 2009. **314**(1-2): p. 35-41.
249. Orlanducci, S., et al., *Nanocrystalline TiO₂ on single walled carbon nanotube arrays: Towards the assembly of organized C/TiO₂ nanosystems*. Carbon, 2006. **44**(13): p. 2839-2843.
250. Cai, J.H., et al., *Synthesis, characterization and visible-light photocatalytic activity of TiO₂-SiO₂ composite modified with zinc porphyrins*. Journal of Sol-Gel Science and Technology, 2012. **62**(3): p. 432-440.
251. Corradetti, S., et al., *Boron carbide as a target for the SPES project*. Journal of Nuclear Materials, 2013. **432**(1-3): p. 212-221.
252. El-Sheikh, A.H., et al., *Deposition of anatase on the surface of activated carbon*. Surface & Coatings Technology, 2004. **187**(2-3): p. 284-292.
253. Figaro, S., et al., *Adsorption studies of molasse's wastewaters on activated carbon: Modelling with a new fractal kinetic equation and evaluation of kinetic models*. Journal of Hazardous Materials, 2009. **161**(2-3): p. 649-656.
254. Onal, Y., et al., *Adsorption kinetics of malachite green onto activated carbon prepared from Tuncbilek lignite*. Journal of Hazardous Materials, 2006. **128**(2-3): p. 150-157.

255. Cheung, W.H., Y.S. Szeto, and G. McKay, *Intraparticle diffusion processes during acid dye adsorption onto chitosan*. *Bioresource Technology*, 2007. **98**(15): p. 2897-2904.
256. Temkin, M. and V. Pyzhev, *Kinetic of ammonia synthesis on promoted iron*. *Catalysts Acta Physiochim URSS*, 1940. **12**(3): p. 327-56.
257. Li, Z., et al., *Carbon nanotube/titanium dioxide (CNT/TiO₂) core-shell nanocomposites with tailored shell thickness, CNT content and photocatalytic/photoelectrocatalytic properties*. *Applied Catalysis B-Environmental*, 2011. **110**: p. 50-57.
258. Li, Z.J., et al., *As(V) and As(III) removal from water by a Ce-Ti oxide adsorbent: Behavior and mechanism*. *Chemical Engineering Journal*, 2010. **161**(1-2): p. 106-113.
259. Bednar, A.J., et al., *Preserving the distribution of inorganic arsenic species in groundwater and acid mine drainage samples*. *Environmental Science & Technology*, 2002. **36**(10): p. 2213-2218.
260. Liu, G.J., et al., *Effect of NOM on arsenic adsorption by TiO₂ in simulated As(III)-contaminated raw waters*. *Water Research*, 2008. **42**(8-9): p. 2309-2319.
261. Yu, L., et al., *Arsenite removal from aqueous solutions by gamma-Fe₂O₃-TiO₂ magnetic nanoparticles through simultaneous photocatalytic oxidation and adsorption*. *Journal of Hazardous Materials*, 2013. **246**: p. 10-17.
262. Ito, A., et al., *Biological oxidation of arsenite in synthetic groundwater using immobilised bacteria*. *Water Research*, 2012. **46**(15): p. 4825-4831.
263. Sanchez, J. and B.L. Rivas, *Arsenic extraction from aqueous solution: Electrochemical oxidation combined with ultrafiltration membranes and water-soluble polymers*. *Chemical Engineering Journal*, 2010. **165**(2): p. 625-632.
264. Sorlini, S. and F. Gialdini, *Conventional oxidation treatments for the removal of arsenic with chlorine dioxide, hypochlorite, potassium permanganate and monochloramine*. *Water Research*, 2010. **44**(19): p. 5653-5659.
265. Zhang, F.S. and H. Itoh, *Photocatalytic oxidation and removal of arsenite from water using slag-iron oxide-TiO₂ adsorbent*. *Chemosphere*, 2006. **65**(1): p. 125-131.
266. Zhou, W., et al., *Photodegradation of organic contamination in wastewaters by bonding TiO₂/single-walled carbon nanotube composites with enhanced photocatalytic activity*. *Chemosphere*, 2010. **81**(5): p. 555-561.
267. Pany, S., K.M. Parida, and B. Naik, *Facile fabrication of mesoporosity driven N-TiO₂@CS nanocomposites with enhanced visible light photocatalytic activity*. *Rsc Advances*, 2013. **3**(15): p. 4976-4984.
268. Zhang, J., et al., *UV Raman spectroscopic study on TiO₂. I. Phase transformation at the surface and in the bulk*. *Journal of Physical Chemistry B*, 2006. **110**(2): p. 927-935.
269. Chauhan, R., A. Kumar, and R.P. Chaudhary, *Structural and optical characterization of Ag-doped TiO₂ nanoparticles prepared by a sol-gel method*. *Research on Chemical Intermediates*, 2012. **38**(7): p. 1443-1453.
270. Zhang, J., et al., *UV Raman Spectroscopic Study on TiO₂. II. Effect of Nanoparticle Size on the Outer/Inner Phase Transformations*. *Journal of Physical Chemistry C*, 2009. **113**(5): p. 1698-1704.
271. Han, C.Y., et al., *Synthesis and characterization of mesoporous alumina and their performances for removing arsenic(V)*. *Chemical Engineering Journal*, 2013. **217**: p. 1-9.

272. Chen, B., et al., *Facile synthesis of mesoporous Ce-Fe bimetal oxide and its enhanced adsorption of arsenate from aqueous solutions*. Journal of Colloid and Interface Science, 2013. **398**: p. 142-151.
273. Tan, C.Y., et al., *Biosorption of Basic Orange from aqueous solution onto dried A. filiculoides biomass: Equilibrium, kinetic and FTIR studies*. Desalination, 2011. **266**(1-3): p. 56-62.
274. Fujishima, A. and X.T. Zhang, *Titanium dioxide photocatalysis: present situation and future approaches*. Comptes Rendus Chimie, 2006. **9**(5-6): p. 750-760.
275. Li, Q., N.J. Easter, and J.K. Shang, *As(III) Removal by Palladium-Modified Nitrogen-Doped Titanium Oxide Nanoparticle Photocatalyst*. Environmental Science & Technology, 2009. **43**(5): p. 1534-1539.
276. Miller, S.M. and J.B. Zimmerman, *Novel, bio-based, photoactive arsenic sorbent: TiO₂-impregnated chitosan bead*. Water Research, 2010. **44**(19): p. 5722-5729.
277. Xu, Z.H. and X.G. Meng, *Size effects of nanocrystalline TiO₂ on As(V) and As(III) adsorption and As(III) photooxidation*. Journal of Hazardous Materials, 2009. **168**(2-3): p. 747-752.

VITA

ZÜLEYHA ÖZLEM KOCABAŞ ATAKLI

Istanbul, Turkey

Date & Place of Birth: August, 31, 1985 - Istanbul/Turkey

E-mail: ozlemkocabas@sabanciuniv.edu

CITIZENSHIP: Turkish

LANGUAGES: English and Turkish

EDUCATION

2008-2013 Ph.D., Sabancı University

Istanbul, Turkey

Material Science and Engineering

Comprehensive Examinations: Written and Oral Completed with Distinction

Ph.D. Thesis: "Fabrication of Nano and Porous Materials & Their Utilization in Purification of Water Contaminated with Arsenic, Copper and Lead"

2003-2008 Bachelor of Science, Sabancı University

Istanbul, Turkey

Major Degree: Material Science and Engineering

Minor Degree: Chemistry

PUBLICATIONS

A) Articles in Refereed Journals

Z. Özlem Kocabas-Ataklı, Yuda Yürüm, A Facile Synthesis of Activated Carbon/Titanium Dioxide Nanocomposites for Enhanced As(III) Removal from Water, submitted to *Carbon*, **2013**.

Alp Yürüm, Z. Özlem Kocabaş-Ataklı, Meltem Sezen and Yuda Yürüm, “Arsenic (V) Removal from Water by Iron Oxide/Activated Carbon System Manufactured by Microwave Heating”, submitted to *Water Research*, **2013**.

Kaan Yılcıoğlu, Z. Özlem Kocabaş Ataklı, Yuda Yürüm, Selim Çetiner, Evaluation of Inducing ROS production on lipid accumulation in the tested hyper saline alga *Dunaliella* sp. and their bioaccumulation potentials of Cu^{2+} , Ni^{2+} , and Zn^{2+} , in preparation, **2013**.

Z. Özlem Kocabas-Ataklı, Yuda Yürüm, “Synthesis and Characterization of Anatase Nanoadsorbent and Application in Removal of Lead, Copper and Arsenic from Water”, *Chemical Engineering*, 225, pp. 625–635, **2013**.

Aslı Nalbant Ergün, Z. Özlem Kocabaş, Yuda Yürüm, “Synthesis of Mesoporous MCM-41 Materials by Low Power Microwave Heating”, *Chemical Engineering Communications*, 200, pp. 1057-1070, **2013**.

Mustafa Baysal, Z. Özlem Kocabaş, Firuze Okyay, Alp Yürüm, F. Duygun, Sedat Inan, Yuda Yürüm, “Biogasification and Combustion Reactions of Turkish Lignites: Adsorption Behavior and Biogasification of Soma Lignite and Co-Combustion of Beypazari Lignite With Biomass”, Fuel Section B, Fuels, Chemicals, Materials and Energy from Biomass, Fuel 236, 243rd American Chemical Society National Meeting, **2012**.

Burcu Saner, Z. Özlem Kocabaş, Aslı Nalbant Ergun, Mustafa Baysal, Ilse Letofsky-Papst, Yuda Yürüm, “Synthesis of Boron Nitride Nanostructures over Fe³⁺ Impregnated Mesoporous Silica MCM-41 Chemical Vapor Deposition Technique and Measurement of Their Hydrogen Capacity”, *Industrial Chemical Engineering Research*, 51, pp. 11341–11347, **2012**.

Z. Özlem Kocabaş, Yuda Yürüm, “Kinetic Modeling of Arsenic Removal From Water by Ferric Ion Loaded Red Mud”, *Separation Science and Technology*, 46, pp. 2380-2390, **2011**.

B) Articles in Conference Proceedings

Yuda Yurum, Alp Yurum, Zuleyha Ozlem Kocabas, Raphael Semiat, “Synthesis and Characterization of Iron-impregnated Pre-oxidized Activated Carbon Prepared by Microwave Radiation for As(V) Removal from Water”, EGU General Assembly 2013, Vienna, Austria: **2013**.

Z. Özlem Kocabaş, Burcu Açiksöz and Yuda Yürüm, “Binding Mechanisms of As(III) on Activated Carbon/Titanium Dioxide Nanocomposites: A Potential Method for Arsenic Removal from Water”. MRS Proceedings, 1449, *Cambridge Univ. Press*, **2012**.

Z. Özlem Kocabaş, Yuda Yürüm, “Evaluation of the Adsorption Potential of Synthesized Anatase Nanoparticles for Arsenic Removal”, MRS FALL Proceeding, 1317, *Cambridge Univ. Press*, **2011**.

CONFERENCES

Z. Özlem Kocabaş, Burcu Açiksöz, Yuda Yürüm, “Synthesis of Titanium Dioxide Nanoparticles and Evaluation of Efficiency for Sorption Of Lead, Copper And Arsenic From Water”, *NanoTRVIII 2012, 8th Nanoscience and Nanotechnology Conference*, Hacettepe University, Ankara, Turkey, June 25-29, 2012. Oral presentation.

Z. Özlem Kocabaş, Burcu Açiksöz and Yuda Yürüm (2012). “Binding Mechanisms of As(III) on Activated Carbon/Titanium Dioxide Nanocomposites: A Potential Method for Arsenic Removal from Water.” San Francisco, *MRS Spring 2012*. Oral presentation.

Z. Özlem Kocabaş, Yuda Yürüm, “Synthesis of Titanium Dioxide Nanoparticles and Their Application for Simultaneous Photocatalytic Oxidation of As(III) and Sorption of As(V)”, San Diego, *ACS Spring 2012*. Oral presentation.

Burcu Saner Okan, Z. Özlem Kocabaş, Aslı Nalbant Ergün, Mustafa Baysal, Yuda Yürüm, “Synthesis of Boron Nitride Nanostructures by Chemical Vapor Deposition Technique and Measurement of Their Hydrogen Storage Capacity”, *EMCC 7, 7th Chemical Engineering Conference for Collaborative Research in Eastern Mediterranean Countries*, Corfu, Greece, April 27- May 1, 2012.

Burcu Saner, Z. Özlem Kocabaş, Aslı Nalbant Ergün, Yuda Yürüm, “Template Synthesis of Boron Nitride Nanotubes over Iron Impregnated Mesoporous Silica MCM-41 by Chemical Vapor Deposition Technique”, *17th International Symposium on Boron, Borides and Related Materials*, Istanbul, Turkey, September 11-17, 2011. Oral presentation.

Yuda Yürüm, Burcu Saner Okan, Züleyha Özlem Kocabaş, Firuze Okyay, and Aslı Nalbant Ergün, Ahu Gümrah Dumanlı, Alp Yürüm, “Bor ve Karbon Nanomalzemelerin Üretimi ve Karakterizasyonu”, *Kocaeli Nanoteknoloji Günleri*, Kocaeli, Türkiye: Kocaeli Üniversitesi 2011. Oral Presentation.

Z. Özlem Kocabaş, Yuda Yürüm, “Evaluation of the Adsorption Potential of Synthesized Anatase Nanoparticles for Arsenic Removal”, Boston, *MRS FALL 2010*, November 2010. Oral presentation.

Z. Özlem Kocabaş, Yuda Yürüm, “Comparative Study of Arsenic Removal Efficiency from Water by Adsorption and Photocatalytic Oxidation with Titanium Dioxide”, *International Conference on Clean Energy*, Cyprus, May 2010. Oral presentation.

Z. Özlem Kocabaş, Yuda Yürüm, “Enhanced Photocatalytic Oxidation of As³⁺ Using Titania Nanoparticles for Arsenic Removal from Water”, *Third National Catalysis Conference*, Zonguldak, May 2010. Oral presentation.

Z. Özlem Kocabaş, Yuda Yürüm, “Adsorption Mechanism of Arsenite on Fe⁺³ Impregnated Activated Carbon”, *Carbon Materials for Today and Future, Turkish-Japanese Joint Carbon Symposium*, Istanbul, March 2010. Poster presentation.

Z. Özlem Kocabaş, Yuda Yürüm, “A Parametric Evaluation of The Removal As(III) and As(V) from Aqueous Solution by Red Mud”, *EMCC6, 6th Chemical Engineering Conference For Collaborative Research In Eastern Mediterranean Countries*, Antalya, March 2010. Poster presentation.

Z. Özlem Kocabaş, Y. Yürüm, “Removal of As(III) from Water/Wastewater by Adsorption Using Titanium Dioxide Nanoparticles”, *V. National Nanoscience And Nanotechnology Conference*, Eskisehir, June 2009. Poster presentation.

Z. Özlem Kocabaş, Yuda Yürüm, “The Effect of Titanium Dioxide Nanoparticles on As(III) Removal from Water”, *International Conference on Nanomaterials and Nanosystems*, Istanbul, August 2009. Poster presentation.

RESEARCH

2009-2011 Yuda Yürüm, Aslı Nalbant, Burcu Saner, Z. Özlem Kocabaş, Production of boron nitride nanotubes in thermal and microwave media and use of these for hydrogen storage. Project 2009.Ç230, BOREN, National Boron Research Institute.

2003-2008 **Undergraduate Research studies at Sabanci University, Turkey**

- Graduation Project: *Design of a Piezoactuator* - design of a piezoelectric mechanism consisting of a flexible structure actuated by piezoceramics,

- *Photoluminescence Properties of Bariumaluminate* – producing single phase bariumaluminate doped with Europium and Dysprosium, Project *Micro Air Vehicle* - designing and manufacturing piezoelectric composite materials, determining the properties of mechanic and piezoelectric fiber (PVDF, ZnO).

Summer 2007 Internship at BOSCH in Applied Science Research Center in Gerlingen/GERMANY

The synthesis of mullite by using sol-gel method and characterization of sintered mullite samples by instrumental analysis.

2008-2013 Research Assistant, Sabanci University

Science of Nature

Introduction to Materials Science

Analytical Chemistry

Surface Chemistry

Kinetics

ACADEMIC SCHOLARSHIPS AND AWARDS

2008-2013 Full Scholarship, Sabanci University, PhD. Program of Material Science & Engineering.

Spring 2007 Certificate of High Honor, Faculty of Engineering and Natural Sciences, Sabanci University.

Spring 2005 Certificates of Honor, Faculty of Engineering and Natural Sciences, Sabanci University.